

On-board Range-based Relative Localization

For Leader-Follower Flight of Micro Aerial Vehicles

Steven van der Helm

February 17, 2018

On-board Range-based Relative Localization

For Leader-Follower Flight of Micro Aerial Vehicles

MASTER OF SCIENCE THESIS

For obtaining the degree of Master of Science in Aerospace Engineering
at Delft University of Technology

Steven van der Helm

February 17, 2018



Delft University of Technology

Copyright © Steven van der Helm
All rights reserved.

DELFT UNIVERSITY OF TECHNOLOGY
DEPARTMENT OF
CONTROL AND SIMULATION

The undersigned hereby certify that they have read and recommend to the Faculty of Aerospace Engineering for acceptance a thesis entitled "**On-board Range-based Relative Localization**" by **Steven van der Helm** in partial fulfillment of the requirements for the degree of **Master of Science**.

Dated: February 17, 2018

Readers:

Dr. ir. Q. P. Chu

Dr. ir. G. C. H. E. de Croon

Dr. ir. C. J. M. Verhoeven

Ir. K. N. McGuire

Ir. M. Coppola

Acknowledgements

Perhaps the hardest chapter to write is the one where you are supposed to reflect on a year's worth of work, and thank the people that have helped you bring your thesis to a successful end. Nevertheless, I will give it my best shot.

With the end of my thesis comes the end of my life as a student. It has been a wonderful experience to see my friends and fellow students that I have started my Bachelor of Science with five years ago, all get their now Master of Science degrees and wander into the next phase of their lives. With this submission, I hope to join them shortly on this experience.

I can honestly say that I am glad that I chose to pursue the thesis topic that I present you today. Working on this topic has taught me many new things and gave me a new appreciation for embedded programming. For this, and for all the support throughout my entire thesis, I would like to thank my supervisors Kimberly McGuire, Mario Coppola, and Guido de Croon. Your feedback has really allowed me to elevate my work to a new level, and for that I am grateful. Together with your help I have been able to produce a thesis that I am proud of.

I would finally like to thank all my family and friends for their emotional support throughout my thesis. The thesis is inherently a project that is characterized by a large degree of autonomous working. The emotional support from family and friends has been a vital driving force to keep me motivated and moving forward.

Table of Contents

List of Abbreviations	xii
List of Symbols	xiv
1 Introduction	1
1-1 Research Context and Motivation	1
1-2 Research Objectives and Research Questions	2
1-3 Thesis Structure	3
I Scientific Paper	5
II Literature Review	31
2 Overview of Localization Hardware	33
2-1 Overview of Hardware Used in Swarm Robotics	33
2-2 Trade-off Between Different Hardware Systems used in Swarming	33
2-2-1 External Systems	34
2-2-2 On-board Systems	35
2-2-3 Best Hardware System in Robotic Swarming	38
2-2-4 Selection of Radio Technology	39
3 Introduction to Ultra-Wideband technology	41
3-1 History of Ultra-Wideband	41
3-2 Theory behind Ultra-Wideband	43
3-2-1 UWB Channel Impulse Response	43
3-2-2 IEEE Proposed Ultra-Wideband Channel Impulse Response Models	45
3-2-3 UWB Signal Shapes and Properties	46
3-3 UWB Modulation	49
3-3-1 Pulse Position Modulation	49
3-3-2 Pulse Amplitude Modulation	50

3-3-3	Pulse Shape Modulation	51
3-4	UWB Multiple Access and Spectrum Randomisation	51
3-4-1	Time-Hopping UWB	51
3-4-2	Direct Sequence Spread Spectrum Ultra Wideband	52
3-4-3	Multi-band Ultra Wideband	53
3-5	Ultra-Wideband Regulations	53
4	Uses of Ultra-Wideband Technology in the Literature	57
4-1	Localization Compared to Radar	57
4-2	Ultra-Wideband for Localization	59
4-2-1	Early Research on UWB localization	59
4-2-2	Research on Highly Accurate UWB Localization	60
4-2-3	UWB Localization Applied to Indoor Navigation	60
4-2-4	UWB Localization for Aerial Vehicle Applications	61
4-3	Ultra-Wideband as a Communication Technology	62
5	Beacon Based Localization and Ranging	65
5-1	Lateration Techniques for Localization	65
5-2	Angulation Technique for Localization	70
5-3	Uplink, Downlink, and Hybrid Localization	72
6	Two-Way Ranging Implementations and Considerations	73
III	Additional Experiments	79
7	Ranging Experiments with Ultra Wideband	81
7-1	Hardware Used in Ranging Experiment	81
7-2	Antenna Delay Calibration	82
7-3	Experiment Execution	83
7-4	Ranging Experiment Results	84
7-4-1	Raw ranging data	84
7-4-2	Processed Range Error Results and Discussion	85
7-4-3	Normality of Ranging Data and Error Bounds	89
8	Parrot Bebop 2 characteristics	91
8-1	Parrot Bebop 2 step response	91
8-2	Parrot Bebop 2 on-board measurements	92
Bibliography		95

List of Abbreviations

AMAE	Average Mean Absolute Error
AOA	Angle of Arrival
BPM	Bi-Phase Modulation
BPSK	Binary Phase Shift Keying
CEPT	European Conference of Postal and Telecommunications Administrations
CIR	Channel Impulse Response
DAA	Detect and Avoid
DC	Direct Current
DSSS	Direct Sequence Spread Spectrum
EC	European Commission
ECC	Electronic Communications Committee
EIRP	Effective Isotropic Radiated Power
EKF	Extended Kalman Filter
EM	Electromagnetic
ETSI	European Telecommunications Standard Institute
FCC	Federal Communications Commission
FDM	Frequency Division Multiplex
FOV	Field of View
FRO	First Report and Order
GML	Generalized Maximum Likelihood
GNSS	Global Navigation Satellite System
GPS	Global Positioning System
IMU	Inertial Measurement Unit
IR	Infrared
IR	Impulse Radio
ISI	Inter Symbol Interference
LDC	Low Duty Cycle
LOS	Line of Sight
LPD	Low Probability of Detection
LTI	Linear Time Invariant
MAE	Mean Absolute Error

MAC	Medium Access Control
MAV	Micro Aerial Vehicle
MB	Multi-Band
MCS	Motion Capture System
MPC	Multipath Component
NED	North-East-Down
NLOS	Non Line of Sight
NLR	Non-Linear Regression
OFDM	Orthogonal Frequency Division Multiplexing
PAM	Pulse Amplitude Modulation
PDOP	Position Dilution of Precision
PHY	Physical layer
PPM	Pulse Position Modulation
PRF	Pulse Repeat Frequency
PRT	Pulse Repetition Time
PSM	Pulse Shape Modulation
QPSK	Quadrature Phase Shift Keying
RF	Radio Frequency
RMSE	Root Mean Squared Error
RSP	Received Signal Phase
RSS	Received Signal Strength
RSSI	Received Signal Strength Indicator
SDS	Symmetric Double Sided
TDMA	Time Division Multiple Access
TDOA	Time Difference of Arrival
TH	Time-Hopping
TOA	Time of Arrival
TOF	Time of Flight
TWR	Two Way Ranging
UAV	Unmanned Aerial Vehicle
USA	United States of America
UWB	Ultra Wideband

List of Symbols

a_i	acceleration vector of drone i
$a_{x,i}$	horizontal acceleration of drone i forward
$a_{y,i}$	horizontal acceleration of drone i to the right
dt	time-step
e	positional error for follower drone
f	state differential model
h	observation model
i	virtual control input
p	relative position between two drones
p_i	absolute position of drone i
p_x	x-coordinate of relative position vector between two drones
p_y	y-coordinate of relative position vector between two drones
\tilde{q}_i	true pitch rate of drone i
r_i	yaw rate of drone i
\tilde{r}_i	true yaw rate of drone i
s_i	specific force for drone i
t	time
t_p	propagation time
u	input vector
u_i	horizontal forward velocity of drone i
v_i	velocity vector of drone i
v_{1c}	velocity command for drone 1
$v_{x,i}$	horizontal velocity of drone i forward
$v_{y,i}$	horizontal velocity of drone i to the right
x	state vector
y	output vector
A	2x2 matrix with -1 and 1 on the off-diagonal
A_d	disturbance amplitude
M	determinant
R	rotation matrix
S_i	skew symmetric matrix of drone i 's yaw rate

\mathcal{B}_i	Euler body-fixed frame of drone i
\mathcal{H}_i	horizontal body-fixed frame of drone i
\mathcal{I}	North-East-Down reference frame, assumed inertial
$\mathcal{L}_{\mathbf{f}}^n$	n-th order Lie derivative along \mathbf{f}
\mathcal{O}	observability matrix
θ_i	pitch angle of drone i
τ	time delay
ϕ_i	roll angle of drone i
ψ_i	heading angle of drone i
$\Delta p_{t_1}^{t_2}$	change in position between time t_1 and time t_2
$\Delta \psi$	heading angle difference between drone 1 and 2
$\Delta \psi_i _{t_1}^{t_2}$	heading angle change for drone i between time t_1 and time t_2
\sum	non-linear state-space system
∇	differential operator

Chapter 1

Introduction

This document contains the work performed for an MSc thesis graduation project on indoor leader-follower flight with Micro Aerial Vehicles (MAVs). This introduction serves to provide the context within this thesis resides, and the motivation for the research topic. It also presents the overall structure of this thesis for clarity.

1-1 Research Context and Motivation

Leader-follower flight is a frequently studied topic within swarm robotics. In turn, swarm robotics is a domain within robotics that focuses on groups of robots and their cooperation. The interest in swarm robotics is often sparked by observations of swarming behavior exhibited by social animals in nature, such as ants, bees, birds, and fish [15] due to their ability to accomplish rather impressive tasks when cooperating in a swarm.

What is particularly interesting about these natural examples of swarming is their inherent ability to be robust, flexible, and scalable [15]. In this context, the property of robustness pertains to a swarms ability to be relatively unaffected by loss of individual members. Flexibility means that the swarm is able to operate in a variety of different environments. Finally, scalability applies to its ability to adapt to different group sizes. [15, 98]. Naturally these properties are desirable to have also in artificially created systems, and thus the domain of swarm robotics was born.

Swarm robotics, and in particular swarm robotics with MAVs, has many potential applications. Examples that offer value specifically to MAVs are cooperative surveillance and/or mapping [1, 100, 102], localization of areas of sensory interest (e.g. chemical plumes) [44, 103], the detection of forest fires [73], or search missions in hazardous environments [12].

In order to safely and efficiently operate a group of MAVs, there are certain tasks that the swarm must autonomously be capable of executing. An example of a frequently studied task is collision avoidance between agents in the swarm [21, 95]. Another example, which is the topic of this thesis, is the task of collectively moving a group of MAVs around. As swarms increase in numbers, individually controlling agents becomes less viable, and methods are required to easily move the group around as a collective. Leader-follower flight is a solution to this problem, which is why this thesis has considered leader-follower flight as a topic.

Leader-follower flight requires MAVs to have knowledge of the relative location of the leader. This is a non-trivial problem, and was therefore also studied in this thesis. The desire was to propose a solution that would work independent of the environment that the MAVs are in, including indoor environments. This means that obtaining the relative locations between MAVs must be done with only on-board sensors. External positioning systems like the Global Navigation Satellite System (GNSS) or Motion Capture Systems (MCSs) can not be used since they are not available everywhere.

Earlier research on on-board relative localization methods has demonstrated the feasibility of wireless range-based methods to perform this task of localization [21, 39]. Wireless radio has certain favorable properties, such as the fact that it works omni-directionally and therefore does not require active tracking of neighboring agents. The implementation in [21] however showed insufficient accuracy in the relative localization results for a task like leader-follower flight. The method in [39] is susceptible to drift over longer periods of time. Furthermore, both previous implementations required each MAV to have knowledge of their heading with respect to magnetic North [21, 39]. This heading is typically obtained through magnetometer readings, which are notoriously unreliable in an indoor environment due to local magnetic disturbances [2]. These observations lead us to the research objective and research questions of this thesis.

1-2 Research Objectives and Research Questions

This thesis continues to investigate the potential of wireless range-based methods for relative localization purposes, specifically for the task of indoor leader-follower flight. The research objective throughout this thesis has been to

**improve the accuracy of on-board wireless range-based relative localization
methods for an indoor environment**

and to consequently use this to

demonstrate leader-follower flight.

As already mentioned, one of the primary drawbacks of earlier implementations of range-based relative localization methods on MAVs was their reliance on knowledge of their heading with respect to magnetic North. It has been theoretically shown however that a common heading reference is not actually necessary when performing range based relative localization [70, 113]. The first research question during this thesis was therefore:

- 1) What are the practical consequences of removing the heading dependency in range-based relative localization methods?

The second guiding research question has been:

- 2) How can range-based relative localization be used to perform leader-follower flight?

The answers to these research questions combined provide sufficient knowledge to be able to accomplish the research objective.

1-3 Thesis Structure

The thesis starts off with a scientific paper in part I. This paper answers the two research questions listed above and contains the main scientific contribution of the work performed during this thesis. The paper can be read as a stand-alone document, and the remainder of the thesis serves as additional (background) knowledge for some of the topics discussed in the paper.

In part II of the thesis, part of the literature review that was conducted during the preliminary phase of this thesis is presented.

In chapter 2, an overview is given of different methods that can be used for relative localization purposes. This chapter serves as motivation as to why wireless range-based sensors are such a promising solution compared to other solutions. It also presents why in this thesis it has been chosen to use Ultra Wideband (UWB) radio in particular to obtain range measurements, as opposed to any other existing wireless radio technology.

Because UWB is a relatively unknown radio technology, chapters 3 and 4 further go into depth on the topic of UWB. These chapters further illustrate the favorable properties of UWB, and what the technology can be used for.

Chapters 5 and 6 give an introduction into wireless radio based localization and ranging. Chapter 6 in particular discusses the concept of two-way ranging, which is the method of choice in this thesis to measure range between MAVs.

Part III contains some additional experimental results that have not been covered in the scientific paper in part I. In particular, the ranging performance of the UWB modules used in this thesis is tested and analyzed in chapter 7. Finally, the thesis concludes by evaluating some characteristic of the Parrot Bebop 2 drone¹ that was used for the experiments within this thesis in chapter 8. Both the step response of the Bebop 2 to a velocity command, and the accuracy of on-board sensors that are important to the scientific paper are discussed here.

¹<https://www.parrot.com/us/drones/parrot-bebop-2>

Part I

Scientific Paper

On-board Range-based Relative Localization applied to Leader-Follower Flight of Micro Aerial Vehicles

Steven van der Helm¹, Kimberly McGuire², Mario Coppola², and Guido de Croon²

¹MSc Student, Micro Air Vehicle Laboratory, Delft University of Technology

²Supervisor, Micro Air Vehicle Laboratory, Delft University of Technology

Abstract—In this paper a range-based relative localization solution is proposed and demonstrated in practice. The approach is based on wireless range measurements between robots, along with the communication of their velocities, accelerations, yaw rates, and height. It can be implemented on many robotic platforms without the need for dedicated sensors. With respect to previous work, we remove the dependency on a common heading reference between robots. The main advantage of this is that it makes the relative localization approach independent of magnetometer readings, which are notoriously unreliable in an indoor environment. A theoretical observability analysis shows that it may also have two disadvantages: the motion of the robots must meet more stringent conditions and the relative localization method becomes more susceptible to noise on the range measurements. However, simulation results have shown that in the presence of significant magnetic disturbances that are common to indoor environments, removing the heading dependency is beneficial. We conclude the paper by implementing the heading-independent method on real Micro Aerial Vehicles (MAVs) and performing leader-follower flight in an indoor environment. Despite the observability analysis showing leader-follower flight to be an especially difficult task, we still manage to successfully fly for over 3 minutes with two fully autonomous followers using only on-board sensing.

I. INTRODUCTION

Multi-agent and swarm robotics are heavily studied topics within the domain of Micro Aerial Vehicle (MAV) applications. They offer to make MAV applications more robust, flexible, and scalable [1, 2]. These properties pertain to a group’s ability to remain operable under loss of individual members and their ability to operate under different conditions. Furthermore, one can imagine that through cooperation a swarm of MAVs could execute tasks faster than any single MAV could.

The envisioned applications of such multi-agent robotic systems are therefore plentiful. Examples that are of interest specifically to MAVs are cooperative surveillance and/or mapping [3–5], localization of areas of sensory interest (e.g. chemical plumes) [6, 7], the detection of forest fires [8], or search missions in hazardous environments [9].

In order to deploy groups of MAVs for such applications, there are certain tasks that the group must typically be capable of performing. Frequently studied tasks are collision avoidance [10, 11] and leader-follower or formation flight [12–14]. These tasks are accomplished by the MAVs through knowledge of the locations of at least the neighboring MAVs in a group.

Obtaining the (relative) locations of neighboring agents in a group is however a non-trivial problem and many different solutions have been proposed and used in the literature.

Often used are the external systems that can provide a global reference frame within which agents can localize themselves and others. An example is the group of so called Motion Capture Systems (MCSs) [7, 15–20]. These systems can provide highly accurate location data, but only within the limited coverage provided by the system. Alternatively, the information provided by the Global Navigation Satellite System (GNSS) can be used to provide similar location data [3, 12, 14, 21, 22]. Whilst this signal is much more widely available, it is also much less accurate, inevitably leading to large required inter agent separations [23]. Furthermore, the signal cannot reliably be used indoors due to signal attenuation [24] and even in some urban environments or forests due to multipath effects [25].

To increase the versatility of the solution, the MAVs should thus use onboard sensors to determine the locations of neighboring MAVs. Often vision based methods are employed such as onboard camera based systems [11, 23, 26, 27] or infrared sensor systems [28–30]. These systems are however characterised by a limited field of view. Dealing with this issue can be done for example by creating constructs with an array of sensors [30] or by actively tracking neighbouring agents [23]. Neither solutions are ideal for groups of MAVs due to respectively the weight penalty that comes with an array of sensors, or the more limited freedom of motion and scalability as a consequence of the need for active tracking of neighbors.

An omni directional sensor would thus be more advantageous, and those sensors do exist. In fact, wireless radio transceivers can actually be used to fulfill this role and are already present on most MAV platforms by default.

Guo et al. have recently implemented an Ultra Wideband (UWB) radio based system for this task in [31]. They fuse range measurements with displacement information from each MAV to estimate the relative location between MAVs. However, their proposed method suggests that each MAV must keep track of their own displacement with respect to their initial launching point. If this measurement is obtained through on-board sensors (for example by integrating velocities) then this measurement will be subject to drift over time.

Alternatively, Coppola et al [10] have demonstrated a Bluetooth based relative localization method. Rather than using displacement information, they use, among other information,

the velocities of different MAVs to establish a relative location estimate. If the drones are capable of measuring their own velocity directly, then this measurement does not suffer from the same drift issues, making it suitable for longer flights as well.

Despite the promising results of range-based solutions, a major downside of both the implementation in [10] and in [31] is that they rely on a common frame of reference. This frame is established by having each drone measure their heading with respect to North. The magnetometers used to establish this North direction are notoriously unreliable in especially indoor environments, due to the local disturbances in the Earth's magnetic field [32]. Heading errors upwards of 80° can locally occur when magnetometers are used to infer a heading in indoor environments [32].

The difficulty of establishing a reliable direction towards North in an indoor environment is a well known problem. Consequently, researchers have proposed solutions in the form of complementary or Kalman filters [33–36], or the usage of redundant magnetic sensors to compensate the local disturbances [32, 37]. These solutions however may be overly complex for the purpose of relative localization, since it has been theoretically shown that a shared reference frame is not actually necessary when performing range based relative localization [38, 39].

The first main contribution of this paper is therefore an analysis into the consequences of removing the heading dependency in range based relative localization. This will be provided through an observability analysis and by performing simulations. Different to [38, 39], the analysis additionally considers the inclusion of acceleration information, since this is commonly known by MAVs from their Inertial Measurement Unit (IMU). Furthermore, the analysis specifically focuses on the implications that removing a heading dependency has, especially from a practical implementation point of view.

The observability analysis will show us that the task of leader-follower flight is especially difficult with range-based relative localization methods. To really show the capabilities of our method, we therefore implement it on real MAVs for precisely this difficult task of leader-follower flight. This will thus be the second main contribution of this paper.

The structure of the paper is as follows. First of all a theoretical observability analysis for range based observation with and without a reliance on a common heading is given in section II. The most important theoretical findings in this study are verified through simulation in section III. Afterwards the heading independent localization filter is implemented on real MAVs and used to demonstrate leader-follower flight in section IV. The results are reflected upon in the discussion section in section V. Finally, the overall conclusions of this paper are drawn in section VI.

II. OBSERVABILITY OF THE RELATIVE LOCALIZATION FILTER

The purpose of the eventual relative localization filter is for a drone (say drone 1) to be able to track the position of another drone (say drone 2). Despite the reference to drones

in particular, most of the conclusions that follow hold for any general system that can provide the same sensory information as used in this analysis. Furthermore, the results may be extrapolated to more than two drones, as will be demonstrated in section IV. For clarity, however, only drones 1 and 2 are referred to in the coming analysis.

In this section, an observability analysis is performed that specifically focuses on the practical implications of performing range based relative localization with or without reliance on a common heading reference.

A. Preliminaries

The primary analytical concept that will be used to study range based relative localization is that of *local weak observability*, as introduced by Hermann and Krener in [40]. This concept, as the name implies, can be used to make claims regarding whether a specific state can be distinguished from other states in its neighborhood. Local weak observability can be demonstrated through an analytical test [40], which will now be briefly introduced for reference, using the notation style used in this paper.

Consider a generic non-linear state-space system Σ defined by:

$$\dot{\mathbf{x}} = \mathbf{f}(\mathbf{x}, \mathbf{u}) \quad (1)$$

$$\mathbf{y} = \mathbf{h}(\mathbf{x}) \quad (2)$$

The system Σ has state vector $\mathbf{x} = [x_1, x_2, \dots, x_n]^T \in \mathbb{R}^n$, an input vector $\mathbf{u} \in \mathbb{R}^l$, and an output vector $\mathbf{y} \in \mathbb{R}^m$. The vector function $\mathbf{f}(\mathbf{x}, \mathbf{u})$ contains the definitions for the time derivatives of all the states in \mathbf{x} and the vector function $\mathbf{h}(\mathbf{x})$ contains the observation equations for the system. Define for this system the following Lie derivatives:

$$\mathcal{L}_{\mathbf{f}}^0 \mathbf{h} = \mathbf{h} \quad (3)$$

$$\mathcal{L}_{\mathbf{f}}^1 \mathbf{h} = \nabla \otimes \mathcal{L}_{\mathbf{f}}^0 \mathbf{h} \cdot \mathbf{f} \quad (4)$$

⋮

$$\mathcal{L}_{\mathbf{f}}^i \mathbf{h} = \nabla \otimes \mathcal{L}_{\mathbf{f}}^{i-1} \mathbf{h} \cdot \mathbf{f} \quad (5)$$

Where ∇ is the differential operator defined as $\nabla = [\frac{\partial}{\partial x_1}, \frac{\partial}{\partial x_2}, \dots, \frac{\partial}{\partial x_n}]$ and \otimes is the Kronecker product. Note that accordingly, $\nabla \otimes \mathbf{h}$ is equivalent to the Jacobian matrix of \mathbf{h} .

Using these definitions, an observability matrix can be constructed as follows:

$$\mathcal{O} = \begin{bmatrix} \nabla \otimes \mathcal{L}_{\mathbf{f}}^0 \mathbf{h} \\ \nabla \otimes \mathcal{L}_{\mathbf{f}}^1 \mathbf{h} \\ \vdots \\ \nabla \otimes \mathcal{L}_{\mathbf{f}}^i \mathbf{h} \end{bmatrix}, \quad i \in \mathbb{N} \quad (6)$$

A system is locally weakly observable if the observability matrix is full rank [40]. This theory will be applied to the relative localization filter such that the conditions can be derived for which the filter is locally weakly observable.

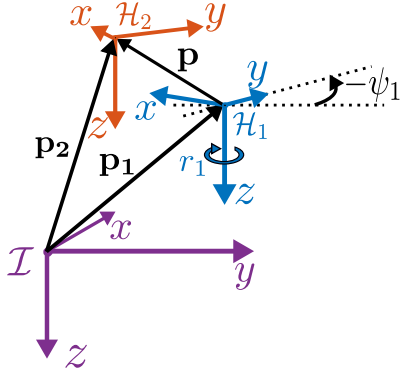


Fig. 1. Important reference frames used in this paper. Frame \mathcal{I} in purple is the earth-fixed North East Down frame (assumed to be inertial). Frames \mathcal{H}_1 (orange) and \mathcal{H}_2 (blue) are body fixed reference frames for drones 1 and 2 respectively.

B. Reference Frames

For the analyses that follow, consider the reference frames schematically depicted in figure 1.

Denoted by \mathcal{I} is the earth-fixed, North-East-Down (NED) reference frame, which is assumed to be an inertial frame of reference.

Denoted by \mathcal{H}_i , $i = 1, 2$ is a body-fixed reference frame belonging to drone i . Its origin is coincident with drone i 's centre of gravity and its location with respect to the \mathcal{I} frame is represented by the vector \mathbf{p}_i . The \mathcal{H}_i frame is defined to be a horizontal frame of reference, such that the z -axis of the \mathcal{H}_i frame remains parallel to that of the \mathcal{I} frame. The \mathcal{H}_i frame however is rotated with respect to the \mathcal{I} frame about the positive z -axis by an angle ψ_i , where ψ_i is the heading that drone i has with respect to North, also referred to as its yaw angle. The rate of change of ψ_i is represented by r_i .

Note that the \mathcal{H}_i frame is different from the more typical body-fixed frame \mathcal{B}_i that uses the three Euler angles for roll, pitch, and yaw to represent its orientation with respect to the \mathcal{I} frame. The reason for using the \mathcal{H}_i rather than the \mathcal{B}_i frame, is that it simplifies some kinematic relations later on in this paper, without having to impose additional assumptions such as the assumption that the roll and pitch angle of the drone are small. Of course the kinematics are even simpler in the \mathcal{I} frame, but establishing this common frame for every drone introduces the undesirable requirement for each drone to have knowledge of a common North direction. The \mathcal{H}_i frame thus forms a sort of compromise between the \mathcal{I} frame and the \mathcal{B}_i frame.

C. Nonlinear System Description

As mentioned earlier, assume for this analysis that it is drone 1 that attempts to estimate the relative position of drone 2. Define for that purpose the vector \mathbf{p} to be this relative position, such that $\mathbf{p} = \mathbf{p}_2 - \mathbf{p}_1$ (see figure 1). Furthermore, denote by \mathbf{v}_i and \mathbf{a}_i the linear velocities and accelerations of frame \mathcal{H}_i with respect to frame \mathcal{I} , expressed in frame \mathcal{H}_i , $i = 1, 2$.

Finally, let $\Delta\psi$ represent the difference in heading between drone 1 and 2, such that $\Delta\psi = \psi_2 - \psi_1$.

It is assumed from this point on that the drones are capable of measuring their own height. Since the \mathcal{H}_i frame is a horizontal frame of reference, the height can easily be treated as a separate dimension that does not influence the overall observability analysis if it is directly measured. For the sake of brevity, the height is therefore not included in the system description. The vectors for the relative position \mathbf{p} , the velocity \mathbf{v}_i , and the acceleration \mathbf{a}_i can thus be expanded as 2D vectors: $\mathbf{p}^\top = [p_x, p_y]^\top$, $\mathbf{v}_i = [v_{x,i}, v_{y,i}]^\top$, $\mathbf{a}_i = [a_{x,i}, a_{y,i}]^\top$, $i = 1, 2$.

In accordance with the earlier definition of the rate of change of ψ_i , the rate of change of $\Delta\psi$ is $\Delta\dot{\psi} = r_2 - r_1$. An important point to note is that the value for r_i is not equal to the yaw rate as would commonly be measured by an onboard rate gyroscope in the body frame \mathcal{B}_i . Instead, r_i can be expressed as:

$$r_i = \frac{\sin(\phi_i)}{\cos(\theta_i)} \tilde{q}_i + \frac{\cos(\phi_i)}{\cos(\theta_i)} \tilde{r}_i \quad (7)$$

with \tilde{q}_i and \tilde{r}_i representing the true pitch and yaw rate as would be measured by a rate gyroscope, and ϕ_i and θ_i being the roll and pitch angles of the drone. However, for the sake of simplicity the value for r_i will be referred to as the drone's yaw rate.

Similarly, the value for the linear acceleration of the \mathcal{H}_i frame expressed in coordinates of the \mathcal{H}_i frame, so \mathbf{a}_i , is not exactly equal to what is measured by the accelerometer on board. Instead, it is equal to:

$$\mathbf{a}_i = \begin{bmatrix} c(\theta_i) & s(\phi_i)s(\theta_i) & c(\phi_i)s(\theta_i) \\ 0 & c(\phi_i) & -s(\phi_i) \end{bmatrix} \mathbf{s}_i \quad (8)$$

where \mathbf{s}_i is the specific force measured in the body frame \mathcal{B}_i by the accelerometer of drone i . Furthermore, $c(\alpha)$ and $s(\alpha)$ represent short hand notation for $\cos(\alpha)$ and $\sin(\alpha)$ respectively. The matrix in this equation consists of the first two rows of the rotation matrix from the \mathcal{B}_i frame to the \mathcal{H}_i frame.

Define the complete state of the system to be $\mathbf{x} = [\mathbf{p}^\top, \Delta\psi, \mathbf{v}_1^\top, \mathbf{v}_2^\top]^\top$ and the known inputs to the system as $\mathbf{u}^\top = [\mathbf{a}_1^\top, \mathbf{a}_2^\top, r_1, r_2]^\top$. The continuous time state differential equations can be written as:

$$\dot{\mathbf{x}} = \mathbf{f}(\mathbf{x}, \mathbf{u}) = \begin{bmatrix} -\mathbf{v}_1 + \mathbf{R}\mathbf{v}_2 - \mathbf{S}_1\mathbf{p} \\ r_2 - r_1 \\ \mathbf{a}_1 - \mathbf{S}_1\mathbf{v}_1 \\ \mathbf{a}_2 - \mathbf{S}_2\mathbf{v}_2 \end{bmatrix} \quad (9)$$

Here, \mathbf{R} is the 2D rotation matrix from frame \mathcal{H}_2 to \mathcal{H}_1 , such that:

$$\mathbf{R} = \mathbf{R}(\Delta\psi) = \begin{bmatrix} \cos(\Delta\psi) & -\sin(\Delta\psi) \\ \sin(\Delta\psi) & \cos(\Delta\psi) \end{bmatrix} \quad (10)$$

The matrices \mathbf{S}_1 and \mathbf{S}_2 are the skew-symmetric matrix equivalent of the cross product, adapted to the 2D case. The matrix \mathbf{S}_i is equal to:

$$\mathbf{S}_i = \mathbf{S}_i(r_i) = \begin{bmatrix} 0 & -r_i \\ r_i & 0 \end{bmatrix}, i = 1, 2 \quad (11)$$

The variables \mathbf{a}_i and r_i , $i = 1, 2$ are *inputs* into the system and drone 1 must thus have knowledge of these values. These are however typically available from accelerometer and gyroscope data in combination with the appropriate relations given in equations 7 and 8.

Of course equation 9 needs to be complemented with an observation model. Apart from the height, which must be measured but is not included in this analysis, the drones should be able to measure the relative range between each other, along with their own and each other's velocities.

The analysis that follows aims to study the difference between a scenario where the above measurements are the only measurements and the scenario where the drones are additionally capable of observing their own heading, so ψ_1 and ψ_2 . The situation where the drones can observe a heading is referred to as \sum_A and the situation where a heading is not observed is referred to as \sum_B for convenience.

Sticking to the state as previously defined, the scenario where ψ_1 and ψ_2 are observed is equivalent to $\Delta\psi$ (the difference in headings) being observed. So for \sum_A , the following observation model can be defined:

$$\mathbf{y}_A = \mathbf{h}_A(\mathbf{x}) = \begin{bmatrix} h_{A1}(\mathbf{x}) \\ h_{A1}(\mathbf{x}) \\ \mathbf{h}_{A3}(\mathbf{x}) \\ \mathbf{h}_{A4}(\mathbf{x}) \end{bmatrix} = \begin{bmatrix} \frac{1}{2}\mathbf{p}^T\mathbf{p} \\ \Delta\psi \\ \mathbf{v}_1 \\ \mathbf{v}_2 \end{bmatrix} \quad (12)$$

Note that the observation equation $h_{A1}(\mathbf{x})$ is slightly modified with regards to the earlier mentioned measurements for the convenience of the observability analysis. Rather than observing the range itself between the two drones (i.e. $\|\mathbf{p}\|_2$), half the squared range is observed (i.e. $\frac{1}{2}\mathbf{p}^T\mathbf{p}$). This change is made to make the observability analysis more convenient without changing its result. Both $\|\mathbf{p}\|_2$ and $\frac{1}{2}\mathbf{p}^T\mathbf{p}$ contain the same information as far as observability of the system is concerned [38].

The second case that is studied is that where the headings of the drones are not observed at all. In this situation it is not possible to observe the difference in heading $\Delta\psi$ directly. For \sum_B , the observation model therefore becomes:

$$\mathbf{y}_B = \mathbf{h}_B(\mathbf{x}) = \begin{bmatrix} h_{B1}(\mathbf{x}) \\ \mathbf{h}_{B2}(\mathbf{x}) \\ \mathbf{h}_{B3}(\mathbf{x}) \end{bmatrix} = \begin{bmatrix} \frac{1}{2}\mathbf{p}^T\mathbf{p} \\ \mathbf{v}_1 \\ \mathbf{v}_2 \end{bmatrix} \quad (13)$$

The effect of this difference in the observation equation is studied in the following sections.

D. Observability analysis with common heading reference

First consider system \sum_A , such that the observation model is given by equation 12. The first entry in the observability matrix is equal to:

$$\nabla \otimes \mathcal{L}_f^0 \mathbf{h}_A = \nabla \otimes \mathbf{h}_A = \begin{bmatrix} \mathbf{p}^T & 0 & \mathbf{0}_{1x2} & \mathbf{0}_{1x2} \\ \mathbf{0}_{1x2} & 1 & \mathbf{0}_{1x2} & \mathbf{0}_{1x2} \\ \mathbf{0}_{2x2} & \mathbf{0}_{2x1} & \mathbf{I}_{2x2} & \mathbf{0}_{2x2} \\ \mathbf{0}_{2x2} & \mathbf{0}_{2x1} & \mathbf{0}_{2x2} & \mathbf{I}_{2x2} \end{bmatrix} \\ = \begin{bmatrix} \mathbf{p}^T & \mathbf{0}_{1x5} \\ \mathbf{0}_{5x2} & \mathbf{I}_{5x5} \end{bmatrix} \quad (14)$$

With \mathbf{I}_{nxn} representing the identity matrix of size $n \times n$ and $\mathbf{0}_{mxn}$ representing a matrix filled with zeros of size $m \times n$.

One can already deduce some important information from this first term that will simplify the subsequent analysis. First of all, note that for the higher order terms in the observability matrix, the last 5 columns will not contribute to increasing its rank, because these columns are already populated by the identity matrix. Furthermore, one can verify that the higher order terms in the observation matrix corresponding to the observations of $\Delta\psi$, \mathbf{v}_1 , and \mathbf{v}_2 only have terms in those last 5 columns because none of the higher order Lie derivatives corresponding to those observations depend on the state \mathbf{p} . For this reason, these need not be computed and are therefore omitted for brevity. The remainder of this analysis considers only the terms corresponding to observation $h_{A1}(\mathbf{x}) = \frac{1}{2}\mathbf{p}^T\mathbf{p}$.

The first order Lie derivative corresponding to the observation $h_{A1}(\mathbf{x}) = \frac{1}{2}\mathbf{p}^T\mathbf{p}$ is equal to:

$$\mathcal{L}_f^1 h_{A1} = \mathbf{p}^T(-\mathbf{v}_1 + \mathbf{R}\mathbf{v}_2 - \mathbf{S}_1\mathbf{p}) \quad (15)$$

Next, remembering that \mathbf{S}_1 is a skew symmetric matrix, such that $\mathbf{S}_1 + \mathbf{S}_1^T = \mathbf{0}_{2x2}$, the following identity is obtained:

$$\frac{\partial \mathbf{p}^T \mathbf{S}_1 \mathbf{p}}{\partial \mathbf{p}} = \mathbf{p}^T (\mathbf{S}_1 + \mathbf{S}_1^T) = \mathbf{p}^T (\mathbf{0}_{2x2}) = \mathbf{0}_{1x2} \quad (16)$$

Using this identity it is easy to verify that the second term in the observation matrix corresponding to $h_{A1}(\mathbf{x})$ is:

$$\nabla \mathcal{L}_f^1 h_{A1} = \begin{bmatrix} -\mathbf{v}_1 + \mathbf{R}\mathbf{v}_2 \\ \mathbf{p}^T \frac{\partial \mathbf{R}}{\partial \Delta\psi} \mathbf{v}_2 \\ -\mathbf{p} \\ \mathbf{R}^T \mathbf{p} \end{bmatrix}^T \quad (17)$$

Now, it is possible to continue calculating higher order terms for the observability matrix, but in practice this is not necessary. The first term of the observability matrix, as shown in equation 14 already presents a matrix of rank 6. Since the state is of size 7, this means that only 1 more linearly independent row needs to be added to the observability matrix to demonstrate local weak observability of the system. It is of practical interest to study the scenarios in which the system is locally weakly observable with a minimum amount of Lie derivatives involved in the analysis. This is due to the fact that in practice all signals are noisy, and continuous differentiation of a noisy signal will inevitably lead to increasingly noisy signals. It will be demonstrated that the terms presented in equation 17 are sufficient under certain conditions to make the observability matrix full rank.

As mentioned, equation 14 already shows that the last five columns of the observability matrix are no longer of interest

to increase its rank. Furthermore, only the observation of $h_{A1}(\mathbf{x}) = \frac{1}{2}\mathbf{p}^\top \mathbf{p}$ provides non-zero terms in the first two columns of the observability matrix. Therefore, the following matrix can be constructed by collecting the terms of the first two columns in the observation matrix belonging to observation $h_{A1}(\mathbf{x})$:

$$\mathbf{M}_A = \begin{bmatrix} \mathbf{p}^\top \\ -\mathbf{v}_1^\top + \mathbf{v}_2^\top \mathbf{R}^\top \end{bmatrix} \quad (18)$$

where the first term is from the zeroth order Lie derivative (see equation 14) and the second term from the first order Lie derivative (see equation 17).

The system is thus observable with a minimum amount of Lie derivatives if the matrix given by 18 has two linearly independent rows. By the definition of linear independence, this means that the following condition must hold to guarantee local weak observability of the system:

$$-\mathbf{v}_1 + \mathbf{R}\mathbf{v}_2 \neq c\mathbf{p} \quad (19)$$

where c is an arbitrary constant.

This condition essentially tells us that the relative velocity of the two drones should not be a multiple of the relative position vector between the two drones.

It can be difficult to intuitively envision what this condition means in practice. By inspecting equation 19, however, we can find more intuitive conditions that must also be met for equation 19 to hold. These conditions can be described as follows:

- $\mathbf{p} \neq \mathbf{0}_{2 \times 1}$ (20)

- $\mathbf{v}_1 \neq \mathbf{0}_{2 \times 1}$ or $\mathbf{v}_2 \neq \mathbf{0}_{2 \times 1}$ (21)

- $\mathbf{v}_1 \neq \mathbf{R}\mathbf{v}_2$ (22)

The first condition tells us that the x and y coordinates of the relative position of drone 2 with respect to drone 1 should not be equal to 0. In practice this would only be possible if the drones were separated by height, for otherwise their physical dimension would prevent this condition from occurring.

The second condition tells us that one of the two drones needs to be moving to render the filter observable, and that the observability is indifferent to which of the drones is moving (hence the `or` condition).

The third condition tells us that the drones should not be moving in parallel at the same speed (note the rotation matrix \mathbf{R} to transform \mathbf{v}_2 to the \mathcal{H}_1 frame).

Whilst these three conditions are indeed easier to consider, it should be noted that these three conditions combined are only a subset of the conditions imposed by equation 19. For example, the scenario where drone 2 is stationary, and drone 1 flies straight towards drone 2, does not violate these three conditions. It does however violate equation 19. To guarantee the observability of a state and input combination, it should therefore be checked against the full condition in equation 19.

E. Observability analysis without a common heading reference

After getting a sense of what conditions should be met to make system \sum_A locally weakly observable, it would be

interesting to see how this compares to the system where the heading dependency is no longer present. Therefore, consider now system \sum_B whose observation equation is given by equation 13, which does not include an observation of the state $\Delta\psi$. For this system, the first term in the observability matrix becomes:

$$\nabla \otimes \mathcal{L}_f^0 h_B = \nabla \otimes h_B = \begin{bmatrix} \mathbf{p}^\top & 0 & \mathbf{0}_{1 \times 2} & \mathbf{0}_{1 \times 2} \\ \mathbf{0}_{2 \times 2} & \mathbf{0}_{2 \times 1} & \mathbf{I}_{2 \times 2} & \mathbf{0}_{2 \times 2} \\ \mathbf{0}_{2 \times 2} & \mathbf{0}_{2 \times 1} & \mathbf{0}_{2 \times 2} & \mathbf{I}_{2 \times 2} \end{bmatrix} \quad (23)$$

The term is very similar to the one shown previously in equation 14. The important difference is that the row corresponding to the observation of $\Delta\psi$ has disappeared. This means that the third column in 23 is now all 0's. Consequently, the matrix is only rank 5, compared to the rank 6 that was found previously. Since the state size is still 7, a minimum of two more independent rows must be added to the observability matrix to render the system locally weakly observable. Again only the terms corresponding to the observation $h_{B1}(\mathbf{x}) = \frac{1}{2}\mathbf{p}^\top \mathbf{p}$ have terms that could increase the rank of the observability matrix. This means that this time a minimum of two more Lie derivatives must be calculated.

It can be verified that the first derivative $\mathcal{L}_f^1 h_{B1}$ and thus its state-derivative $\nabla \mathcal{L}_f^1 h_{B1}$ are exactly the same as calculated for \sum_A . These therefore need not be calculated anymore and are given by equations 15 and 17 respectively.

The second order Lie derivative is equal to:

$$\begin{aligned} \mathcal{L}_f^2 h_{B1} = & (-\mathbf{v}_1^\top + \mathbf{v}_2^\top \mathbf{R}^\top)(-\mathbf{v}_1 + \mathbf{R}\mathbf{v}_2 - \mathbf{S}_1 \mathbf{p}) \quad (24) \\ & + \mathbf{p}^\top \frac{\partial \mathbf{R}}{\partial \Delta\psi} \mathbf{v}_2(r_2 - r_1) - \mathbf{p}^\top (\mathbf{a}_1 - \mathbf{S}_1 \mathbf{v}_1) \\ & + \mathbf{p}^\top \mathbf{R}^\top (\mathbf{a}_2 - \mathbf{S}_2 \mathbf{v}_2) \end{aligned}$$

Some of these terms drop out if equation 24 is expanded. For example the yaw rate of drone 1, r_1 , cancels out completely. Without any additional assumptions, equation 24 can be reduced to:

$$\begin{aligned} \mathcal{L}_f^2 h_{B1} = & \mathbf{v}_1^\top \mathbf{v}_1 + \mathbf{v}_2^\top \mathbf{v}_2 - 2\mathbf{v}_1^\top \mathbf{R}\mathbf{v}_2 + \mathbf{p}^\top \frac{\partial \mathbf{R}}{\partial \Delta\psi} \mathbf{v}_2 r_2 \\ & - \mathbf{p}^\top \mathbf{a}_1 + \mathbf{p}^\top \mathbf{R}\mathbf{a}_2 - \mathbf{p}^\top \mathbf{R}^\top \mathbf{S}_2 \mathbf{v}_2 \end{aligned} \quad (25)$$

The state-derivative of $\mathcal{L}_f^2 h_{B1}$ can then be shown to be equal to equation 26. Note that again some terms cancel out, this step has been omitted for brevity.

$$\nabla \mathcal{L}_f^2 h_{B1} = \begin{bmatrix} \mathbf{a}_1 + \mathbf{R}\mathbf{a}_2 \\ -2\mathbf{v}_1^\top \frac{\partial \mathbf{R}}{\partial \Delta\psi} \mathbf{v}_2 + \mathbf{p}^\top \frac{\partial \mathbf{R}}{\partial \Delta\psi} \mathbf{a}_2 \\ 2\mathbf{v}_1 - 2\mathbf{R}\mathbf{v}_2 \\ -2\mathbf{R}^\top \mathbf{v}_1 + 2\mathbf{v}_2 \end{bmatrix}^\top \quad (26)$$

Just like before, a part of the observation matrix can be extracted for analysis. This time, the first three columns in the observation matrix (as opposed to two) are collected for the observation $h_{B1}(\mathbf{x}) = \frac{1}{2}\mathbf{p}^\top \mathbf{p}$. Also, this time the terms up to

and including the second order Lie derivative are minimally needed to obtain a full rank observability matrix. The following matrix is obtained:

$$\mathbf{M}_B = \begin{bmatrix} \mathbf{p}^\top & 0 \\ -\mathbf{v}_1^\top + \mathbf{v}_2^\top \mathbf{R}^\top & \mathbf{p}^\top \frac{\partial \mathbf{R}}{\partial \Delta \psi} \mathbf{v}_2 \\ -\mathbf{a}_1^\top + \mathbf{a}_2^\top \mathbf{R}^\top & -2\mathbf{v}_1^\top \frac{\partial \mathbf{R}}{\partial \Delta \psi} \mathbf{v}_2 + \mathbf{p}^\top \frac{\partial \mathbf{R}}{\partial \Delta \psi} \mathbf{a}_2 \end{bmatrix} \quad (27)$$

Obtaining the conditions for which this is a full rank matrix is in this case somewhat less obvious due to the plethora of terms. Rather than directly demonstrating linear independence of the three rows in equation 27, the determinant $|\mathbf{M}_B|$ may be computed and demonstrated to be non-zero. This is done as follows.

Recall that $\mathbf{p}^\top = [p_x, p_y]$. Furthermore, suppose $-\mathbf{v}_1^\top + \mathbf{v}_2^\top \mathbf{R}^\top = [a, b]$ and $-\mathbf{a}_1^\top + \mathbf{a}_2^\top \mathbf{R}^\top = [c, d]$. Then matrix \mathbf{M}_B can be written as:

$$\mathbf{M}_B = \begin{bmatrix} p_x & p_y & 0 \\ a & b & \mathbf{p}^\top \frac{\partial \mathbf{R}}{\partial \Delta \psi} \mathbf{v}_2 \\ c & d & -2\mathbf{v}_1^\top \frac{\partial \mathbf{R}}{\partial \Delta \psi} \mathbf{v}_2 + \mathbf{p}^\top \frac{\partial \mathbf{R}}{\partial \Delta \psi} \mathbf{a}_2 \end{bmatrix} \quad (28)$$

The determinant of \mathbf{M}_B can be computed using a cofactor expansion along the last column of \mathbf{M}_B . This results in:

$$|\mathbf{M}_B| = -\mathbf{p}^\top \frac{\partial \mathbf{R}}{\partial \Delta \psi} \mathbf{v}_2 (dp_x - cp_y) + (-2\mathbf{v}_1^\top \frac{\partial \mathbf{R}}{\partial \Delta \psi} \mathbf{v}_2 + \mathbf{p}^\top \frac{\partial \mathbf{R}}{\partial \Delta \psi} \mathbf{a}_2) (bp_x - ap_y) \quad (29)$$

Now, the following identity can be used:

$$bp_x - ap_y = [a \ b] \begin{bmatrix} -p_y \\ p_x \end{bmatrix} = [a \ b] \mathbf{A} \begin{bmatrix} p_x \\ p_y \end{bmatrix}, \quad (30)$$

$$\text{where } \mathbf{A} = \begin{bmatrix} 0 & -1 \\ 1 & 0 \end{bmatrix}.$$

Substituting back the original expressions for $[a, b]$, $[c, d]$, and $[p_x, p_y]$, the determinant of \mathbf{M}_B becomes:

$$|\mathbf{M}_B| = -\mathbf{p}^\top \frac{\partial \mathbf{R}}{\partial \Delta \psi} \mathbf{v}_2 (-\mathbf{a}_1^\top + \mathbf{a}_2^\top \mathbf{R}^\top) \mathbf{A} \mathbf{p} + (-2\mathbf{v}_1^\top \frac{\partial \mathbf{R}}{\partial \Delta \psi} \mathbf{v}_2 + \mathbf{p}^\top \frac{\partial \mathbf{R}}{\partial \Delta \psi} \mathbf{a}_2) (-\mathbf{v}_1^\top + \mathbf{v}_2^\top \mathbf{R}^\top) \mathbf{A} \mathbf{p} \quad (31)$$

This can be simplified and written as:

$$|\mathbf{M}_B| = \left[\mathbf{p}^\top \frac{\partial \mathbf{R}}{\partial \Delta \psi} (-\mathbf{a}_2 \mathbf{v}_1^\top + \mathbf{v}_2 \mathbf{a}_1^\top) + 2 \mathbf{v}_1^\top \frac{\partial \mathbf{R}}{\partial \Delta \psi} (\mathbf{v}_2 \mathbf{v}_1^\top - \mathbf{v}_2 \mathbf{v}_2^\top \mathbf{R}^\top) \right] \mathbf{A} \mathbf{p} \quad (32)$$

This system is thus locally weakly observable with a minimum amount of Lie derivatives if $|\mathbf{M}_B|$ is non-zero. Due to the specific properties of the \mathbf{A} matrix in this determinant (see

equation 30), the following equation must hold to render the determinant $|\mathbf{M}_B|$ non-zero:

$$\mathbf{p}^\top \frac{\partial \mathbf{R}}{\partial \Delta \psi} (-\mathbf{a}_2 \mathbf{v}_1^\top + \mathbf{v}_2 \mathbf{a}_1^\top) + 2 \mathbf{v}_1^\top \frac{\partial \mathbf{R}}{\partial \Delta \psi} (\mathbf{v}_2 \mathbf{v}_1^\top - \mathbf{v}_2 \mathbf{v}_2^\top \mathbf{R}^\top) \neq k \mathbf{p}^\top \quad (33)$$

where k is an arbitrary constant.

This equation is even more difficult to intuitively find a meaning for than the one found before in equation 19. Just like before, however, we can find a more intuitive subset of conditions that also definitely must be met for a system to be observable. These conditions are given by:

$$\bullet \quad \mathbf{p} \neq \mathbf{0}_{2x1} \quad (34)$$

$$\bullet \quad (\mathbf{v}_1 \neq \mathbf{0}_{2x1} \text{ or } \mathbf{a}_1 \neq \mathbf{0}_{2x1}) \text{ and } (\mathbf{v}_2 \neq \mathbf{0}_{2x1} \text{ or } \mathbf{a}_2 \neq \mathbf{0}_{2x1}) \quad (35)$$

$$\bullet \quad \mathbf{v}_1 \neq s \mathbf{R} \mathbf{v}_2 \text{ or } (\mathbf{a}_1 \neq \mathbf{0}_{2x1} \text{ or } \mathbf{a}_2 \neq \mathbf{0}_{2x1}) \quad (36)$$

with s an arbitrary constant.

The first of these conditions again tells us that the determinant $|\mathbf{M}_B|$ is zero if the x and y coordinates of the origins of frames \mathcal{H}_1 and \mathcal{H}_2 coincide. This condition is the same as for \sum_A .

The second condition tells us that both drones need to be moving. This movement may be either through having a non-zero velocity, or through having a non-zero acceleration.

The third condition tells us that the drones may not move in parallel *unless* at least one of the drones is also accelerating at the same time. Note that this time the drones are now not allowed to move in parallel regardless of whether they are moving at the same speed or not (notice the scalar multiple s). The equivalent condition for \sum_A only specified that the drones may not move in parallel at the same speed.

Just like before, the three intuitive conditions described here are only a subset of the conditions imposed by equation 33. This again means that there are state and input combinations that satisfy the three intuitive conditions, but that do not satisfy equation 33.

In order to still give some clarification as to what the implications are of the full unobservability condition in equation 33, we can use numerical optimization methods to further investigate this condition.

Using the Nelder-Mead simplex method for example, it is possible to find points in the state and input space that violate the full observability condition, but that do not violate the intuitive conditions.

Two examples of numerically obtained situations that are unobservable are given in figures 2 and 3. The relative position vector \mathbf{p} , and the velocities and accelerations of both drones \mathbf{v}_i and \mathbf{a}_i , $i = 1, 2$ are geometrically depicted as arrows in the figures. The vectors \mathbf{v}_2 and \mathbf{a}_2 are already rotated to the \mathcal{H}_1 frame for easier evaluation.

Indeed the scenarios in both figures do not violate any of the intuitive conditions given by equations 34 to 36. The relative position is non-zero, both drones have non-zero velocities and accelerations, and the velocity vectors are not parallel.

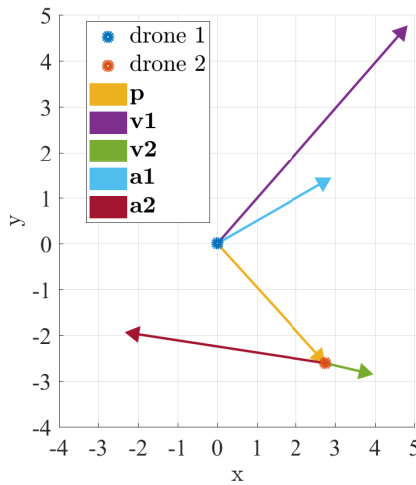


Fig. 2. Geometric display of an unobservable state and input combination

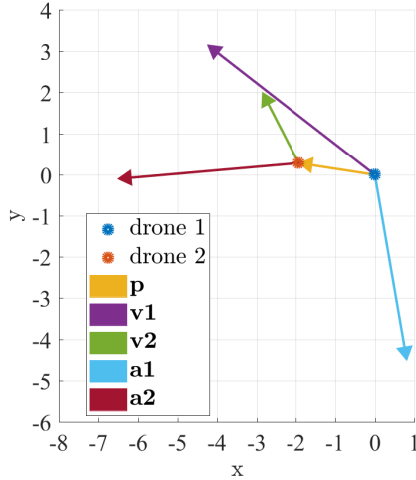


Fig. 3. Geometric display of an unobservable state and input combination

In order to gain more insight into these conditions, it is possible to evaluate how the observability of the system would change if the relative position \mathbf{p} between the drones would change. By varying the p_x and p_y values of the vector \mathbf{p} around the originally obtained values for \mathbf{p} as given in the figures, it is possible to generate a color map that indicates the observability of the system for different relative positions, given the corresponding velocities and accelerations depicted in figures 2 and 3.

To construct such a color map, a measure for the observability of the system is needed. This measure can be obtained by interpreting the meaning of equation 33. It essentially tells us that the left hand side of the equation should not be parallel to the relative position vector \mathbf{p} . A good measure of observability is thus how far away the left hand side of equation 33 is from being parallel to \mathbf{p} . Whether or not two vectors are parallel

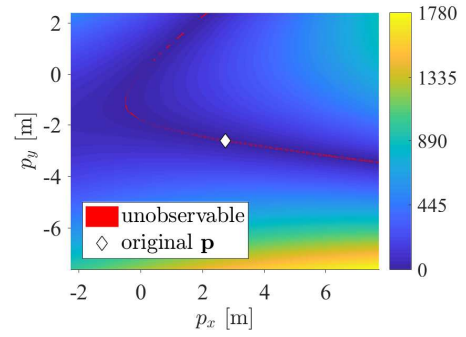


Fig. 4. Colour map of observability for different relative positions. The velocities and accelerations of the drones are kept as depicted by figure 2 and the values for $\mathbf{p}^\top = [p_x, p_y]^\top$ are varied over a 5 m^2 range.

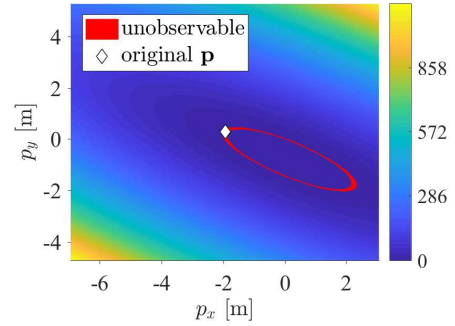


Fig. 5. Colour map of observability for different relative positions. The velocities and accelerations of the drones are kept as depicted by figure 3 and the values for $\mathbf{p}^\top = [p_x, p_y]^\top$ are varied over a 5 m^2 range.

can be tested with the cross product of two vectors. The cross product is zero if they are parallel and non-zero otherwise. The absolute value of the cross product is used as a measure of the observability of the system and will be used to construct the following color maps.

The color maps for the unobservable conditions in figures 2 and 3 are given in figures 4 and 5 respectively. When the cross product is less than a value of 1, it is considered unobservable. In reality only if the cross product is truly 0 it represents an unobservable condition, but this point will hardly be visible on the maps, if at all.

Both colour maps clearly show a non-linear relationship between the relative position vector \mathbf{p} and the observability of the system. Moreover, both maps show a different non-linear relationship. Figure 4 shows more of a hyperbolic relationship, whereas the unobservable region in figure 5 looks more elliptical.

It can be shown that different conditions show yet other relationships between the observability of the system for different relative positions \mathbf{p} . Moreover, these relationships only show what happens in two dimensions (for the two entries in the vector \mathbf{p}). In reality, the observability condition in equation 33 presents an 11 dimensional problem. It is therefore still difficult to deduce general rules from these results.

What all of the color maps do have in common is that the unobservable relative positions are in all cases vastly outnumbered by the observable relative positions. Changing in the position vector in the order of centimeters can already move the system away from the unobservable region. This is a property that will be used later on in the design of a leader-follower control method in section IV.

Note that especially this last conclusion is different than what would be observed for situations that would violate any of the more intuitive conditions in equations 35 and 36. For example, if the condition of parallel flight in equation 36 is violated, then any value for \mathbf{p} would result in an unobservable system, rather than just a few sparse values. It is therefore not without merit to consider these conditions separately.

F. Comparison of the two systems

Finally, the results from the observability analysis of both systems will be compared. This will answer the question of what practical implications there are when moving from a system that relies on a common heading reference, to a system that does not.

One of the primary results of the analysis is the fact that removing the relative heading measurement results in a system that requires at least *one extra Lie derivative* in the range observation to make the system locally weakly observable. This is an important result because it tells us that the heading-independent system \sum_B relies more heavily on the range equation than \sum_A . Without a heading observation, the information in the range signal is now used to estimate a total of three states as opposed to two in \sum_A . Some of this information is contained in the second derivative of the range observation. It is a well known fact that derivatives of a noisy signal become more and more noisy. In practice this means that any system that wishes to perform range-only relative localization without a heading dependency needs an *accurate and low-noise range observation*.

Another important result is that the criteria posed for \sum_B specify that *both drones must be moving*. Contrarily, the criteria for \sum_A specify that only one of the drones must be moving. Whilst this result might not be as relevant when two drones are considered (as they are typically moving), this result is very important for other applications of range-based relative localization. Think for example of the case where a single static beacon is used to estimate the position of a flying drone using range only sensing and communication. The results of this analysis show that \sum_B is not observable in this case, and thus a common heading reference must be observed for such a system to work (or the drone must track the beacon and communicate its estimate to the beacon). Note that in the case where one of the participants is not moving it can be shown that even the higher order Lie derivatives in \sum_B will not succeed in making the observability matrix full rank, so that this statement generally holds.

A third difference is the condition regarding parallel movement of the two drones. \sum_A specifies that the drones should not move in parallel at the same speed (which can thus be translated to mean that there should be a non-zero relative

velocity between the two drones). \sum_B specifies that *the drones should not be moving in parallel regardless of speed*. So even if the second drone were to be moving twice as fast as the first, the filter would not be observable if the direction of movement is the same. \sum_B is however able to bypass this condition in some cases if either of the drones is also simultaneously accelerating. It can be shown that \sum_A is similarly able to bypass the parallel motion condition with acceleration, but a second order Lie derivative would be necessary in this case.

III. VERIFICATION THROUGH SIMULATIONS

This section verifies the conclusions drawn from the analytical observability analysis. First of all the filter that is used to represent the studied problem will be introduced. Afterwards, the conclusions drawn earlier are verified. At first, a kinematic, noise-free study is performed to confirm the differences in the observability conditions for \sum_A and \sum_B . Afterwards, the influence of noise and disturbances on the filter are studied for situations that are known to be observable.

A. Filter Design

The choice of filter throughout the rest of this paper is an Extended Kalman Filter (EKF). This choice was made because this type of filter fits intuitively with how the state-space system was described in section II. The EKF also uses a state differential model and an observation model. The state differential model can thus be kept exactly like the one given earlier in equation 9. The observation models for \sum_A and \sum_B is also kept almost entirely the same as given before in equations 12 and 13, with the only adjustment that the range $\|\mathbf{p}\|_2$ is observed, rather than half the squared range $\frac{1}{2}\mathbf{p}^T\mathbf{p}$. Furthermore, using the EKF is in line with earlier research on range-based relative localization, where it was successfully implemented in practice [10].

An EKF has parameters that need to be tuned, namely the system and measurement noise matrices, the initial state, and the initial state covariance matrix. The initial state is an important setting that will be described where appropriate in the next sections. The other matrices are always tuned to correspond to the actual expected values. The measurement noise matrix is thus tuned based on the expected noises on the measurements and similarly for the system noise matrix. However, since some of the simulations also make use of perfect measurements (with zero noise) and since a zero noise entry in the measurement noise matrix is not possible, the corresponding entries are then given a small value of 0.1.

B. Kinematic, noise-free study of unobservable situations

In the first simulated study, the two ‘drones’ that are studied have kinematic trajectories that can be analytically described. The drones also have perfect noise-free knowledge of the inputs and measurements. The kinematic and noise-free situation is used to confirm conclusions drawn in the observability analysis performed in section II.

The two drones involved in the EKF are designated drone 1 and drone 2. In this context, drone 1 is the host of the EKF

and thus attempts to track the relative position of drone 2. For clarity, this drone is sometimes referred to as the host of the filter. Drone 2 is the drone whose position is tracked by drone 1. It does not run an EKF. For clarity, this drone is sometimes referred to as the tracked drone. The following three scenarios are studied:

- 1) Drone 1 (host) is moving and drone 2 (tracked) is stationary.
- 2) Drone 1 (host) is stationary and drone 2 (tracked) is moving.
- 3) Drone 1 (host) and 2 (tracked) are both moving in parallel to each other at different speeds.

These scenarios have been specifically chosen due to the fact that they represent the intuitive conditions where \sum_A was still demonstrated to be observable, but \sum_B is not. These are limit cases and therefore provide valuable verification of the analytically found differences between both systems.

The simulation will show whether these different scenarios have convergent EKFs or not. The focus of this analysis is on the estimation of the relative position \mathbf{p} and the relative heading $\Delta\psi$. Since the velocities are observed directly in both observation models, these are observable regardless of the situation. For this reason, these states will not be shown.

As mentioned, the EKF needs to have initial values for the state estimate. The initial velocities of drone 1 and 2 are initialized to their true value, since these are not the variables of interest in this analysis. The initial position and relative heading are initialized with an error, the specifics of which will be given in the respective scenarios. The yaw rates and headings of both drones are kept at 0 rad/s and rad respectively. The EKF runs at a frequency of 50 Hz.

The error measure throughout this paper is the Mean Absolute Error (MAE). The separate x and y errors in the relative location estimate \mathbf{p} are combined according to the norm $\|\mathbf{p}\|_2$. This choice was made because the separate errors in x and y directions offer little additional insight and are mostly very similar. The cases will now be studied.

1) Drone 1 (host) moving, drone 2 (tracked) stationary

It is known from the previous analysis that in this scenario, \sum_A is locally weakly observable, whilst \sum_B is not observable. This result is therefore expected to be reflected in the simulation as well.

In this scenario the position of drone 2 is equal to $\mathbf{p}_{2,0}^\top = [1, 1]^\top$ and drone 2 has no velocity or acceleration. The initial position of drone 1 is $\mathbf{p}_{1,0}^\top = [0, 0]^\top$. However, drone 1 has a constant velocity $\mathbf{v}_1^\top = [1, 0]^\top$. The initial guess for the relative position and heading of drone 2 is $[\hat{\mathbf{p}}_0^\top, \hat{\Delta\psi}_0]^\top = [0.1, 0.1, 1]^\top$. Notice that the initial estimation error in p_x , p_y , and $\Delta\psi$ is thus 0.9, 0.9, and 1 respectively.

According to the analytical observability result, this situation should be locally weakly observable for \sum_A . Indeed, as can be seen in figure 6, both the relative position \mathbf{p} error and the relative heading $\Delta\psi$ error quickly converge to 0.

Contrarily, the observability analysis has shown that \sum_B is not locally weakly observable in this case, because the second condition is violated. One of the drones is not moving. Interestingly enough, figure 7 shows that the $\|\mathbf{p}\|_2$ error converges

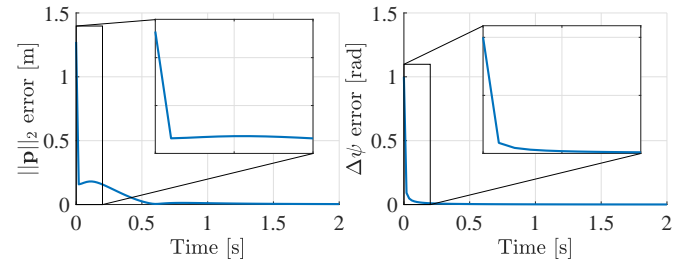


Fig. 6. \sum_A EKF convergence for case 1: drone 1 (host) moving, drone 2 (tracked) stationary

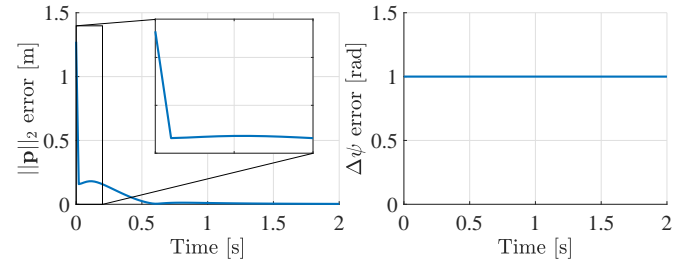


Fig. 7. \sum_B EKF convergence for case 1: drone 1 (host) moving, drone 2 (tracked) stationary

to 0 just as rapidly as for \sum_A . Indeed, the unobservable part of the system in this case is in fact in the $\Delta\psi$ state, which does not converge. This is a favorable result, since the relative position is typically the variable of interest, rather than the difference in heading.

The reason that this behavior occurs lies in the information provided by the first state differential equation. This equation tells us that $\dot{\mathbf{p}} = -\mathbf{v}_1 + \mathbf{R}\mathbf{v}_2 - \mathbf{S}_1\mathbf{p}$. The only dependency that this equation has on the relative heading $\Delta\psi$ is in the rotation matrix \mathbf{R} . Therefore, as long as \mathbf{v}_2 is equal to 0, the differential equation for $\dot{\mathbf{p}}$ has no dependency on the relative heading between the two drones. The convergence of \mathbf{p} therefore remains unaffected. This situation changes, of course, when it is in fact \mathbf{v}_2 that is non-zero and \mathbf{v}_1 that is zero. This case is studied next.

2) Drone 1 (host) stationary, drone 2 (tracked) moving

For this case, all of the parameters are the same as for case 1, with the only difference being that now $\mathbf{v}_1 = 0$ and $\mathbf{v}_2^\top = [1, 0]^\top$.

Just like before, the analytical observability analysis has shown that this case is locally weakly observable for \sum_A . Indeed, it can be seen in figure 8 that both the errors for \mathbf{p} and $\Delta\psi$ converge rapidly to 0.

The observability analysis has shown that \sum_B is not locally weakly observable in this case. As expected, this time figure 9 shows that both $\|\mathbf{p}\|_2$ and $\Delta\psi$ do not converge and that $\|\mathbf{p}\|_2$ even appears to diverge.

This time, because \mathbf{v}_2 is not equal to 0, the state differential equation for the relative position of drone 2 has a dependency

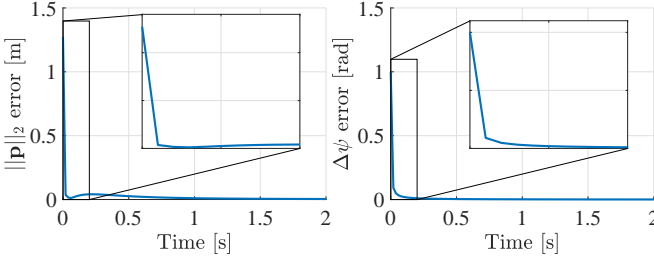


Fig. 8. \sum_A EKF convergence for case 2: drone 1 (host) stationary, drone 2 (tracked) moving

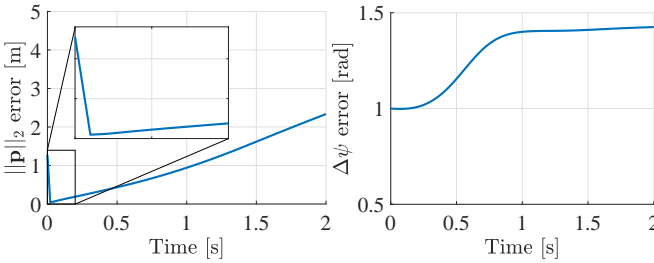


Fig. 9. \sum_B EKF convergence for case 2: drone 1 (host) stationary, drone 2 (tracked) moving

on the relative heading state $\Delta\psi$. Because $\Delta\psi$ does not converge to its true value, and eventually settles at an error of approximately 1.5 rad, there is a large inaccuracy in the state differential equation for \dot{p} . This consequently results in an ever increasing error in p , since drone 1 essentially ‘thinks’ that drone 2 is flying in a different direction than it really is.

This is precisely the reason why it is generally not possible for a stationary vehicle (or beacon) to be tracking a moving vehicle using range-only measurements and velocity information without a common heading reference. Contrarily, it is possible for a moving vehicle to be tracking a stationary vehicle or beacon’s position. This is entirely caused by the fact that a vehicle will always be ‘aware’, in its own body frame, of the direction it is moving in and hence does not need a convergent estimate of the relative heading with respect to the vehicle it is tracking. However, when the vehicle it is tracking does move, it needs this convergent estimate of the relative heading to know what direction the other is moving.

3) Drone 1 (host) and drone 2 (tracked) moving in parallel at different speeds

Finally, the case where both drones are moving in parallel, but at different speeds is studied. Again, most of the parameters are kept the same as those presented under case 1. This time, however, the velocity of drone 2 is set to $v_2^\top = [1, 0]^\top$ and the velocity of drone 1 is set in a parallel direction, but with twice the magnitude ($v_1^\top = 2v_2^\top = [2, 0]^\top$).

According to the observability analysis, this is again one of the limit cases where \sum_A is still just observable, but \sum_B is not. Indeed, figure 10 shows convergent behavior for \sum_A ,

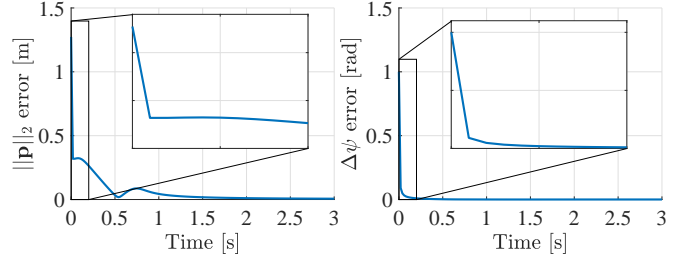


Fig. 10. \sum_A EKF convergence for case 3: drone 1 (host) and 2 (tracked) moving in parallel

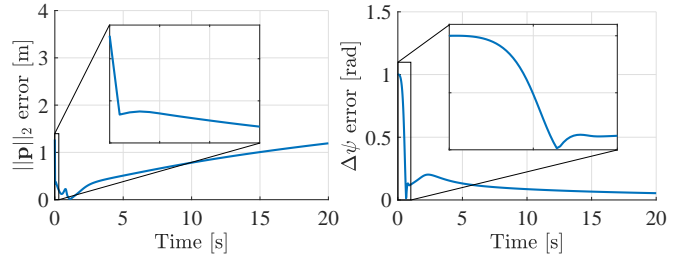


Fig. 11. \sum_B EKF convergence for case 3: drone 1 (host) and 2 (tracked) moving in parallel

whereas figure 11 shows divergence for \sum_B .

Note that the filter for \sum_B has a decreasing error in $\Delta\psi$. However, the convergence for $\Delta\psi$ is very slow (notice how this situation has been simulated for a much longer time than the previous cases). Furthermore, the error for p continues to rise indefinitely.

This result concludes the noise-free simulations that compare the performance of the filters for \sum_A and \sum_B . These simulations verify that indeed the conclusions regarding the differences between the two filters in section II also hold true when translated to a simulation environment.

C. Kinematic, noisy range measurements study of observable situation

Whilst a noise-free study provides a means to demonstrate the feasibility of the proposed filter and can verify the differences between \sum_A and \sum_B , it is also important to study the filter’s performance when presented to noisy data. Not only is this more closely resemblant of the performance of the filter in practice, but it can also be used to verify one of the main conclusions that were drawn in the observability study, namely that \sum_B needs information present in the second derivative of the range data to be observable, compared to only a first derivative for \sum_A . It is consequently expected that with all other parameters fixed, \sum_B will perform increasingly worse as the range data becomes more noisy. For these reasons, a second simulation study is performed for the scenario of noisy data.

For this study, the desire is to steer away from any of the scenarios that were shown to be unobservable in the

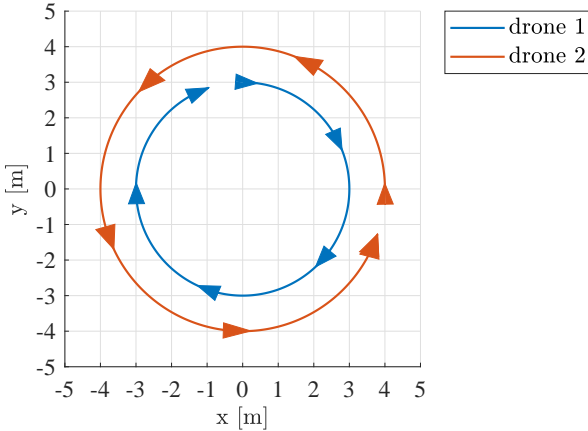


Fig. 12. Two circular trajectories for drone 1 and 2

previous sections. The purpose now is to study both filter's performances for the case where the filters *are* known to be observable, in order to see how both filters compare when both are observable. For this reason, the trajectories for drone 1 (host) and drone 2 (tracked) are designed so as to stay clear of the unobservable situations and to excite the filter effectively through relative motion. The trajectories that are studied are perfectly circular and the drones fly at the same height. The trajectories of the drones are depicted in figure 12.

Consider the trajectory described in polar coordinates $[\rho, \theta]$. Drone 1 flies a circular motion at an angular velocity $\dot{\theta}_1 = \omega_1$ with radius ρ_1 , and drone 2 flies at angular velocity $\dot{\theta}_2 = \omega_2$ with radius ρ_2 . To ensure that both drones have sufficient relative motion, one drone flies clockwise and the other counter clockwise, such that $\omega_1 = -\omega_2$. Moreover, drone 1's trajectory is offset with respect to drone 2's trajectory by 1 meter in range and by 90° in angle, such that $\rho_1 = \rho_2 - 1$ and $\theta_1 = \theta_2 + \frac{\pi}{2}$.

The range offset in the trajectories ensures that the situation $\mathbf{p} = \mathbf{0}$ is avoided, and the angle offset ensures that the relative velocities are distributed more or less equally in x and y directions. Note that for simplicity, both drones keep a steady heading such that $\psi_1 = \psi_2$ and $r_1 = r_2 = 0$.

The trajectories can thus analytically be described as follows, switching back to cartesian coordinates. Drone 2's position vector in time is given by:

$$\mathbf{p}_2(t) = \begin{bmatrix} \rho_2 \cos(\omega_2 t) \\ \rho_2 \sin(\omega_2 t) \end{bmatrix} \quad (37)$$

Drone 1's position vector in time can be described by:

$$\begin{aligned} \mathbf{p}_1(t) &= \begin{bmatrix} (\rho_2 - 1) \cos(-\omega_2 t + \frac{\pi}{2}) \\ (\rho_2 - 1) \sin(-\omega_2 t + \frac{\pi}{2}) \end{bmatrix} \\ &= \begin{bmatrix} -(\rho_2 - 1) \sin(-\omega_2 t) \\ (\rho_2 - 1) \cos(-\omega_2 t) \end{bmatrix} \end{aligned} \quad (38)$$

The equations for $\mathbf{v}_i(t)$ and $\mathbf{a}_i(t)$ are easily obtained by taking the time derivatives with respect to $\mathbf{p}_i(t)$, $i = 1, 2$. Note

TABLE I. AVERAGE MEAN ABSOLUTE ERROR FOR \sum_A AND \sum_B OVER 1000 RUNS WITH DIFFERENT NOISE STANDARD DEVIATION ON THE RANGE MEASUREMENT

	Range noise σ_R [m]							
	0	0.1	0.25	0.5	1	2	4	8
\sum_A AMAE [cm]	2.3	3.4	6.2	10.8	19.3	37.7	72.9	118.2
\sum_B AMAE [cm]	2.7	4.5	8.5	15.1	27.1	52.5	101.8	172.8

that this is not generally true, since \mathcal{H}_i is a rotating frame of reference, but in this case this is possible because the drones keep a constant heading equal to 0 rad.

By picking for ρ_2 and ω_2 the values 4 and $\frac{2\pi}{20}$, the trajectory of drone 2 becomes a circle with a radius of 4 m that is traversed in 20 s. To comply with the earlier defined constraints, ρ_1 and ω_1 become 3 m and $-\frac{2\pi}{20}$ rad/s respectively. These values are chosen to be representative of what a real drone should easily be capable of and result in relative velocities of around 1 m/s in x and y directions between the two drones.

The study will test the performance of the relative localization filter as seen from the perspective of drone 1, who is thus tracking drone 2. The filter is fed perfect information on all state and input values, except for the value of the range $\|\mathbf{p}\|_2$ between the two drones. The range measurement are artificially distorted with increasingly heavy Gaussian white noise. The measured range fed to the filter is thus $\|\mathbf{p}\|_{2,m} = \|\mathbf{p}\|_2 + n(\sigma_R)$, where $n(\sigma_R)$ is a Gaussian white noise signal with zero mean and standard deviation σ_R . The standard deviations that are tested are 0 (noise free), 0.1, 0.25, 0.5, 1, 2, 4, and 8 m. Of course a standard deviation of 8 m is quite high, but this is intentionally chosen with the intent to observe a significant difference in the error. Since this study keeps all the other measurements and inputs noise free, the noise on the range measurement needs to be quite high to get a significant increase in the localization error.

This time the EKF runs at 20 Hz, which is more representative of what the filter will be run at during later experiments discussed in section IV. The described flight trajectory is simulated for 20 seconds each run (which is thus one complete revolution of the circular trajectory). The EKF is initialized to the true state to omit the effects of initialization.

For one particular noise standard deviation, both the filter for \sum_A and for \sum_B are simulated for 1000 different noise realizations. For each realization the MAE of the estimated \mathbf{p} with respect to its true value is computed, again by considering the combined error in the estimate of $\|\mathbf{p}\|_2$. After 1000 realizations, the Average MAE (AMAE) is computed to mitigate the possibility of the results being corrupted by randomness in the noise realizations.

The resulting AMAE values for systems \sum_A and \sum_B are given in table I and are plotted in figure 13. As expected, at very low noise values on the range measurement, both the filters for \sum_A and \sum_B have very similar error performance. With no noise on the range measurements, the difference between the two filters is only 4 mm. However, since the filter for \sum_B is more sensitive to noise on the range measurements, it quickly starts to perform worse than \sum_A as the noise on the range measurement is increased.

This result is in line with the analytical results presented

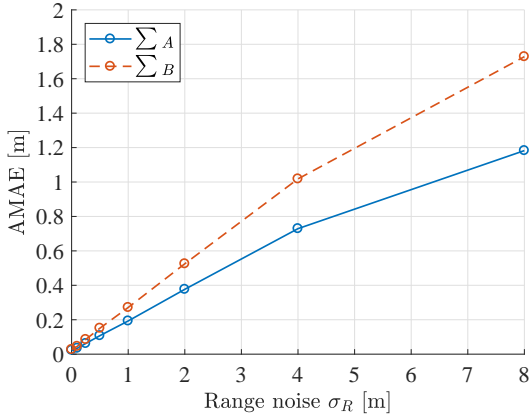


Fig. 13. AMAE in estimate of $\|\mathbf{p}\|_2$ for \sum_B and \sum_A

in section II. However, it also raises the question of whether removing the dependency on a common heading reference poses any advantage, since \sum_A performs consistently better than \sum_B . The reason for this result, however, lies in the fact that the studied scenario uses perfect measurements for all the sensors except for the measured range. As mentioned in the introduction, the heading observation is notoriously troublesome and unreliable, especially in an indoor environment [32]. Therefore, it would be valuable to study what would happen to this analysis in the case where the heading estimate is not perfect, as will be studied next.

D. Kinematic, noisy range measurements, and heading disturbance study for observable situation

In order to compare the results obtained with an imperfect heading measurement to those obtained in the previous section, the same drone trajectories are simulated. The trajectories of drone 1 and 2 can thus be represented by equations 38 and 37 respectively. All the other simulation parameters are kept the same as well.

This time, however, a disturbance is introduced on the heading measurement. The simulated disturbance is modeled to look similar to how an actual local perturbation in the magnetic field would perturb a heading estimate. The actual magnetic perturbation and the corresponding heading error are taken from a study on indoor magnetic perturbations [32]. In that study, the obtained disturbance on the heading estimate looks similar to a Gaussian curve, and in this analysis it is thus modelled as such.

The actual disturbance on the heading estimate in time $d(t)$ is given by:

$$d(t) = A_d \cdot e^{-(\epsilon(t-t_0))^2} \quad (39)$$

Here the amplitude of the disturbance in radians is given by A_d , the parameter ϵ controls the width of the Gaussian curve and t_0 controls the location of the curve in time. For this study, ϵ is set to 1, resulting in a disturbance of approximately 4 seconds long, and t_0 is set to 5, such that the disturbance occurs

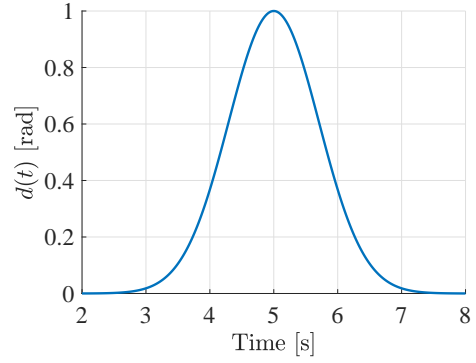


Fig. 14. Disturbance on the relative heading measurement in time, for an amplitude A_d of 1 rad

at around 5 seconds into the flight. How such a disturbance looks is presented in figure 14 for an amplitude A_d of 1 rad.

Several amplitudes of the disturbance are tested, namely 0, 0.25, 0.5, 1, and 1.5 rad. The final amplitude of 1.5 thus results in a maximum heading estimate error of almost 85° , which is approximately equal to the amplitude of the disturbance shown in [32]. Note that the disturbance is introduced directly on the measurement of $\Delta\psi$ (the difference in headings between two drones). This is the situation that would occur if one of the two drones would fly in a locally perturbed area.

Since in the end the parameter of interest is how the filter for \sum_B compares to the filter for \sum_A , the data is this time represented as a percentage comparison of the relative localization errors between the two filters. This data is visually presented in figure 15. A positive % in this figure means that the filter for \sum_B performs *worse* than the filter for \sum_A . The dotted line at a 0% represents the point where both filters perform equally well.

In this comparison we now see that as the applied disturbance amplitude on the heading measurement provided to system \sum_A is increased, the region for which \sum_B performs better than \sum_A expands. In the case of the largest disturbance, with A_d equal to 1.5 radians, filter \sum_B even performs better at a range noise σ_R equal to 8.

This result reinforces the presumption that it is not always better to include a heading measurement in the filter. In the experimental results in section IV we will use Ultra Wideband (UWB) radio modules to obtain range measurements between drones. To give an idea of what type of range noise standard deviations can actually be achieved in practice, in the executed experiments with real drones, the UWB modules resulted in ranging errors with standard deviations between 0.1 and 0.3. If we assume normality of the ranging error, this would mean for the situation depicted in figure 15 that the heading-independent system \sum_B would be the preferred choice for all heading disturbance amplitudes except for the situation where there is no heading disturbance at all.

IV. LEADER-FOLLOWER FLIGHT EXPERIMENT

In this section we demonstrate the workings of the heading-independent filter in practice in an indoor environment for a

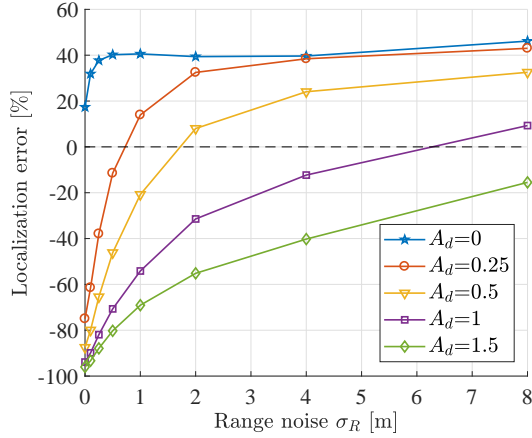


Fig. 15. Percentage error comparison between \sum_B and \sum_A for different disturbance amplitudes A_d . Positive percentage means \sum_B performs worse than \sum_A .

scenario of leader follower flight.

A. Leader-follower flight considerations

Before designing an actual control method to accomplish leader-follower flight, let's first reflect on the previous observability analysis results from section II and their implications with respect to leader-follower flight.

We know that in order to have an observable heading independent system, the combined motion of the leader and follower has to meet the observability condition presented in equation 33. We further know that in order to meet this condition, the three intuitive conditions presented by equation 34 to 36 certainly have to be met. Let's first consider these conditions.

The first condition in equation 34 specifies that the relative position between leader and follower must be non-zero. This condition has little implication to leader-follower flight, other than the fact that the follower must follow the leader at a non-zero horizontal distance, which typically is the objective.

The second conditions in equation 35 tells us that both drones must be moving. As far as leader-follower flight is concerned, this is automatically accomplished as long as the leader is not stationary.

The third condition in equation 36 is especially impactful for leader-follower flight. It specifies that the drones should not be moving in parallel (regardless of speed), unless they are also accelerating. A lot of research on leader-follower flight aims to design control laws that would result in fixed geometrical formations between different agents in the formation. This is typically achieved by specifying desired formation shapes, or desired inter-agent distances for members in the swarm [14, 18, 19, 41]. By the very nature of fixed geometries, that would result in parallel velocity vectors.

For this reason, a different approach to leader-follower flight is certainly necessary. Rather than flying in a fixed formation, it is also possible for the follower to fly a delayed version of the leader's trajectory. As long as the leader's trajectory is not

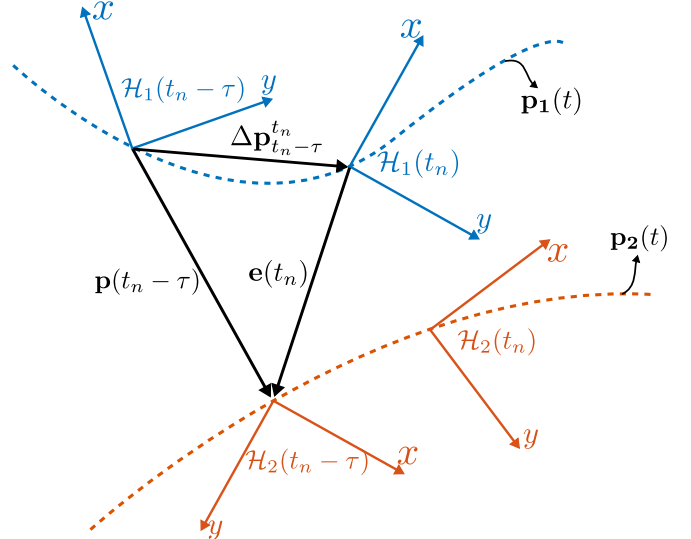


Fig. 16. Control problem for leader-follower flight. In blue is drone 1's trajectory in time $p_1(t)$. In orange is drone 2's trajectory in time $p_2(t)$. The desire is for drone 1 to drive $e(t)$ to $\mathbf{0}$ for $t \rightarrow \infty$.

a pure straight line for long periods of time, this will result in relative motion between the leader and follower. This is therefore the approach taken in this paper.

This solution should also help to prevent the MAVs from getting stuck in an unobservable situation that is not covered by equations 34 to 36, but that is covered by the full observability condition in equation 33. We concluded that for the scenarios that are numerically found to be unobservable according to equation 33, changing the relative position \mathbf{p} only slightly can already result in an observable situation. In the proposed method of having the follower fly a time-delayed version of the leader's trajectory, the relative position vector \mathbf{p} will naturally change if the leader's trajectory is not a straight line.

Whether this is sufficient measure to retain observability of the system, will be evaluated after the leader-follower flight results are presented. This will be done in section V.

B. Leader-follower formation control design

We thus want to construct a leader-follower control method that results in the follower flying a delayed version of the leader's trajectory. This naturally avoids parallel velocity vectors and keeps the relative positions dynamic. As it turns out, this type of control can be quite intuitively accomplished with the information provided by the relative localization filter.

Consider the schematically depicted problem in figure 16. It shows two arbitrary trajectories in dotted lines. At the top, in blue, is the trajectory for drone 1, which is represented by its position vector in time $p_1(t)$. On the bottom, in orange, is the trajectory for drone 2, $p_2(t)$.

Suppose the desire is for the follower (say drone 1) to follow the leader's trajectory (say drone 2) with a time delay equal to τ . The control problem for drone 1 can be simply put as the desire to accomplish $p_1(t) = p_2(t - \tau)$.

Let t_n indicate the current time at which a control input must be calculated. At the current time, drone 1 has a body fixed reference frame $\mathcal{H}_1(t_n)$, whose origin is $\mathbf{p}_1(t_n)$. At time $t_n - \tau$, drone 1 knows the relative position of the leader in its own body fixed frame $\mathcal{H}_1(t_n - \tau)$, since this information is provided by the relative localization filter. However, for this control method to work, drone 1 must have knowledge of where the leader's old position is at the current time t_n . This value of interest is depicted by the vector $\mathbf{e}(t_n)$ in figure 16; it is the positional error with respect to the desired follower's position at time t_n .

Denote by $\mathbf{R}_{\mathcal{H}_i(t_1)\mathcal{H}_i(t_2)}$ the rotation matrix from frame \mathcal{H}_i at time t_2 , to frame \mathcal{H}_i at time t_1 . This rotation matrix is defined as:

$$\mathbf{R}_{\mathcal{H}_i(t_1)\mathcal{H}_i(t_2)} = \begin{bmatrix} \cos(\Delta\psi_i|_{t_1}^{t_2}) & -\sin(\Delta\psi_i|_{t_1}^{t_2}) \\ \sin(\Delta\psi_i|_{t_1}^{t_2}) & \cos(\Delta\psi_i|_{t_1}^{t_2}) \end{bmatrix}, \quad (40)$$

$\Delta\psi_i|_{t_1}^{t_2}$ is the change in heading angle for drone i from time t_1 to time t_2 , which can be calculated as:

$$\Delta\psi_i|_{t_1}^{t_2} = \int_{t_1}^{t_2} r_i(t) dt \quad (41)$$

The current positional error for the follower drone 1, depicted in figure 16, can be defined as:

$$\mathbf{e}(t_n) = \mathbf{R}_{\mathcal{H}_1(t_n)\mathcal{H}_1(t_n - \tau)} (\mathbf{p}(t_n - \tau) - \Delta\mathbf{p}_{t_n - \tau}^{t_n}) \quad (42)$$

The vector $\Delta\mathbf{p}_{t_n - \tau}^{t_n}$ represents how much the follower has moved from time $t_n - \tau$ until t_n as defined in frame $\mathcal{H}_1(t_n - \tau)$. This vector can be calculated using information available to the follower:

$$\Delta\mathbf{p}_{t_n - \tau}^{t_n} = \int_{t_n - \tau}^{t_n} \mathbf{R}_{\mathcal{H}_1(t_n - \tau)\mathcal{H}_1(t)} \mathbf{v}_1(t) dt \quad (43)$$

Finally, one more piece of information is needed in order to be able to design a control law for the follower drone, which is the model of the follower drone and how it responds to control inputs. In this paper, it is assumed that the drone already has stable inner loop control running on board, such that the drone becomes an outer loop control system that directly can take velocity commands. It is further assumed that with the inner loops in place, the drone responds like a very simple first order delay filter to velocity commands, such that the differential equation for the drone's velocity becomes:

$$\dot{\mathbf{v}}_1 = \tau^{-1}(\mathbf{v}_{1c} - \mathbf{v}_1) \quad (44)$$

Where τ^{-1} is a diagonal matrix with on the diagonal the inverse values of the time constants that characterise the delay of the system with respect to a control input \mathbf{v}_{1c} . This is only an approximation of how the actual drone behaves, but it will be shown to be sufficient to accomplish the desired behavior.

With all this information in place, a control law can be designed. The control law is designed using Nonlinear Dynamic

Inversion (NDI) principles. In order to use NDI, a state space model is required for the situation at hand. A very similar state space model to the one used for the relative localization filter can be used. Define the state vector as:

$$\bar{\mathbf{x}} = [\mathbf{e}^\top, \Delta\bar{\psi}, \mathbf{v}_1^\top, \bar{\mathbf{v}}_2^\top]^\top \quad (45)$$

The state vector is similar to the one defined before for the relative localization filter, with a few small changes. First of all, $\mathbf{e} = \mathbf{e}(t)$ represents the current positional error for the follower drone 1 with respect to the leader's old position. Secondly, $\Delta\bar{\psi}$ and $\bar{\mathbf{v}}_2^\top$ represent again the difference in heading between two drones and the velocity of drone 2, except now $\Delta\bar{\psi}$ is the difference in heading between frame $\mathcal{H}_1(t)$ and $\mathcal{H}_2(t - \tau)$, and $\bar{\mathbf{v}}_2^\top$ is the delayed leader's velocity at time $t - \tau$, such that $\bar{\mathbf{v}}_2^\top = \mathbf{v}_2(t - \tau)$.

Similarly, define a new input vector as:

$$\bar{\mathbf{u}} = [\mathbf{v}_{1c}^\top, \bar{\mathbf{a}}_2^\top, r_1, \bar{r}_2]^\top \quad (46)$$

Where \mathbf{v}_{1c} is the actual control input fed to drone 1, and $\bar{\mathbf{a}}_2$ and \bar{r}_2 represent the same values as \mathbf{a}_2 and r_2 , except delayed versions thereof. Therefore $\bar{\mathbf{a}}_2 = \mathbf{a}_2(t - \tau)$ and $\bar{r}_2 = r_2(t - \tau)$.

Finally, a new set of state differential equations can be defined as:

$$\dot{\bar{\mathbf{x}}} = \bar{\mathbf{f}}(\bar{\mathbf{x}}, \bar{\mathbf{u}}) = \begin{bmatrix} -\mathbf{v}_1 + \bar{\mathbf{R}}\bar{\mathbf{v}}_2 - \mathbf{S}_1\mathbf{e} \\ \bar{r}_2 - r_1 \\ \tau^{-1}(\mathbf{v}_{1c} - \mathbf{v}_1) \\ \bar{\mathbf{a}}_2 - \bar{\mathbf{S}}_2\bar{\mathbf{v}}_2 \end{bmatrix} \quad (47)$$

Where $\bar{\mathbf{R}} = \mathbf{R}(\Delta\bar{\psi})$ and $\bar{\mathbf{S}}_2 = \mathbf{S}_2(\bar{r}_2)$.

The state that we wish to control is the current positional error that drone 1 has with respect to the delayed leader's position, so the state \mathbf{e} . This state can be represented as:

$$\mathbf{e} = \mathbf{H}\bar{\mathbf{x}} \quad (48)$$

With \mathbf{H} given by:

$$\mathbf{H} = [\mathbf{I}_{2 \times 2} \quad \mathbf{0}_{2 \times 5}] \quad (49)$$

The derivative of the control variable with respect to time is equal to:

$$\dot{\mathbf{e}} = \mathcal{L}_{\bar{\mathbf{f}}}^1 \mathbf{e} = \mathbf{H}\bar{\mathbf{f}} = -\mathbf{v}_1 + \bar{\mathbf{R}}\bar{\mathbf{v}}_2 - \mathbf{S}_1\mathbf{e} \quad (50)$$

The second derivative of the control variable:

$$\begin{aligned} \ddot{\mathbf{e}} &= \mathcal{L}_{\bar{\mathbf{f}}}^2 \mathbf{e} = (\nabla \otimes \dot{\mathbf{e}}) \cdot \bar{\mathbf{f}} \\ &= \left[-\mathbf{S}_1 \quad \frac{\partial \bar{\mathbf{R}}}{\partial \Delta\bar{\psi}} \bar{\mathbf{v}}_2 \quad -\mathbf{I}_{2 \times 2} \quad \bar{\mathbf{R}} \right] \cdot \bar{\mathbf{f}} \\ &= -\mathbf{S}_1 (-\mathbf{v}_1 + \bar{\mathbf{R}}\bar{\mathbf{v}}_2 - \mathbf{S}_1\mathbf{e}) + \frac{\partial \bar{\mathbf{R}}}{\partial \Delta\bar{\psi}} \bar{\mathbf{v}}_2 (\bar{r}_2 - r_1) \\ &\quad - \mathbf{I}_{2 \times 2} (\tau^{-1}(\mathbf{v}_{1c} - \mathbf{v}_1)) + \bar{\mathbf{R}} (\bar{\mathbf{a}}_2 - \bar{\mathbf{S}}_2\bar{\mathbf{v}}_2) \\ &= \mathbf{D}\mathbf{v}_{1c} + \mathbf{b}(\mathbf{x}, \mathbf{u}) \end{aligned} \quad (51)$$

With \mathbf{D} equal to:

$$\mathbf{D} = -\mathbf{I}_{2 \times 2} \tau^{-1} \quad (52)$$

and $\mathbf{b}(\mathbf{x}, \mathbf{u})$ equal to:

$$\begin{aligned}\mathbf{b}(\mathbf{x}, \mathbf{u}) = & -\mathbf{S}_1 (-\mathbf{v}_1 + \bar{\mathbf{R}}\bar{\mathbf{v}}_2 - \mathbf{S}_1\mathbf{p}) \\ & + \frac{\partial \bar{\mathbf{R}}}{\partial \Delta\psi} \bar{\mathbf{v}}_2 (\bar{r}_2 - r_1) \\ & + \mathbf{I}_{2 \times 2} \tau^{-1} \mathbf{v}_1 + \bar{\mathbf{R}} (\bar{\mathbf{a}}_2 - \mathbf{S}_2 \mathbf{v}_2)\end{aligned}\quad (53)$$

This can further be reduced to:

$$\begin{aligned}\mathbf{b}(\mathbf{x}, \mathbf{u}) = & -\mathbf{S}_1 (-\mathbf{v}_1 + \bar{\mathbf{R}}\bar{\mathbf{v}}_2 - \mathbf{S}_1\mathbf{p}) \\ & - \frac{\partial \bar{\mathbf{R}}}{\partial \Delta\psi} \bar{\mathbf{v}}_2 r_1 + \mathbf{I}_{2 \times 2} \tau^{-1} \mathbf{v}_1 + \bar{\mathbf{R}} \bar{\mathbf{a}}_2\end{aligned}\quad (54)$$

At this point the following control law can be chosen:

$$\mathbf{v}_{1c} = \mathbf{D}^{-1}(\mathbf{i} - \mathbf{b}(\mathbf{x}, \mathbf{u}))\quad (55)$$

with \mathbf{i} now a virtual control input.

This control law results in a fully linearized differential equation for the positional error of the follower, since substitution of the control law from equation 55 in equation 51 results in the following differential equation:

$$\ddot{\mathbf{e}} = \mathbf{i}\quad (56)$$

Which can be shown to be exponentially stable if the following virtual control is implemented:

$$\mathbf{i} = -K_p \mathbf{e} - K_d \dot{\mathbf{e}}\quad (57)$$

$$K_p, K_d > 0\quad (58)$$

C. Experimental Set-Up

One of the main findings in the observability study and the simulation results is that the localization error scales more steeply with range noise for system \sum_B than for \sum_A . It is therefore important to use sensors that can provide accurate ranging for these experiments.

Whilst a variety of wireless transceivers are capable of providing the communication and ranging required for the relative localization filter, specifically Ultra Wideband (UWB) based radio transceivers have been used in this paper. UWB has recently gained attention within the domain of ranging and localization, and is deemed to also provide a good solution within this context due to its favorable properties in this scenario. UWB signals are characterized by their fine temporal and spatial resolution [42], which leads UWB based systems to be able to resolve for example multipath more easily [43]. Ultimately, this leads to accurate ranging performance for these systems. Another advantage of the technology is its relative robustness to interference from other radio technologies [24, 44, 45] due to the fact that it operates on an (ultra) wide range of frequencies.

The UWB ranging hardware that has been used in these experiments is the ScenSor DWM1000 module that is sold by Decawave.¹ The algorithms used to control the module must be run on a separate micro controller that communicates with

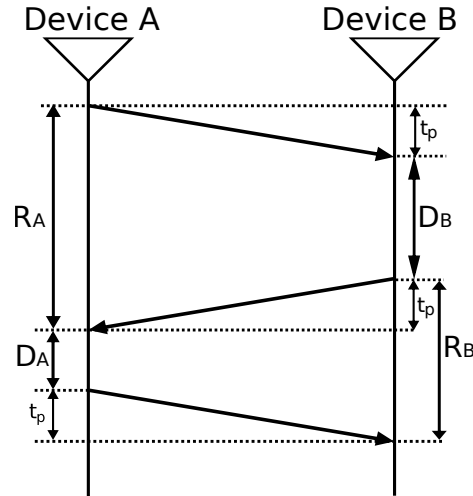


Fig. 17. Double Sided Two Way Ranging message exchange. Adapted from [46]

the UWB module. The performance of the modules therefore also depends on the performance of the algorithms that are run on the micro controller.

The specific ranging algorithm that is employed in this paper is a particular implementation of the Two-Way Ranging (TWR) method introduced in [46]. The messages exchanged in this protocol are presented schematically in figure 17.

The variable of interest is t_p , which represents the propagation time of the UWB signal. This can be converted in an actual range by multiplying it with the speed of light. It is shown in [46] that this t_p can be extracted through:

$$t_p = \frac{R_A R_B - D_A D_B}{2T}\quad (59)$$

where $T = R_A + D_A = R_B + D_B$, and R_A , R_B , D_A , and D_B are the round trip times (R) and message delay times (D) of the TWR exchange as perceived by the clocks in device A and B.

In the message exchange in figure 17 only device B would have all the necessary information to compute its range with respect to device A. If the desire is for both devices to be able to localize each other, an additional message must be added at the end of the protocol (from device B to device A) which contains the computed range.

Since the end goal is to fuse ranging data with velocity, acceleration, height, and yaw rate data in the localization filter, these variables must also be communicated between the two devices. The same UWB messages used in the TWR protocol are also used to communicate these variables.

The UWB module transceiver has been installed on the Parrot Bebop 2 platform.² The Bebop 2 runs custom autopilot software designed using the open-source autopilot framework Paparazzi UAV.³ Paparazzi UAV provides the stable inner loop

¹<https://www.decawave.com/products/dwm1000-module>

²<https://www.parrot.com/us/drones/parrot-bebop-2#parrot-bebop-2>

³http://wiki.paparazziuav.org/wiki/Main_Page

control loops for the Bebop 2 using Incremental NDI (INDI). This allows us to control the outer loop by giving the computed velocity commands to the INDI inner loops.

The velocity and height information that are also necessary for the relative localization filter, is at first provided by an overhead Motion Capture System (MCS) by OptiTrack.⁴ In a second iteration of the experiment this information is provided through only on-board sensing. The velocity data is then obtained from the drones' on-board bottom-facing camera. Using Lucas-Kanade based optical flow methods, the camera can be used to obtain estimates of the drones' velocities. The height is measured using an on-board ultrasonic sensor that the Bebop 2 is equipped with by default. The acceleration and yaw rate information is at all times obtained from the drones' on-board accelerometers and gyroscope respectively.

The experiment is first conducted with one leader and one follower drone in section IV-D. The experiment is then performed again for the case where there are two followers in section IV-E.

D. Leader-follower flight with one follower

The experiment with one follower drone consists of one Bebop 2 following another Bebop 2 using the control law presented in section IV-B. Both Bebop 2's first, after take-off, fly concentric circles just like the one used in the simulation section, as shown in figure 12. This procedure is followed to make sure the EKF that runs on-board the drones has time to converge to the correct result, such that by the time the follower drone is instructed to start following the leader, the follower has a correct estimate of the relative location of the leader.

The trajectory of the leader has been designed to sufficiently excite the the relative localization filter during the leader-follower flight and to decrease the likelihood of being stuck in unobservable states. This has been done by introducing frequent turns in the trajectory to have changing relative velocities and accelerations. The follower is instructed to follow the leader's trajectory with a time delay of $\tau = 5$ seconds.

It is important to note that the norm of the follower's commanded velocity $\|\mathbf{v}_{1c}\|_2$ during both experiments is saturated at 1.5 m/s. This measure is taken for reasons of safety, since the drones are flying in a confined area. This does however have consequences for the performance of the follower's tracking, as will be discussed in the next sections.

1) Leader-follower flight with velocity and height information from a MCS

First the case where velocity and height information is provided by the MCS is studied. In figure 18 the trajectory flown by the follower is compared to the trajectory of the leader. The x and y coordinates are compared separately for part of the flight in figures 19a and 19b. Finally, in figure 20, a time composition of overhead camera images is given for 5 seconds of flight as an illustration. The follower's position is shown at seven time instances during these 5 seconds and is compared to the leader's trajectory.

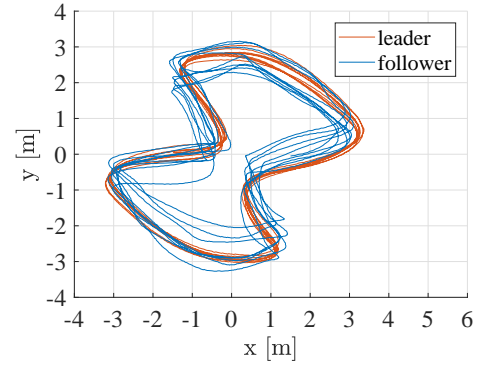


Fig. 18. The trajectories of leader and follower during experiment with MCS height and velocity

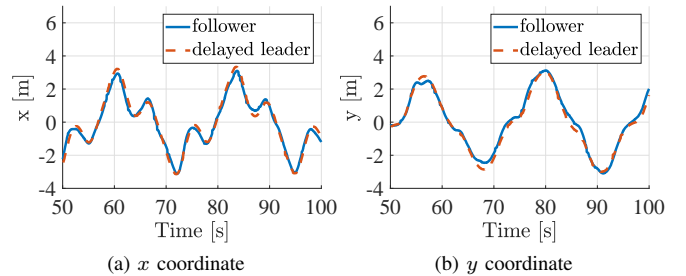


Fig. 19. The trajectory of the follower compared to the delayed trajectory of the leader for the experiment with MCS height and velocity.

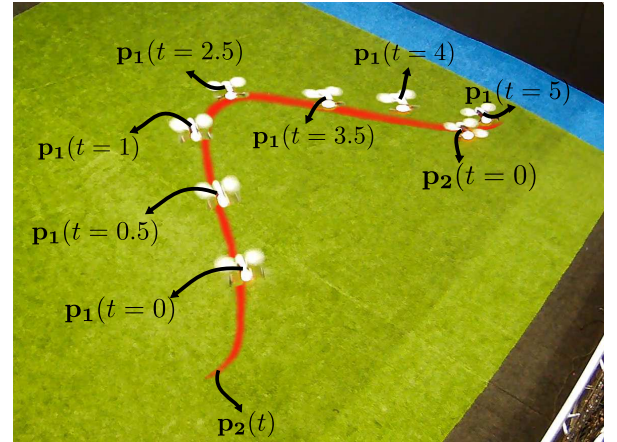


Fig. 20. Time composition of overhead camera images of leader and follower drone in time, for the experiment with MCS height and velocity. Indicated in orange and marked by $p_2(t)$, is part of the leader's trajectory. The leader's final position is indicated by $p_2(t = 0)$. Seven points in time of the follower's trajectory are indicated in the image. According to the control objective, $p_1(t = 5)$ should equal $p_2(t = 0)$.

A total of 200 seconds of leader follower flight took place successfully and will be analyzed here. During this time, many laps of the designed trajectory were executed. The trajectories in figures 18 to 20 indeed show that the follower is tracking a delayed version of the leader's trajectory. There

⁴<http://optitrack.com/>

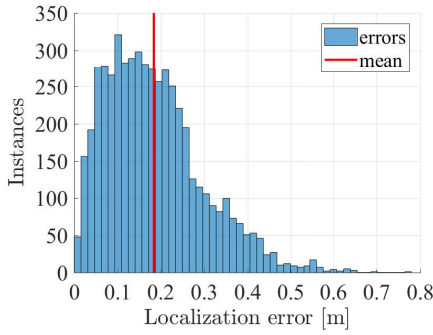


Fig. 21. Histogram of the localization error for the follower during experiment with MCS height and velocity

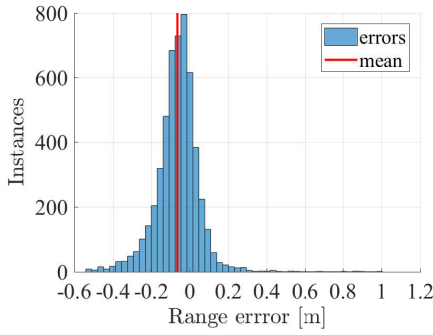


Fig. 22. Histogram of the ranging error during experiment with MCS height and velocity

are however clearly noticeable errors as well. Before looking into the specifics of the tracking error, let's first examine the performance of the relative localization filter throughout this experiment.

The actual error distribution for the norm of the relative location estimate $\|\mathbf{p}\|_2$ is shown in figure 21. The errors have a mean value of 18.4 cm and a maximum value of 77.5 cm, at maximum inter-drone distances up to 5 m.

Since in this experiment the velocity and height information was provided with high accuracy by the MCS, one would expect the primary source for the localization error to be the ranging error from the UWB modules. However, inspection of the ranging error actually shows a pretty favourable error distribution.

A histogram of the ranging error throughout the flight is given in figure 22. The mean of the ranging error is close to zero (about -6.4 cm) and the errors are nicely distributed around this mean. This is therefore not the main cause of the occasionally higher relative localization errors.

In fact, the most clearly identifiable cause for the relative localization error is the occasional dropping of frames by the UWB modules. The average update rate of the relative localization filter is about 25 Hz, corresponding to a time step of approximately 40 ms. The update rate is established by the rate at which the UWB modules produce a new ranging result. However, the modules occasionally drop frames, causing the

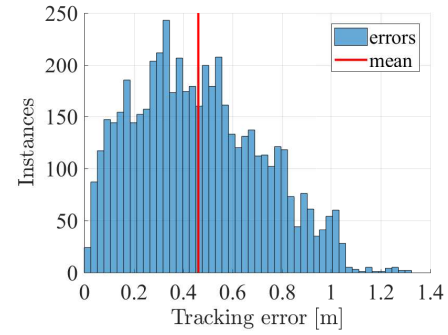


Fig. 23. Histogram of the tracking error $\|\mathbf{e}\|_2$ for the follower during experiment with MCS height and velocity

time step to spike up. The largest time step recorded during the flight is 470 ms, an order of magnitude larger than the average. It is not hard to imagine the unfavorable effect this can have for the relative localization estimate. It is therefore not coincidental that the largest localization error recorded during the flight, also corresponds to one of those times where the UWB modules dropped frames.

Knowing what the relative localization performance was during the flight, we can better inspect the tracking error of the follower drone. The tracking error distribution $\|\mathbf{e}\|_2$ is given in figure 23. The mean of the distribution is equal to 46.1 cm and the maximum error is 1.32 m.

Of course part of this error is caused by a relative localization error from the follower's perspective, which will inevitably affect the tracking performance. However, since the relative localization error is quite a bit lower than the tracking error, there must be other sources of error as well.

One source of the error is the fact that the follower's response to a velocity command \mathbf{v}_{1c} is modeled as a first order delay. In reality the drone inevitably has some overshoot with respect to commands, which is not captured by a first order delay. This model mismatch by itself might not be that harmful to the performance, since the control law would respond to the modeling mismatch with more aggressive velocity commands as a reaction to the drone not behaving as modeled. However, the control law's freedom is severely restricted by the command saturation at 1.5 m/s.

Another effect of the command saturation is that the follower cannot move as fast as the command law would want it to move. This is supported by a qualitative analysis of the follower's trajectory with respect to the leader's trajectory in figure 18. Most of the trajectories of the follower seem to take a 'shortcut' with respect to the leader's trajectory. This falls in line with the expected behavior due to the command saturation. The control law is designed not only to track the trajectory of the leader in space, but also in time. As the follower starts lagging behind the leader more than the desired $\tau = 5$ seconds, the follower starts to take shortcuts in the trajectory to catch up with the leader. This observation would likely be less prevalent if the command saturation

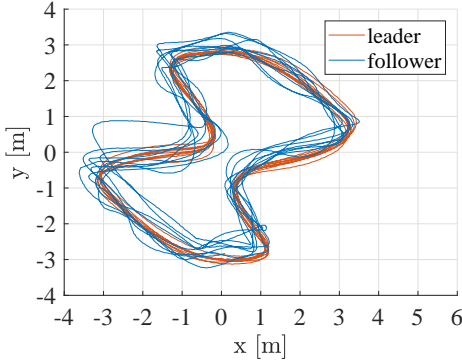


Fig. 24. Trajectory of leader and follower during experiment with only on-board sensing and processing

would be increased to higher values.

2) Leader-follower flight with only on-board measurements

As a second step, we demonstrate the workings of the proposed methods in this paper when *only on-board sensing* is used. The follower drone now does not use any MCS information during its flight. The velocity information now comes from Lucas-Kanade based optical flow measurements and the height is now derived from the on-board ultrasonic sensor. Similarly, the leader drone directly communicates optical flow velocities and ultrasonic height measurements (along with accelerations and yaw rate from the IMU) to the follower drone for use in the relative localization filter. The MCS is only used for the purpose of logging ground truth data and for the leader to safely fly its original trajectory. No MCS data is used directly in flight by the follower. Again, 200 s of leader-follower flight with full on-board sensing took place successfully and will be analyzed here.

The trajectory of the follower with respect to the delayed leader's trajectory is compared in figures 24 and 25. Furthermore, another time composition for 5 seconds of flight where the follower is tracking the leader is given in figure 26.

The main qualitative difference with respect to the situation where the MCS was still used for velocity and height information, is the fact that the follower's trajectory is a bit less smooth. Otherwise, the performance seems relatively similar. Overall, the follower taking a 'shortcut' with respect to the leader's trajectory still appears to happen, although the increased disorder in the follower's trajectory makes it somewhat less apparent.

The tracking error distribution for the on-board sensing case is given in figure 28. The mean tracking error is 50.8 cm and the maximum error is 1.47 m. The relative localization error is given in figure 27. Here, the mean error is 22.6 cm and the maximum error is 75.8 cm, at maximum drone distances up to 5.2 meters.

It's interesting to see how similar the performance is when using only on-board sensing, compared to using the MCS for height and velocity data. This can mainly be attributed to the fact that the measurements that have been replaced

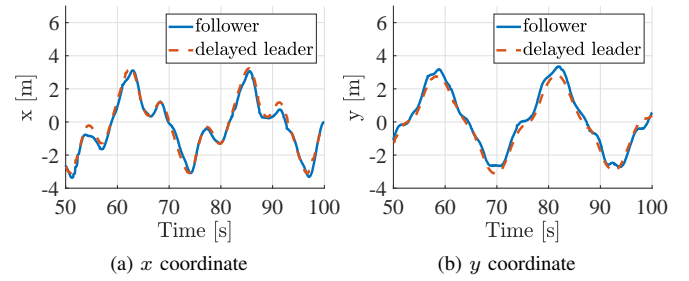


Fig. 25. The trajectory of the follower compared to the delayed trajectory of the leader for the experiment with only on-board sensing.

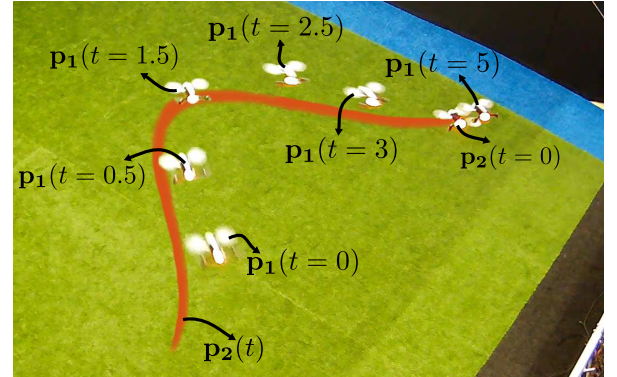


Fig. 26. Time composition of overhead camera images of leader and follower drone in time, for the experiment with only on-board sensing. Indicated in orange and marked by $p_2(t)$, is part of the leader's trajectory. The leader's final position is indicated by $p_2(t = 0)$. Six points in time of the follower's trajectory are indicated in the image. According to the control objective, $p_1(t = 5)$ should equal $p_2(t = 0)$.

(the height and velocity of both drones) are actually quite accurately measured on-board as well.

The primary reason for why the trajectory of the follower with on-board sensors still seems slightly more disordered, is actually caused by the fact that the follower has difficulty to accurately control its altitude when using only on-board sensing. The follower now purely relies on height measurements from its ultrasonic sensor. The update rate of this sensor is low, and in between measurements the follower uses (noisy) accelerometer data to update its height. This sometimes causes the follower to believe its altitude is different than it really is, causing it to rapidly ascent or descent. This can take up a lot of thrust, restricting the follower's ability to manoeuvre accurately in the horizontal plane, due to thrust saturation.

E. Leader-follower flight with two followers

To demonstrate that the methods in this paper can also scale to more than one follower drones, the leader-follower flight is also performed with two followers instead of one, both with MCS height and velocity data, and again with only on-board sensing as well.

The UWB messaging protocol is adapted to allow every drone to perform ranging with every other drone. The drones

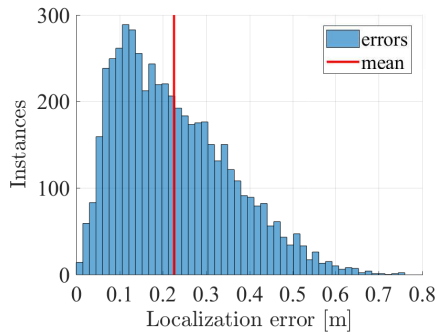


Fig. 27. Histogram of the localization error for the follower during experiment with only on-board sensing and processing

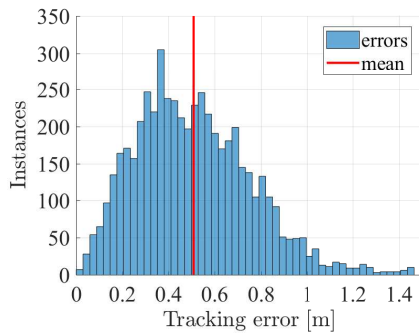


Fig. 28. Histogram of the tracking error $\|e\|_2$ for the follower during experiment with only on-board sensing and processing

also communicate a unique (pre-assigned) identification number within the UWB messages. The followers can use this identification number to determine which messages originate from the leader and can therefore individually keep track of the leader just like before. The main consequence of the increased messages is a drop in the UWB range update rate, which is reduced from about 25 Hz with 2 drones, to about 16 Hz with 3 drones.

This time, due to the lack of space available, there is no initialization procedure to give the kalman filters on the followers time to converge. Instead, the drones are placed in starting positions and orientations that match roughly with what the kalman filters on-board the drones are initialized to. Whilst this placement is done purely by eye, it proved to be sufficient measure to be able to safely start the leader-follower flight even without an initialization phase.

The leader flies the same trajectory as before. The first follower follows this trajectory with a $\tau = 4$ second delay, and the second follower follows it with an $\tau = 8$ second delay. Again 200 seconds of successful flight data is extracted and analysed.

An overhead camera image for the flight with MCS height and velocity data is presented in figure 29 to give an idea of how the experiment really looked like. The trajectories for this flight are displayed in figure 30 for the leader and two

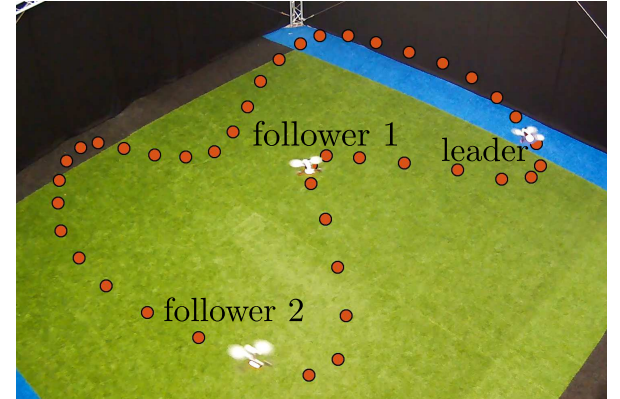


Fig. 29. Overhead camera image of leader and two followers using MCS height and velocity. In orange is the leader's trajectory marked at 0.5 second intervals.

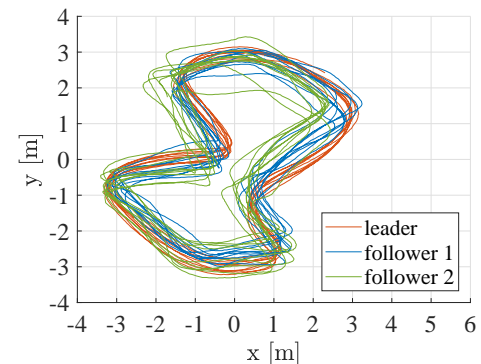


Fig. 30. Trajectory of leader and two followers using MCS height and velocity

followers. For the flights with only on-board information, the trajectories are given in figure 31.

Much of the same behaviour as for the case with just one follower is observed again. We again see that the followers tend to take a shortcut with respect to the leader's trajectory. Furthermore, it can be seen that the flights using only on-board information are less smooth than those with MCS height and velocity information.

For the flight with MCS data, follower 1 has a MAE for the relative localization error of only 15.8 cm. By comparison, follower 2 has a MAE of 43.9 cm. Furthermore, followers 1 and 2 have MAE for the tracking of 42.9 cm and 70.3 cm respectively.

The flight with only on-board sensing resulted in a relative localization MAE of 51.8 and 53.6 cm. The tracking MAE this time was 58.6 and 98.4 cm. The reasons for why these values are worse than for the flights with one follower will be evaluated in the next subsection, in comparison with all the other flights.

F. Comparison of flights

In this section we present in a clear format the relative localization and tracking MAE of the various flights that were

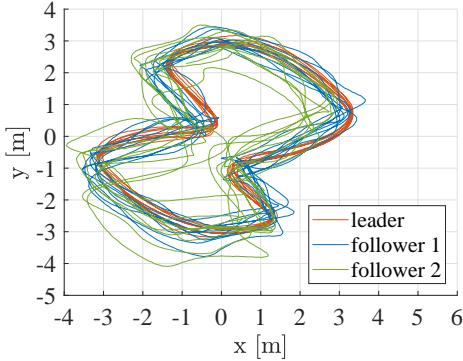


Fig. 31. Trajectory of leader and two followers using only on-board information

TABLE II. COMPARISON OF MEAN LOCALIZATION (LOC.) ERRORS AND MEAN TRACKING (TRACK.) ERRORS FOR ALL PERFORMED EXPERIMENTAL FLIGHTS, BOTH FOR MCS AND FULLY ON-BOARD (ON-B.) FLIGHTS.

	1 follower		2 followers			
	MCS	on-b.	MCS 1	MCS 2	on-b. 1	on-b. 2
Loc. error [cm]	18.4	22.6	15.8	43.9	51.8	53.6
Track. error [cm]	46.1	50.8	42.9	70.3	58.6	98.4

executed. We also discuss in more detail the most noteworthy differences between experiments. All the errors are presented in table II.

The first noteworthy observation is the fact that for the experiment with two followers, especially the tracking performance for the second follower is clearly worse than that for the first follower in both the MCS and fully on-board case. This is a byproduct of the fact that the proposed leader-follower control method inherently relies on integration of velocity information in time. As the delay with which the follower must follow the leader increases, so does the period of time over which the follower must integrate its velocity. This is subject to drift, which shows in the tracking performance. This effect is more noticeable in the fully on-board case, since the velocity estimates from optical flow methods are less accurate than the ones computed by the MCS.

Another perhaps unexpected result is that in the experiment with two followers, the localization error for follower 2 in the MCS case is quite a bit higher than that for the first follower. In part this can be explained by the fact that follower 2 has a larger mean range with respect to the leader than follower 1 does (4.2 m compared to 2.9 m). The main reason, however, is the fact that follower 2 has substantially larger ranging errors with the leader than follower 1 does. In figure 32, the ranging error distributions are compared for both drones. Whilst the mean in both cases is close to zero, it is clear to see that the performance is better for follower 1. The distribution for follower 2 is much wider, showing much more frequent high errors. Furthermore, a fragment of the range error in time shown in figure 33 shows that the errors are clearly not random noise. They show a certain trend in time, which will also reflect in the localization errors. Due to the large difference between the ranging performance for followers 1 and 2, there might

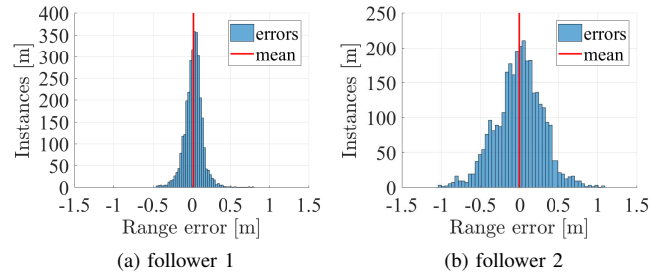


Fig. 32. Comparison between ranging error distributions for follower 1 and 2 for the flight with MCS height and velocity data.

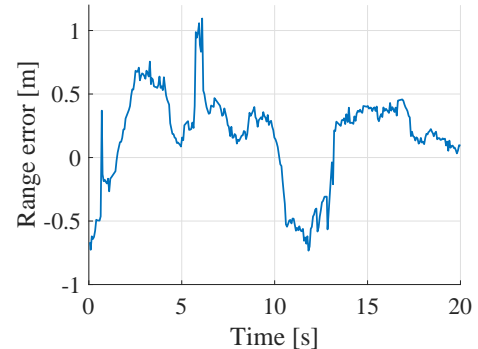


Fig. 33. Range error for follower 2 in time

have been a hardware issue with the specific UWB module on follower 2.

A final result that stands out is the fact that both followers 1 and 2 have substantially higher localization errors in the on-board case than was found for the on-board experiment with a single follower. There is not one reason alone that we can blame for this result, but rather it appears to be a combination of factors that play a role. The increased communication traffic caused a decrease in the filter update rate and also resulted in an increase in ranging frames dropped. Follower 2, as mentioned above, again showed in this flight a worse ranging performance than follower 1. Follower 1, in turn, had slightly less accurate optical flow velocity estimates than were obtained with the single follower flight (21 cm/s MAE compared to 15 cm/s before) and also slightly higher ranging errors than for the single follower flight (15 cm MAE compared to 8 cm before). All factors combined, both followers suffered a comparable degradation in localization performance.

V. DISCUSSION

In this section we will revisit the observability analysis from section II with the obtained experimental data. We will also present some remarks on the scalability of this methodology to larger groups of MAVs.

A. Remarks on observability

We mentioned earlier in section IV that the full observability condition in equation 33 was difficult to directly integrate in

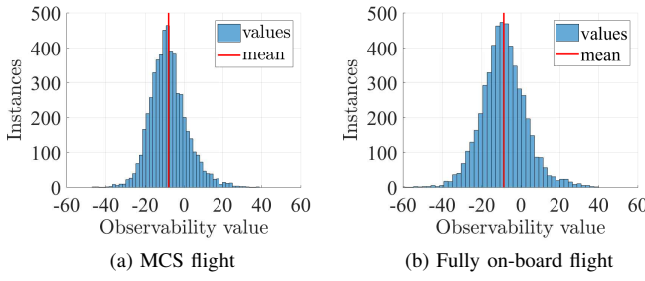


Fig. 34. Histogram of observability values for experiments with one follower

the design of a leader-follower control law, due to the high dimensionality of the condition. However, we demonstrated through numerical evaluations of the equation 33 that, given a particular set of velocities and accelerations for both drones, the set of unobservable relative positions \mathbf{p} was typically very small compared to the set of observable relative positions.

Having the follower fly a delayed version of the leader's trajectory naturally results in varying relative positions between leader and follower, as long as the leader's velocity changes in time. Given the sparsity of unobservable relative positions, we therefore assumed that this control behavior would be sufficient to largely avoid unobservable situations. Even if an unobservable situation would occur, it should only be for a short period in time, as the relative position continuously changes and moves to an observable region again.

Having performed the experiments and collected all the ground truth data, it is possible now to test whether this initial assumption was valid in this case. All the parameters needed to evaluate equation 33 have been logged during the experiments and can simply be inserted into equation 33 to check the observability of the relative localization filter in time. The measure of observability of the system is again represented by the cross product between the left hand side of equation 33 and the relative position vector \mathbf{p} .

The flights that are analyzed are the flights with one follower, for both the MCS and full on-board case. For the flight with MCS height and velocity information, the measure of observability is given in a histogram in figure 34a. For the fully on-board flight, it is shown in figure 34b. A sample of how the observability changes in time is given in figure 35 for the MCS flight and in figure 36 for the on-board flight.

If we again take a threshold of 1, then an observability value between -1 and 1 can be considered unobservable. Again, theoretically only a value of 0 would cause an unobservable system, but because there is noise on the obtained data, the observability measure is not known exactly. Therefore, a somewhat higher threshold is adopted to compensate for the noise on the data.

With this threshold, the unobservable datapoints for the MCS and the on-board flight are 4.76% and 4.75% of all the datapoints respectively. Interestingly enough, this value is virtually the same for both flights.

This percentage will inevitably change depending on what threshold is chosen. However, also a qualitative analysis of

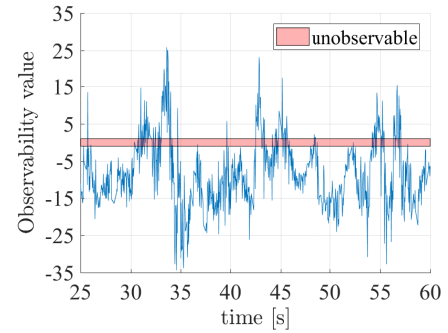


Fig. 35. Observability plot in time for flight with MCS height and velocity information

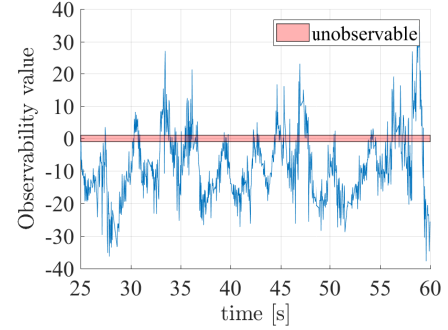


Fig. 36. Observability plot in time for flight with full on-board information

figures 34 to 36 supports that at the very least it is only a small percentage of the data that is unobservable. Most of the data points are well clear of this threshold. It is furthermore visible that unobservable data points are isolated in time, giving the system ample observable data points in between to recover from short periods of unobservability.

We know from the simulations performed in section III that even clearly unobservable scenarios do not immediately lead to big localization errors. Instead, they gradually cause an increase in the localization error in time. Isolated events of unobservability therefore are not expected to cause significant trouble in practice either.

Qualitative inspection of the data indeed shows little correlation between the unobservable regions of the flight and the relative localization error. To demonstrate, the localization error is compared to the observability of the filter in figure 37 for a small segment of the flight with MCS information. For easier comparison, the observability has been reduced to a binary value, where a value of '1' indicates that the system is within the threshold of unobservability at that time. It is clear that there is hardly any correlation, if at all, between these two parameters.

Contrarily, the earlier mentioned occasional dropping of UWB ranging messages shows a very clear correlation with the relative localization error. The two clear spikes in the localization error shown in figure 37 correspond exactly to

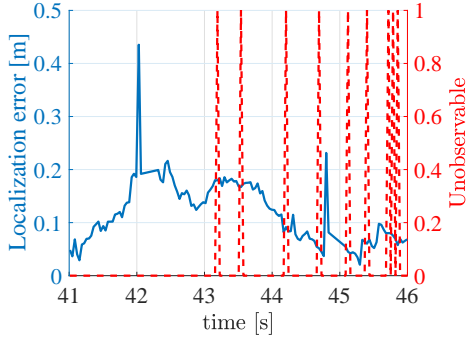


Fig. 37. Comparison between localization error and the observability of the filter. An unobservable value of '1' means the observability measure is within the threshold of unobservability (between -1 and 1)

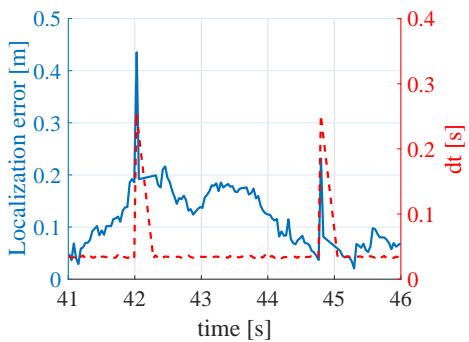


Fig. 38. Comparison between localization error and the time step of UWB ranging message

the times where the UWB communication dropped frames, causing the update timestep dt to rise. This is shown in figure 38.

B. Remarks on scalability

The experimental results in section IV show that the methods in this paper can successfully scale to two followers that follow a leader in a confined area. Even when full on-board sensing is used by the followers, more than three minutes of successful flight were demonstrated without the need for manual intervention.

Whilst this is an impressive result in its own right, analysis of the data does show a substantial rise in localization and tracking errors when scaling up to two drones. This raises the question of what would happen if even more drones are added to the experiment, would this be viable?

One of the results we found is that there is a correlation between especially the tracking performance of the follower and the time delay with which it follows the leader's trajectory. The follower that tracked with a time-delay of eight seconds showed consistently larger tracking errors than the followers with four or five second delays. An alternative solution to the two follower problem is having one follower follow the leader and the other following the first follower. With such an arrangement, both followers could follow another MAV with

the same time delay. This setup has not yet been studied in this work, but could prove to be a better alternative. It is worth looking into this approach in future research.

Another result we found is the reduced update rate when flying with two followers instead of one. Of course adding more drones will always require additional data communication, but a drop from 25 Hz to 16 Hz is quite significant for adding just one more drone.

The main remark to make here is that this reduction in update rate is very much dependent on the software and hardware used for these experiments. It should be possible to significantly increase the update rate to allow for many more drones without having to sacrifice too much on the update rate.

Just to give some examples, in these experiments we operated the UWB modules on the lowest data rate settings (110 kbps). This should theoretically help to improve the ranging accuracy, but in practice will most likely not make a big difference at the small inter-drone ranges occurring in these experiments [47]. The maximum data rate that the UWB modules support is actually 6.8 mbps [47], a factor 680 faster than the data rate used in the experiments. This would clearly allow for much higher update rates, even with three or more drones. One would need to examine however what such a change would have on ranging accuracy and stability.

Furthermore, the UWB modules used in the experiments only operated on a single band of frequencies, namely the frequency band from 4243.2 MHz to 4742.4 MHz. UWB as a standard supports a much wider band of frequencies to transmit on. The DWM1000 itself in fact also supports multiple bands divided in the frequency domain within which the modules can operate [47]. Theoretically, pairs of drones should be able to operate simultaneously on different frequency bands without interfering with each other, which would again result in better scalability to multiple drones. Alternatively, one could look at different UWB radio methods for the communication between drones. Carrier-free variants of UWB, such as direct sequence spread spectrum UWB, can allow for high data throughput on a single, much wider frequency band than the one used by the DWM1000 [48].

VI. CONCLUSION

We have shown in this paper the feasibility of heading-independent range-based relative localization on MAVs. We now know that removing the dependency on a common heading between MAVs has two main disadvantages: the motion of agents must meet more stringent conditions to be observable and the relative localization becomes more susceptible to noise on the range measurements. The clear advantage, on the other hand, is that the filter is no longer affected by local disturbances in Earth's magnetic field. We have shown in simulation that already for small magnetic perturbations, this results in the heading-independent method to perform better than the heading-dependent method.

The results from our observability analysis show that leader-follower flight is especially difficult with the proposed relative localization method. Fixed geometry formation flight will in fact not even be possible. Instead we developed a method

that allows one drone to follow another drone's trajectory with a certain time delay. This approach has been shown to stay sufficiently clear from unobservable conditions, which has allowed us to successfully demonstrate leader-follower flight in practice.

Using only on-board sensory information, one drone can localize another drone with a mean error of just 22.6 cm over 200 seconds of leader-follower flight. This consequently allows the drone to track another drone's trajectory with a mean error of 50.8 cm. The method has been demonstrated to work also with two followers tracking the same leader. In this case the localization and tracking errors do go up, but this is believed to be largely solvable by increasing the communication data rate and consistency.

VII. FUTURE WORK

Despite this promising result, there are still plenty of opportunities to research within the domain of range based relative localization. For certain one of the opportunities is the initial convergence behavior of the filter. The initial conditions that the EKF starts in are important to get a quickly convergent estimate of the relative location of another drone. If the initial condition is too far off from the real situation, the filter can prove very difficult to converge. A primary problem is the fact that there exist ambiguous states where the EKF can converge to, from which it is difficult for the EKF to get out of. It would be interesting in the future to research methods to address these problems. For example the effect of alternative filters like a particle filter could be studied, or running multiple filters in known ambiguous states to identify the correct state more easily.

Furthermore, the current implementation of leader-follower flight uses a lot of past data values and directly uses state values like the velocities of the two drones to implement its control method. It would be interesting to research other methods of accomplishing this type of leader-follower flight. For example it might be possible to perform real time polynomial data fitting on the relative positions of the leader. The resulting polynomial trajectories could instead be used to obtain the velocities and accelerations through analytical derivations of the polynomials. This might result in less data that needs to be stored and smoother trajectories.

Finally, considering the hardware aspect of the experiments in this paper, we have shown the importance of consistent, high frequency communication and ranging. The occasional increase in the time step of the relative localization filter proved more detrimental to the relative localization performance than the occasional unobservability of the filter. It would therefore be valuable to further optimize the frequency and consistency with which ranging messages can be exchanged.

REFERENCES

- [1] E. Şahin, "Swarm Robotics: From Sources of Inspiration to domains of Application," in *Swarm Robotics. SR 2004. Lecture Notes in Computer Science* (E. Şahin and W. Spears, eds.), vol. 3342, pp. 10–20, Springer, 2005.
- [2] M. Brambilla, E. Ferrante, M. Birattari, and M. Dorigo, "Swarm robotics: a review from the swarm engineering perspective," *Swarm Intelligence*, vol. 7, no. 1, pp. 1–41, 2013.
- [3] M. Saska, V. Vonásek, J. Chudoba, J. Thomas, G. Loianno, and V. Kumar, "Swarm Distribution and Deployment for Cooperative Surveillance by Micro-Aerial Vehicles," *Journal of Intelligent & Robotic Systems*, vol. 84, no. 1–4, pp. 469–492, 2016.
- [4] M. Schwager, B. J. Julian, and D. Rus, "Optimal coverage for multiple hovering robots with downward facing cameras," *2009 IEEE International Conference on Robotics and Automation*, pp. 3515–3522, 2009.
- [5] M. Achtelik, Y. Brunet, M. Chli, S. Chatzichristofis, J. D. Decotignie, K. M. Doth, F. Fraundorfer, L. Kneip, D. Gurdan, L. Heng, E. Kosmatopoulos, L. Doitsidis, G. H. Lee, S. Lynen, A. Martinelli, L. Meier, M. Pollefeys, D. Piguet, A. Renzaglia, D. Scaramuzza, R. Siegwart, J. Stumpf, P. Tanskanen, C. Troiani, and S. Weiss, "Sfly: Swarm of micro flying robots," in *2012 IEEE/RSJ International Conference on Intelligent Robots and Systems*, pp. 2649–2650, Oct 2012.
- [6] A. T. Hayes, A. Martinoli, and R. M. Goodman, "Swarm robotic odor localization: Off-line optimization and validation with real robots," *Robotica*, vol. 21, no. 4, pp. 427–441, 2003.
- [7] M. Schwager, J. McLurkin, J.-J. E. Slotine, and D. Rus, "From Theory to Practice: Distributed Coverage Control Experiments with Groups of Robots," in *Springer Tracts in Advanced Robotics* (O. Khatib, V. Kumar, and G. J. Pappas, eds.), vol. 54, pp. 127–136, Berlin: Springer, 2009.
- [8] L. Merino, F. Caballero, J. R. Martinez-de Dios, J. Ferruz, and A. Ollero, "A cooperative perception system for multiple UAVs: Application to automatic detection of forest fires," *Journal of Field Robotics*, vol. 23, no. 3–4, pp. 165–184, 2006.
- [9] R. W. Beard and T. W. McLain, "Multiple uav cooperative search under collision avoidance and limited range communication constraints," in *42nd IEEE International Conference on Decision and Control*, vol. 1, pp. 25–30, Dec 2003.
- [10] M. Coppola, K. McGuire, K. Y. W. Scheper, and G. C. H. E. de Croon, *On-board Communication-based Relative Localization for Collision Avoidance in Micro Air Vehicle teams*. arxiv:1609.08811, submitted on 28 sep 2016.
- [11] S. Roelofsen, D. Gillet, and A. Martinoli, "Reciprocal collision avoidance for quadrotors using on-board visual detection," *2015 IEEE/RSJ International Conference on Intelligent Robots and Systems (IROS)*, pp. 4810–4817, 2015.
- [12] G. Vásárhelyi, C. Virág, G. Somorjai, N. Tarcai, T. Szörényi, T. Neppusz, and T. Vicsek, "Outdoor flocking and formation flight with autonomous aerial robots," in *2014 IEEE/RSJ International Conference on Intelligent Robots and Systems*, pp. 3866–3873, 2014.
- [13] H. Cheng, Y. Chen, and W. S. Wong, "Trajectory tracking and formation flight of autonomous UAVs in GPS-denied environments using onboard sensing," *IEEE Chinese Guidance, Navigation and Control Conference*, pp. 2639–2645, 2014.
- [14] Y. Gu, B. Seanor, G. Campa, M. R. Napolitano, L. Rowe, S. Gururajan, and S. Wan, "Design and Flight Testing Evaluation of Formation Control Laws," *IEEE Transactions on Control Systems Technology*, vol. 14, no. 6, pp. 1105–1112, 2006.
- [15] Y. Mulgaonkar, G. Cross, and V. Kumar, "Design of small, safe and robust quadrotor swarms," in *2015 IEEE International Conference on Robotics and Automation (ICRA)*, pp. 2208–2215, 2015.
- [16] A. Kushleyev, D. Mellinger, C. Powers, and V. Kumar, "Towards a swarm of agile micro quadrotors," *Autonomous Robots*, vol. 35, no. 4, pp. 287–300, 2013.
- [17] N. Michael, D. Mellinger, Q. Lindsey, and V. Kumar, "The GRASP Multiple Micro-UAV Test Bed: Experimental evaluation of multirobot

- aerial control algorithms,” *IEEE Robotics & Automation Magazine*, vol. 17, no. 3, pp. 56–65, 2010.
- [18] M. Turpin, N. Michael, and V. Kumar, “Decentralized formation control with variable shapes for aerial robots,” *2012 IEEE International Conference on Robotics and Automation*, pp. 23–30, 2012.
- [19] S. H. Chiew, W. Zhao, and T. H. Go, “Swarming Coordination with Robust Control Lyapunov Function Approach,” *Journal of Intelligent and Robotic Systems*, vol. 78, no. 3, pp. 499–515, 2015.
- [20] A. T. Hayes and P. Dormiani-Tabatabaei, “Self-organized flocking with agent failure: Off-line optimization and demonstration with real robots,” in *2002 IEEE International Conference on Robotics and Automation*, pp. 3900–3905, 2002.
- [21] S. A. P. Quintero, G. E. Collins, and J. P. Hespanha, “Flocking with fixed-wing UAVs for distributed sensing: A stochastic optimal control approach,” in *Proceedings of the American Control Conference*, pp. 2025–2031, 2013.
- [22] S. Hauer, S. Leven, M. Varga, F. Ruini, A. Cangelosi, J. C. Zufferey, and D. Floreano, “Reynolds flocking in reality with fixed-wing robots: Communication range vs. maximum turning rate,” in *2011 IEEE/RSJ International Conference on Intelligent Robots and Systems*, pp. 5015–5020, Sept 2011.
- [23] T. Nägeli, C. Conte, A. Domahidi, M. Morari, and O. Hilliges, “Environment-independent Formation Flight for Micro Aerial Vehicles,” in *2014 IEEE/RSJ International Conference on Intelligent Robots and Systems*, pp. 1141–1146, 2014.
- [24] H. Liu, H. Darabi, P. Banerjee, and J. Liu, “Survey of Wireless Indoor Positioning Techniques and Systems,” *IEEE Transactions on Systems, Man, and Cybernetics, Part C (Applications and Reviews)*, vol. 37, no. 6, pp. 1067–1080, 2007.
- [25] T. M. Nguyen, A. H. Zaini, K. Guo, and L. Xie, “An Ultra-Wideband-based Multi-UAV Localization System in GPS-denied environments,” in *International micro air vehicle competition and conference 2016*, pp. 56–61, 2016.
- [26] A. Iyer, L. Rayas, and A. Bennett, “Formation Control for Cooperative Localization of MAV Swarms (Demonstration),” in *Proceedings of the 2013 International Conference on Autonomous Agents and Multi-agent Systems*, pp. 1371–1372, 2013.
- [27] P. Conroy, D. Bareiss, M. Beall, and J. van den Berg, “3-D Reciprocal Collision Avoidance on Physical Quadrotor Helicopters with On-Board Sensing for Relative Positioning,” arXiv:1411.3794, submitted on 14 Nov 2014.
- [28] M. Kriegleder, S. T. Digumarti, R. Oung, and R. D’Andrea, “Rendezvous with bearing-only information and limited sensing range,” in *2015 IEEE International Conference on Robotics and Automation*, pp. 5941–5947, 2015.
- [29] T. Stirling, J. Roberts, J.-C. Zufferey, and D. Floreano, “Indoor navigation with a swarm of flying robots,” in *2012 IEEE International Conference on Robotics and Automation*, pp. 4641–4647, 2012.
- [30] J. F. Roberts, T. Stirling, J.-C. Zufferey, and D. Floreano, “3-D relative positioning sensor for indoor flying robots,” *Autonomous Robots*, vol. 33, no. 1-2, pp. 5–20, 2012.
- [31] K. Guo, Z. Qiu, W. Meng, L. Xie, and R. Teo, “Ultra-wideband based cooperative relative localization algorithm and experiments for multiple unmanned aerial vehicles in GPS denied environments,” *International Journal of Micro Air Vehicles*, vol. 9, no. 3, pp. 169–186, 2017.
- [32] M. H. Afzal, V. Renaudin, and G. Lachapelle, “Assessment of Indoor Magnetic Field Anomalies using Multiple Magnetometers,” *23rd International Technical Meeting of the Satellite Division of the Institute of Navigation*, pp. 525–533, 2010.
- [33] D. Roetenberg, H. J. Luinge, C. T. M. Baten, and P. H. Veltink, “Compensation of magnetic disturbances improves inertial and magnetic sensing of human body segment orientation,” *IEEE Transactions on Neural Systems and Rehabilitation Engineering*, vol. 13, no. 3, pp. 395–405, 2005.
- [34] D. Roetenberg, C. T. M. Baten, and P. H. Veltink, “Estimating body segment orientation by applying inertial and magnetic sensing near ferromagnetic materials,” *IEEE Transactions on Neural Systems and Rehabilitation Engineering*, vol. 15, no. 3, pp. 469–471, 2007.
- [35] M. H. Afzal, V. Renaudin, and G. Lachapelle, “Use of earth’s magnetic field for mitigating gyroscope errors regardless of magnetic perturbation,” *Sensors*, vol. 11, no. 12, pp. 11390–11414, 2011.
- [36] X. Yuan, S. Yu, S. Zhang, G. Wang, and S. Liu, “Quaternion-based unscented kalman filter for accurate indoor heading estimation using wearable multi-sensor system,” *Sensors*, vol. 15, no. 5, pp. 10872–10890, 2015.
- [37] X. Li, Q. Zhou, S. Lu, and H. Lu, “A new method of double electric compass for localization in automobile navigation,” in *2006 International Conference on Mechatronics and Automation*, pp. 514–519, 2006.
- [38] X. S. Zhou and S. I. Roumeliotis, “Robot-to-robot relative pose estimation from range measurements,” *IEEE Transactions on Robotics*, vol. 24, no. 6, pp. 1379–1393, 2008.
- [39] A. Martinelli and R. Siegwart, “Observability analysis for mobile robot localization,” in *2005 IEEE/RSJ International Conference on Intelligent Robots and Systems*, pp. 1471–1476, Aug 2005.
- [40] R. Hermann and A. J. Krener, “Nonlinear Controllability and Observability,” *IEEE Transactions on Automatic Control*, vol. 22, no. 5, pp. 728–740, 1977.
- [41] M. Saska, J. Vakula, and L. Preucil, “Swarms of micro aerial vehicles stabilized under a visual relative localization,” in *2014 IEEE International Conference on Robotics and Automation*, pp. 3570–3575, 2014.
- [42] N. S. Correal, S. Kyperountas, Q. Shi, and M. Welborn, “An UWB Relative Location System,” in *2003 IEEE Conference on Ultra Wideband Systems and Technologies*, pp. 394–397, 2003.
- [43] M. Z. Win and R. A. Scholtz, “Impulse radio: how it works,” *IEEE Communications Letters*, vol. 2, no. 2, pp. 36–38, 1998.
- [44] J. Foerster, E. Green, S. Somayazulu, and D. Leeper, “Ultra-Wideband Technology for Short- or Medium-Range Wireless Communications,” *Intel Technology Journal*, vol. 2, 2001.
- [45] A. F. Molisch, D. Cassioli, C.-C. Chong, S. Emami, A. Fort, B. Kannan, J. Karedal, J. Kunisch, H. G. Schantz, K. Siwiak, and M. Z. Win, “A comprehensive standardized model for ultrawideband propagation channels,” *IEEE Transactions on Antennas and Propagation*, vol. 54, no. 11, pp. 3151–3166, 2006.
- [46] D. Neirynck, E. Luk, and M. McLaughlin, “An alternative double-sided two-way ranging method,” in *13th Workshop on Positioning, Navigation and Communications (WPNC)*, 2016.
- [47] DecaWave, “DW1000 user manual.” https://www.decawave.com/sites/default/files/dw1000_user_manual_2.12.pdf. [Online] Accessed: 15 February 2018.
- [48] H. Nikookar and R. Prasad, *Introduction to Ultra Wideband for Wireless Communications*. Springer Netherlands, 1 ed., 2009.

Part II

Literature Review

Chapter 2

Overview of Localization Hardware

In this chapter a more thorough analysis of different types of available (relative) localization hardware is given. This analysis was formed by gathering from the literature the hardware that have previously been used in different swarm robotics papers for the task of (relative) localization. The different hardware solutions will be coherently mapped in section 2-1. Afterwards these systems are evaluated with respect to their use within this thesis in section 2-2.

2-1 Overview of Hardware Used in Swarm Robotics

An overview of what type of localization hardware has been used in successful demonstrations of swarm robotics will be identified in this section. The overview is presented in table 2-1. The table shows the different articles on swarm robotics that have been studied, and marks the corresponding system(s) that were used in the respective articles to accomplish swarm robotics.

Whilst most of the categories are quite self explanatory, the final two categories “Radio for communication” and “Radio for localization” might need some clarification. Many of the articles on swarm robotics actually use some form of radio. However, most of the articles only use this radio for communication, for example by communicating positional data from an overhead Motion Capture System. Since the topic of this thesis is about using radio for more than just communication, but also directly for relative localization, this has been given a separate category.

2-2 Trade-off Between Different Hardware Systems used in Swarm-ing

The overview in table 2-1 provides a good indication of what type of systems are used in swarm robotics to date. The different systems will now further be examined to determine the most suitable system within the context of this thesis.

Table 2-1: Overview of systems that have been used to demonstrate swarm robotic behaviors in the literature

Article	Motion Capture System	GPS	Systems Found in Swarming Literature				Radio for communication	Radio for localization
			Infrared based	Vision based	Sound based			
Schwager et al. [103]	x		x				x	
Melhuish et al. [72]			x					
Kriegleder et al. [59]			x					
Kernbach and Kernbach [53]			x					
Groß et al. [16]				x				
Alers et al. [6]				x			x	
Mataric [49]			x				x	
Nägeli et al. [80]				x			x	
Basiri et al. [10]					x			
Iyer et al. [48]					x			
Mulgaonkar et al. [78]	x						x	
Kushleyev et al. [61]	x						x	
Michael et al. [74]	x						x	
Turpin et al. [107]	x						x	
Das et al. [24]				x				
Gu et al. [37]			x				x	
Saska et al. [100]			x		x			
Schwager et al. [102]	x						x	
Achtelik et al. [1]			x				x	
Stirling et al. [104]				x			x	
Correll et al. [23]				x				
Rothermich et al. [96]				x				
Hayes et al. [44]				x			x	
Hayes et al. [43]	x			x			x	
Vasarhelyi [108]			x				x	
Quintero et al. [88]			x					
Hauert et al. [42]			x				x	
Celikkamat et al. [18]				x			x	
Kelly and Keating [52]				x		x		
Chiew et al. [20]	x				x		x	
McLurkin and Smith [71]				x	x			
Pestana et al. [84]					x		x	
Coppola et al. [21]							x	
Guo et al. [39]							x	x
Total uses			8	6	13	8	2	21
								2

2-2-1 External Systems

The first few systems that will be discussed are grouped together under the term **external systems**. These are systems that are not (fully) carried on-board the robot, but still facilitate the robots in the swarming task. It typically accomplishes this by providing the robots with global localization data.

The first set of systems belong to the category of **Motion Capture Systems** (MCSs), such as the popular Vicon MCS used in [20, 61, 74, 78, 102, 107], or other overhead camera

systems such as used in [43, 103]. The advantage of using MCSs in swarming experiments is the very high accuracy (down to millimeter and sub-degree accuracy for the Vicon MCS [109]) with which these systems can give pose information to the robots in the swarm, and the relatively high update rate with which it can provide this pose information (often about 50-150 Hz is mentioned in the literature [61, 102, 107]). In order for the robots to actually receive the position information provided by the MCS they must also always be equipped with some communication system (usually wireless) that sends the computed position by the MCS to the robot, since the MCS is the system that computes the position, and not the robots themselves. The main advantage of such a MCS is that the high accuracy of pose information allows the robots to operate with nearly perfect state knowledge of themselves, and potentially of other robots as well. A lot of the theoretical work performed on swarming assumes for example that robots in the swarm have perfect knowledge of (part of) the state of other robots and their own. The close resemblance of a MCS to perfect state knowledge makes the jump from theoretical considerations to practical experiments as small as possible. This allows for quick “proofs-of-concept” with robots, to show that a theoretical work can also work in practice. The major downside is that such a system has to be installed at the location of the experiment. This restricts these applications to function only within a small area covered by the MCS.

The second external system that is often utilized in the literature on swarming is the **Global Navigation Satellite System (GNSS) / Global Position System (GPS)** receiver. Much like for the MCS the GPS receiver allows an external system to help the robots localize. Differently than for the MCS however is that GPS is available in most places around the world. The only restriction it imposes is that there must be a clear reception of the GPS signal. In practice this means that the GPS signal cannot reliably be used indoors due to signal attenuation [67], but also cannot be used in some urban environments and for example forests due to multipath effects [82]. However, even with a clear GPS signal reception the accuracy of GPS leaves much to be desired, which in the domain of robotic swarming would result in large minimum inter-agent separation distances [80]. GPS therefore provides a more wide-spread support than MCS, but is not even close to providing equally high accuracy. Furthermore, a single GPS receiver also only provides positional information (and possibly heading), rather than the position and full orientation that an MCS is typically capable of providing.

Other forms of external localization systems exist with a similar functionality of a MCS. Examples are **(ultra-)sound based indoor localization** system, **wireless Radio Frequency (RF) based indoor localization** systems, and **magnetism based indoor localization** systems [38]. Each provide an alternative system for indoor localization and each have their own advantages and disadvantages. These systems have not been seen to a great extent in swarming related literature by the present author. In any case for all these systems the same major disadvantage holds as for the MCS, which is that it provides localization information only within the relatively small coverage area.

2-2-2 On-board Systems

The external systems mentioned so far provide location information to robots. As mentioned, these systems have clear disadvantages as to where they can be used exactly. In order to

not be reliant on such external systems, on-board sensors would have to be used for robots to obtain the relative locations of neighboring agents in a swarm.

One of the most frequently occurring on-board hardware in the robotic swarming literature is the **Infrared (IR)** sensor, and this is for good reason. IR is Electromagnetic (EM) radiation with a frequency just below the frequencies of visible light. With wireless communication becoming increasingly popular in all sorts of applications, using IR instead of RF communication allows an IR based system to bypass the issues associated with EM interference to and from other systems operating in the common RF bands occupied by for example WiFi or Bluetooth [31]. Furthermore the IR based sensors are very versatile, since they can be used not only for relative localization of other swarm members, but also for proximity sensing/obstacle detection (in a "radar" like fashion) and for communication. This allows researchers to use a single IR based sensor for a variety of purposes. This is also reflected in the uses of IR in swarming in the literature. For example in articles [52, 72, 96] IR sensors are used for relative localization and communication, in articles [23, 53] IR sensors are used for proximity sensing and communication, and McLurkin and Smith even used IR sensors for all three of these applications in [71], making the IR sensor a very efficient sensor indeed. Naturally there are also weaknesses associated with using IR sensors in swarming. Because IR is just a form of light, it will not be able to penetrate any sort of opaque material. This means in practice that IR systems can only work together when they are within the same room [38]. Furthermore, whilst IR is naturally immune to interference from wireless RF signals, it is in fact influenced by the presence of other disturbing sources, including ambient light (both sunlight and artificial light). [31]. Finally, a major downside especially also in robotic swarming is that IR systems have limited Field Of View (FOV). To get the wider coverage required for good relative localization, this will ultimately lead to relatively heavy constructions of multiple sensors in different orientations, such as the ring of IR sensors developed in [94].

Rather than using the IR portion of the light spectrum, others propose to directly use the visible light spectrum in swarming applications in the **vision based** methods for relative localization. A large variety of methods are employed for vision based localization. Some authors suggest to directly estimate the positions of other agents in a swarm, requiring the robots to identify others directly in the video captured by their camera(s). This is often facilitated by equipping the robots with easily identifiable markers of for example distinct colors or patterns, as is demonstrated in [48, 80, 95]. Other approaches attempt to use the camera images to create a map of the environment within which the agents can localize themselves. Via communication the agents can then determine what their locations within this map should be to efficiently execute a desired behavior [1]. This group of methods is referred to as Simultaneous Localization and Mapping (SLAM). In reality SLAM is a broader concept that can also be used in combination with other sensors like laser scanners, but those have not been seen in swarm robotics literature. The downside of especially SLAM is that it is computationally expensive, and requires a lot of communication bandwidth when multiple drones are trying to match their individual maps. This is unfavorable for aerial swarm robotics, since these are both scarce resources. Furthermore, all vision based methods suffer from high dependency on illumination and visual contrast of the scenery, can be erroneous when there are insufficient features present in the environment, and might not be able to provide the required high framerates for highly dynamic tasks

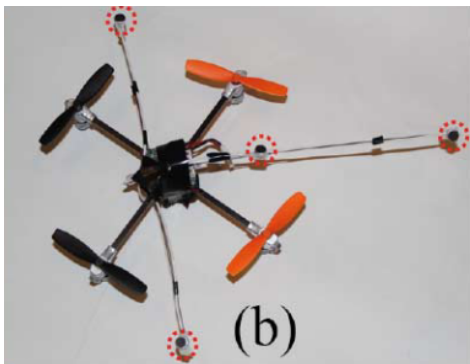


Figure 2-1: Microphone array on a pocket drone [10]

[9, 10]. Vision based methods are also restricted to Line Of Sight (LOS) operation and typically have limited FOV. The demonstrations of swarming behavior using vision based methods so far are with a very limited number of agents (2-3) and do not adequately show scalability of the systems to larger number of agents due to the need to either actively track specific neighbors as in [80], or due to the lack of real-time interaction between agents as in [1].

Alternative to the aforementioned systems are the **onboard sound based systems** which are also capable of providing relative localization information between robots. These systems are far more uncommon in the literature on practical swarming implementations, and have primarily been shown by Basiri et al. in [10] for the case of formation flying. The authors mention some distinct advantages of the sound based system over the aforementioned systems such as the independence of the system on illumination conditions, allowing the system to operate during day and night. The sound waves used for detection can travel through certain obstacles allowing reception of the signal even in the case of some occlusions. Finally the microphones are omnidirectional allowing 3D reception of sound signals [10]. There are some significant disadvantages with respect to swarming applications based on the sound based system, however. Basiri et al. already showed in the experimental results in [10] that the localization performance of the system significantly drops when the number of agents to be localized is increased. In the experiments it was demonstrated that up to three agents were localized with relatively good accuracy, but introducing a fourth agent proved already to be too much. This was in a controlled environment with relatively little disturbing sounds present. Clearly for a swarming purpose this is not desirable since the system should ideally support many more members than three. Furthermore, whilst the microphones can be relatively light, the authors in [10] use the difference in arrival times of sound at different microphones to get a bearing estimate of other agents. This requires the microphones to be spatially separated, resulting in somewhat inconvenient constructions to get such a microphone array installed on a pocket-sized drone (see figure 2-1 for the solution by Basiri et al.).

There is a final group of on-board systems that have been used in the literature and that shows potential for swarm robotics, the **Radio Frequency (RF) based systems**. Much like IR systems, the RF based systems are very versatile in their use, being capable of communication, proximity sensing, and localization. Furthermore the RF based systems are just like the sound based systems omnidirectional and independent of ambient light conditions.

As mentioned in section 2-1, the RF based systems have been divided into two separate categories for the purpose of this hardware evaluation. This is done to make the distinction between different uses of RF based systems more pronounced. Most of the literature on swarm robotics uses some type of RF based system in their execution of swarm robotics. For the most part, however, this RF based system only functions as an auxiliary communication system. For example, any solution that uses a MCS to determine the robots' positions requires the robots to be equipped with a wireless communication system. This is necessary to be able to communicate the externally determined positions to the robots themselves. For GPS, if the robots must have knowledge of the relative locations of each other, a wireless communication system is necessary to exchange positions amongst members of the swarm. Even if there is no need to exchange position data, other authors use the RF based methods to communicate important variables to accomplish a certain swarming behavior. For these reasons, RF based systems are very popular in swarm robotics implementations.

However, as mentioned, RF systems are capable of more than just communication. The wireless radio signals themselves can be used as a source of information to extract for example the range between two RF modules. Since so few authors exploit this possibility of RF systems, it has been given a separate category.

Recent research has shown that RF based systems can be used for relative localization without using external beacons, thus using only onboard radio transceivers. This has been shown with Bluetooth signals by Coppola et al. in [21] where they accomplished relative localization between drones by combining ranging information from signal strength measurements with communicated velocity, heading, and height information between drones. In their final experiment, all the required information is collected through on-board sensors and subsequently fused in an Extended Kalman Filter (EKF). They used this information for collision avoidance behavior, which can be considered a prerequisite for swarming. They managed to avoid collisions between two drones using only onboard sensing for an average time of 192.4 seconds in a 4 x 4 meter arena.

Very recently a similar methodology has also been investigated by Guo et al. in [39] where they used Ultra-Wideband (UWB) radio instead of Bluetooth. Here they first have one drone hovering in a static position, thus acting as a sort of beacon, which allows another drone to get an estimate of its position relative to the static drone. This is done by having the moving drone fly a certain path, and having it collect ranging information at several locations. The flying drone keeps track of the displacements that occurred between the different range measurements, allowing it to get an estimate of its position through classical lateration. Afterwards, all drones are allowed to move and continue to obtain relative location estimates through a combination of range measurements and communication of self-displacements.

2-2-3 Best Hardware System in Robotic Swarming

Clearly the best (set of) systems to be used in robotic swarming depends on a great deal of things, such as the robots used, the behavior they must achieve, and the location they must achieve it in. By focusing on specifically swarming with MAVs, and in an indoor location, one can make some sensible conclusions regarding applicable sensor systems. The requirements that stem from the fact that the robot to be used will be a MAV are:

- The on-board system must be small.

- The on-board system must be light weight.
- The system must work with limited available computational power.
- The system must be scalable.
- The system must be operable in unprepared indoor environments.

Since the system must be operable in unprepared indoor environments, the external systems (such as MCSs and GPS based systems) are not suitable for the application in mind. This therefore leaves only the on-board systems as suitable contestants.

From the on-board systems the sound based systems drop as a candidate system due to the fact that the results from these systems show insufficient scalability to larger numbers of robots.

Alternatively the vision based systems may be used. However, the vision based methods also do not provide promising scalability, mainly due to the fact that vision based systems have limited FOV and therefore must have either multiple cameras, which will be heavy, or must actively track neighboring robots, which is impractical for large numbers of robots. Furthermore out of the considered methods the vision based methods require the highest computational power which is also a limiting factor on MAVs.

Despite the versatility of the IR based systems, these are also not a suitable solution within the current context due to their limited FOV. The bulky constructions that are required to get a decent FOV with IR based systems do not meet the criteria of being small and light weight.

This leaves the most suitable candidate system, the RF based systems. It is a versatile system, given that it is capable of serving as a communication device, a proximity sensors, and has been used for the purpose of relative localization. A big advantage is also the fact that it is omnidirectional. A drawback of the RF based system is that it is not a completely standalone system. It requires additional information (such as velocity, height, or other state variables) to be exchanged between agents in a swarm to get a full three dimensional relative localization fix. This means that the accuracy of the system will inevitably be affected by the quality with which the additional state variables are obtained. Nevertheless, since the individual members in a swarm need this state information to be able to fly anyways, it is assumed that this information is available to them with sufficient accuracy.

2-2-4 Selection of Radio Technology

The question that remains, however, is what specific type of radio to use. Within the context of this thesis it has been decided to pursue the UWB technology for indoor leader-follower flight, and there are a number of good reasons for this choice.

Whilst technologies like Bluetooth, WiFi, ZigBee, and UWB are all protocol standards that enable short-range wireless communications with low power consumption [64], UWB separates itself from other standards in a number of ways. Bluetooth, WiFi, and ZigBee operate on a narrow range of frequencies, and mostly around the 2.4 GHz region. UWB instead transmits on a very wide range of frequencies, typically ranging from about 3.1 to 10.6 GHz [64]. This brings with a number of advantages.

The main advantage that can be attributed to the bandwidth used by UWB signals is that they result in very fine temporal (and thus spatial) resolution [22]. This in turn allows it to

resolve multipaths more easily [110]. Ultimately these properties help to make the ranging performance of an UWB system very accurate, which is obviously important when the desire is to use it in a localization system.

Another advantage associated with this bandwidth allocation is that it provides natural resistance to interference from the many wireless signals that are transmitted at any moment. UWB can be used in close proximity to other RF signals [33, 67, 76] due to the fact that it operates on a very wide frequency band and does not solely rely on any narrow band of frequency like many other radio standards do.

UWB also has a very high theoretical spatial capacity. This means that per unit of area, UWB can theoretically send a very large amount of data [33]. Especially in the case of swarming, where many different agents might wish to transmit data in close proximity, it is a very useful property for the signal to be capable of providing such high theoretical data rates in the space available. This can partially be explained by looking at Shannen's equation which relates channel capacity to bandwidth:

$$C = W \log_2 \left(1 + \frac{S}{N} \right) \quad (2-1)$$

Where C is the channel capacity in bits/second, W is the channel bandwidth in Hz, S is the signal power and N is the noise power. This equation clearly tells us that the maximum channel capacity C increases linearly with the signal bandwidth W . This fact immediately tells us that the high bandwidth used by UWB systems is favorable for the channel capacity that the technology supports.

An additional advantage of UWB that is useful for swarming applications where robots might not always have the same inter agent distance, is the fact that UWB can theoretically quite easily trade off communication speed (bit rates) with communication range [13, 33, 83]. This can be achieved by just sending the same UWB pulse several times in a row to effectively increase the Signal-to-Noise-Ratio (SNR) that is achieved at the receiver [33].

Finally, UWB has relatively favorable material penetrating properties [76]. Clearly in an indoor environment where many walls may be present at close proximity it is favorable if communication between agents remains feasible even if agents are on opposite side of a wall.

Chapter 3

Introduction to Ultra-Wideband technology

UWB is a relatively unknown technology compared to some other wireless technologies. This chapter therefore contains an introduction into UWB technology to familiarize the reader with the technology. The history of the technology will first be briefly discussed in section 3-1. The theoretical foundations behind the technology are discussed in section 3-2. Afterwards some UWB modulation and multiple access techniques will be discussed in respectively sections 3-3 and 3-4. Finally, the legal considerations and regulations regarding UWB will be presented in section 3-5.

3-1 History of Ultra-Wideband

UWB is often perceived as a very contemporary technology that is the result of recent breakthrough in wireless communication, whilst in fact it is already a very old technology. Strictly speaking, UWB can be seen as the oldest form of wireless communications, since the earliest work on wireless communication, the spark-gap transmitter of Marconi (following the work of Hertz), designed in the 1890s, is often perceived as an UWB system due to the physical nature of spark gap transmission (short pulse, high bandwidth transmission) [35, 76, 87]. Unfortunately, said spark gap transmitters generated radio waves in a largely uncontrolled manner [36], and therefore did not seem to allow easy spectrum sharing with other users. In an attempt to allow for a higher degree of spectrum sharing in a controlled manner, and due to the technology being available at the time, the focus in wireless transmission shifted towards more controlled narrowband systems [36, 87]. Through allocating bands of the radio spectrum towards specific purposes, these narrowband systems seemed like a good way to prevent interference between different systems. [36]. The cost, of course, was that this resulted in large portions of the radio spectrum going unused.

The new focus on narrowband wireless communication caused interest in UWB as a communication technology to slowly wane for the decades following the initial successful spark gap transmission. It was not until decades later, around the area of the second world war, that some work relating to UWB communication reappeared in the form of patents filed in the US regarding impulse radio [3]. However, especially during the times of war, the US

government wanted these technologies to remain a secret, and did not grant the patent rights to these patent applications until more than a decade later [3].

Since the 1960s the military and UWB remained intertwined for a long time, as much of the real early UWB systems designed were for military purposes. The military had especial need for Low Probability of Detection (LPD) wireless transmission, and UWB seemed capable of filling that role. For that reason, the early military applications constituted mainly of LPD radar and communication systems [35, 36]. Clearly, due to the military nature of the developments, a lot of the early work regarding UWB was classified [36] and therefore did not help to spark interest for commercial or research applications.

It was actually only in 1989 that the term "ultra-wideband" was first coined by the U.S. Department of Defense [8, 83, 111], and the term "UWB" was used by the Defense Advanced Research Projects Agency (DARPA) in a radar study in 1990 in order to differentiate between conventional and short-pulse radar [35]. Before that time UWB was known under different names, such as "baseband", "impulse" or "carrier-free" radio [35, 83].

Development regarding UWB systems were first accelerated in 1994, when some of the previously classified research material was unclassified [87]. The United States of America's (USA's) Federal Communications Commission (FCC) caught on to the technology, and further accelerated its development in 1998 when they released a Notice of Inquiry that proposed the unlicensed use of UWB. In cooperation with the public they formalized the rules to which UWB systems had to abide in order to operate legally in April 2002 with the release of the First Report and Order regarding UWB [30]. Whilst UWB would be strictly limited in the amount of legally allowable power it can radiate, it was still a very controversial ruling due to the large amount of unlicensed bandwidth that was made available. This was in sharp contrast with the narrow frequency ranges previously available for commercial use. To make the controversy even greater, the allocated bandwidth overlapped with some of the previously allocated narrowband frequencies [36], such as those used by WiFi and GPS.

Rather than just for military operations, commercial companies now started to realize its potential also for the consumer market. UWB was deemed capable of low power communication at both short and long ranges, at respectively high and low data rates [106]. Many articles on UWB were published, and a vast variety of uses for UWB were proposed and envisioned. Examples of these uses are for wireless personal area networks, sensor networks, imaging systems, radar systems, outdoor peer-to-peer networks, intelligent wireless area networks, *etc.* [86, 111].

Upon reading the papers published shortly after the FCC's report and order, UWB appeared like a phenomenon that would surely become a widely adopted technology. However, whilst standards like Bluetooth and WiFi are known by most people today, and are present in many contemporary electronic devices, UWB is largely unknown and only available in niche products. It is not even serving a small portion of its envisioned uses.

One of the large contributions to the failure of UWB to live up to its envisioned potential is the fact that the IEEE failed to come up with a standardized physical layer (PHY) for UWB [17]. The two main contenders for becoming the standard PHY were the Multi-Band UWB (MB-UWB) and Direct Sequence UWB (DS-UWB). Both proposals were backed by different organizations (respectively the WiMedia Alliance and the UWB Forum), and had valid arguments in their favor, making the decision between the two a difficult one. The IEEE 802.15.3a task group, which was the task group tasked with the standardization of UWB, tried for three years to appoint one of the two proposals as the standard, but failed to ever reach the required 75% approval rating to conclude on a standard [17]. The task

group finally recognized its inability to make a decision and unanimously voted to disband at a meeting in Hawaii on January 19, 2006 [36, 83]. Instead, they decided to let the industry determine which of the PHY ought to become the standard. Unfortunately the industry did not do so, and instead started largely to back off from UWB development [17].

To date UWB is not the all-purpose radio technology that it was once hypothesized to be. Most companies that focused on commercial (communication) applications have either backed off from the technology, or have gone bankrupt [17]. Despite the commercial disappointment of the technology, however, it is still a technology with distinct advantages over other RF technologies, as mentioned in section 2-2-4. For that reason there are still researchers to date that investigate its potential, and there are numerous niche applications for which UWB is being used today. An example of this is for real time precision localization, which is also the purpose that this thesis will use UWB for. More information on (contemporary) UWB uses can be found in chapter 4.

3-2 Theory behind Ultra-Wideband

Now that UWB's historical perspective has briefly been introduced, it is time to look at the theoretical foundations of UWB in order to understand what makes the technology appealing.

Somewhat simplistically put, UWB communication consists of a transmitter that emits an EM wave, a wireless channel through which the signal propagates, and a receiver that receives this wave. In order to understand what the signal that is received will look like, one essentially needs two pieces of information. The first piece of information is the signal that is being transmitted (the input), and the second piece of information is the impulse response of the system that this signal propagates through. Mathematically this is described in the well known convolution integral, which tells us that the output $y(t)$ of a Linear Time Invariant (LTI) system with impulse response $h(t)$ in response to an arbitrary input $x(t)$ is given by:

$$y(t) = \int_{-\infty}^{+\infty} h(\tau)x(t - \tau)d\tau \triangleq h(t) * x(t) \quad (3-1)$$

where the $*$ operator is defined to be the convolution operator.

To fully characterize how the received signal therefore looks, one must consider both the impulse response $h(t)$ of the UWB propagation system and the input signals $x(t)$ of UWB. These concepts will both be described in sections 3-2-1 and 3-2-3 respectively.

3-2-1 UWB Channel Impulse Response

The impulse response is the first term appearing in the convolution integral and will be discussed first. As mentioned, the impulse response essentially characterizes the response of the entire system that the input excites. In the study of wireless transmission the impulse response of the channel is referred to as the Channel Impulse Response (CIR).

Whilst there is substantial literature on channel modeling for narrowband wireless channels, these methods cannot automatically be generalized for UWB channels. One of the key reasons for this conclusion is the fact that for narrowband systems the frequency dependent nature of signal reflection may be ignored or assumed constant due to the limited range of frequency

over which a narrowband system radiates. Obviously this cannot equally be assumed for UWB signals, which are characterized by the large range of frequencies that they span [13].

There are essentially two methods of CIR modeling, which are the deterministic and the stochastic method [13]. The deterministic methods are those methods that attempt to model the behavior of a wireless channel specifically in one particular environment. An example of such a method is ray tracing. An example of where this type of channel modeling is used to enhance UWB localization precision is given in [41]. The other method, the stochastic method, is more general. It attempts to model the channel not for a specific location, but instead attempts to model how the channel would typically behave in a generic location by using statistical methods [13]. The following considerations will be regarding stochastic channel models because of their more general nature.

The UWB Channel Impulse Response (CIR) model in its most basic form is essentially a summation of dirac delta functions [83]:

$$h(t) = \sum_{n=1}^N a_n \delta(t - \tau_n) \exp(j\theta_n) \quad (3-2)$$

Where N is the total amount of Multipath Components (MPCs) in the channel, n is the counter of the n th arriving multipath, and a_n , τ_n and θ_n are the amplitude, delay, and phase of the n th arriving MPC. When the UWB that is being considered is a baseband signal, the phase term in equation 3-2 can be excluded [83].

Looking at equation 3-2 one can quickly make some observations as to what the effect of such a CIR will be. Most notable is the effect that a dirac delta function δ has on an arbitrary signal $x(t)$ in a convolution integral. Using the ‘sifting’ property of the dirac delta function in an integral:

$$\int x(t) \delta(t - t_0) = x(t_0) \quad (3-3)$$

and the definition of a convolution (equation 3-1), one quickly arrives at the following property of a dirac delta function in a convolution:

$$x(t) * \delta(t - t_0) = x(t - t_0) \quad (3-4)$$

meaning that the convolution of a signal $x(t)$ with the dirac delta function that is located at t_0 results in a time-shifted version of the signal $x(t)$ where the time shift is equal to t_0 .

Ignoring the phase shift in equation 3-2, the basic CIR is essentially a (finite) sum of these time shifted dirac delta functions. Combining this realization with property 3-4 one quickly realizes that a transmitted wireless signal $x(t)$ after passing through the propagation channel will result in a received signal that is the summation of N time-shifted versions of the transmitted signal $x(t)$. This corresponds with the intuitive notion of MPCs, where the same signal is received with different time delays due to the signal being reflected off of walls, floors, etc. Clearly, in order to be able extract the original direct path of the signal, these MPCs must have minimal overlap in time. This is exactly why UWB is favorable in that sense, since an UWB signal is very narrow in time domain. This will be further demonstrated in the next section.

Other stochastic CIR models for UWB channel modeling exist, but they are mostly based on the standard CIR model presented in equation 3-2 and therefore show similar conclusions

as those that can be made from the basic CIR model. The IEEE also proposed standardized UWB CIR models which are similar to the basic model with some added assumptions on for example the time shifts of the dirac-delta functions (which represent the arrival times of the MPCs). The proposed standardized IEEE models are introduced next.

3-2-2 IEEE Proposed Ultra-Wideband Channel Impulse Response Models

The first standardized CIR model was proposed by the IEEE 802.15.3a task group in [32]. One of the primary assumptions used in the creation of this model was that the arrival times of the different UWB multipath rays at the receiver can be represented as a double poisson process. It is assumed that the different multipaths occur in so-called "clusters" of multipath rays, where both the clusters themselves as well as the individual multipath rays within a cluster arrive according to a poisson process. This model is essentially a slightly modified version of a well known model presented by Saleh and Valenzuela (S-V model) in 1987 (see [99]) where the notion of modeling the arrival times as a double poisson process was introduced. The IEEE model proposed is given by [32]:

$$h(t) = X \sum_{l=0}^L \sum_{k=0}^K \alpha_{k,l} \delta(t - T_l - \tau_{k,l}) \quad (3-5)$$

The assumption of Multipath Components (MPCs) arriving in a double poisson process leads to the double summation present in the IEEE standard model in equation 3-5. This model includes L clusters and a total of K Multipath Components (MPCs) arriving within those clusters. This consequently means that a total of $L \cdot K$ MPCs arrive at the receiver according to this model. Furthermore, $\alpha_{k,l}$ is the multipath gain of the k th MPC arriving in the l th cluster, T_l is the time delay of the l th cluster, and $\tau_{k,l}$ is the time delay of the k th MPC with respect to the delay time of the l th cluster. Finally, the parameter X was introduced to represent the shadowing of the total multipath energy, and is proposed to be log-normally distributed (such that $20\log_{10}(X) \propto \text{Normal}(0, \sigma_x^2)$, where σ_x is the standard deviation corresponding to the variance of the stochastic shadowing effect). The model is valid for the ranges 3-10 GHz in an indoor environment [76].

Clearly it is desirable to have an UWB CIR model that is valid in a more versatile range of environments. A different IEEE task group, namely task group IEEE 802.15.4a recognized the need for this and developed an improved model. The IEEE 802.15.4a task group was also studying UWB systems, but contrarily to their counterpart (802.15.3a) they focused on the alternative low-rate UWB applications for wireless personal area networks (WPANs). They presented their model in a technical report in 2005 [75] and it was later described in an article in 2006 by Molisch et al. [76]. Although the model of the CIR changed only slightly compared to the one presented in equation 3-5, it offers, among others, a more versatile range of environments in which it is valid. Furthermore, despite the group's focus on the low-rate UWB alternative, the model holds for UWB signals at any desired data rate [76].

The alternative IEEE CIR model, again based on the S-V model, is given by:

$$h(t) = \sum_{l=0}^L \sum_{k=0}^K a_{k,l} \exp(j\theta_{k,l}) \delta(t - T_l - \tau_{k,l}) \quad (3-6)$$

Clearly the newly proposed model is similar to the earlier proposed model in equation 3-5. Some differences have been made to the equation though, namely the introduction of the

phase $\theta_{k,l}$ of the arriving MPCs and the exclusion of the shadow fading parameter X .

The reason for putting the phase of the arriving MPCs back into the CIR in equation 3-6 might be due to the need for making the model more versatile and applicable to a wider variety of situations. In the model it was proposed to model the phases of each MPC as a uniform distribution on the range $[0, 2\pi]$, thereby adding some more randomness into the system [76]. Furthermore, excluding the shadow fading parameter seems odd at first (the shadow fading is still present after all), but it becomes clear that rather than having a separate term in the equation for the shadow fading, this phenomenon is now included in the computation of the MPC gains $\alpha_{k,l}$. The full description of how all the different parameters should be computed (used statistical distributions, their fitted parameters, etc.) can be found in [76].

As mentioned, the newly accepted model by the IEEE 802.15.4a task group offers support for a wider variety of environments, both indoor and outdoor, as opposed to the only indoor support of the earlier model presented by IEEE task group 802.15.3a. This can largely be attributed to the fact that the authors of the new model simply present a wider variety of parameters that can be adopted into the model, where every set of parameters represents a new environment [76]. Another big advantage of the new model is that the presented parameters accompanying the model exclude the effects of antennas [76]. This makes the model easier and more versatile in its use and allows comparable results across a wide variety of used systems.

3-2-3 UWB Signal Shapes and Properties

Having the CIR model available is important to understand and model UWB behaviour. However, as equation 3-1 tells us, having the impulse response $h(t)$ available is not enough. Additionally the actual signal that will be sent through the channel must be studied to really characterize an UWB system's performance. Because of the wide range of frequencies allocated for UWB signals, and the different PHY proposals for UWB, there are quite a lot of signal shapes that are proposed to be used in UWB. The most common signal shapes used will be described here. The focus will be on the actual shape of a single signal pulse. Depending on the modulation technique these pulses are congregated in one way or another to form the actual signal. More information on the modulation techniques is given in section 3-3.

The most basic shape of a pulse that can be used in an UWB system is the rectangular monocycle pulse [13]. Its definition in time domain is given by:

$$p(t) = \frac{1}{T_p} [U(t) - U(t - T_p)] \quad (3-7)$$

where $U(t)$ is the unit step function, and T_p is the width of the pulse, which will be in the order of nanoseconds for UWB systems in order to generate the higher bandwidth required for UWB systems. The parameter T_p can be directly used to shape the bandwidth of the signal. This can be seen when taking the Fourier transform of the rectangular monocycle, which is given by:

$$P(f) = \mathcal{F}[p(t)] = \frac{\sin(T_p \pi f)}{\pi f} \quad (3-8)$$

where $P(f)$ is the fourier transform of $p(t)$, and where the \mathcal{F} symbol will be used to char-

acterize the Fourier transform. An example of how the rectangular monocycle pulse looks in both time and frequency domain is given in figure 3-1. In this figure a pulse width of 5 ns is used.

From equation 3-8 it immediately becomes apparent how the pulse width can be used to adjust the bandwidth of the signal, since T_p scales the frequency of the Fourier transformed pulse. Unfortunately the Fourier transform of this signal also reveals that the signal has a strong Direct Current (DC) component. In fact, figure 3-1b shows that the signal peak occurs for zero frequency. This is an undesirable property for EM wave transmission [114], because antennas are not efficient at DC [83]. This is the reason why the rectangular monocycle pulse signal is rarely used in practical systems. However, due to its simplicity it is still often used in academic research [114].

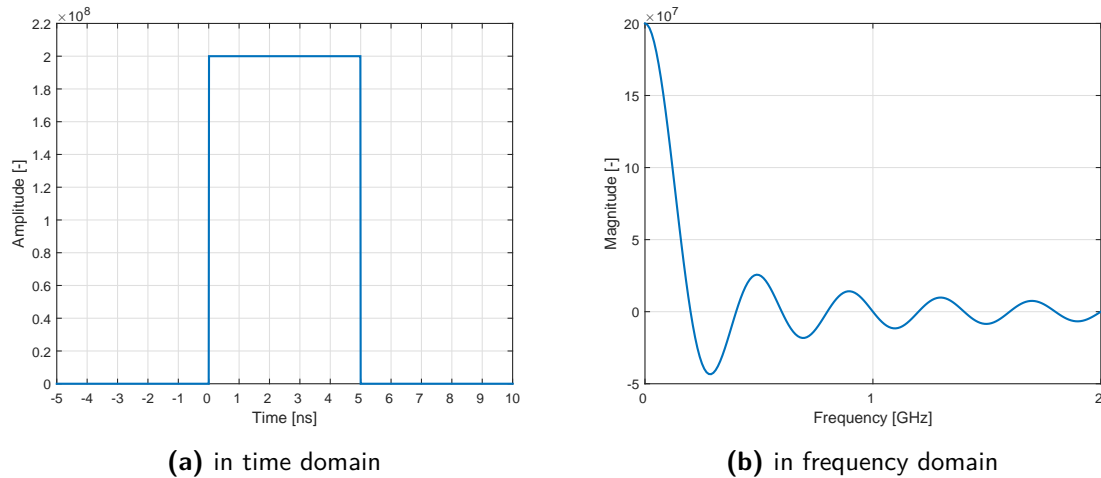


Figure 3-1: Example of a rectangular monocycle pulse

The most typical UWB pulse shape which also has a more practical application, is the Gaussian pulse and the time-derivatives thereof [19, 83]. In time domain the basic Gaussian pulse is given by:

$$p(t) = \frac{A}{\sqrt{2\pi\sigma^2}} \exp\left(-\frac{t^2}{2\sigma^2}\right) \quad (3-9)$$

where in this case A and σ control the amplitude and spread of the signal. For this signal the Fourier transform is given by:

$$P(f) = \mathcal{F}[p(t)] = A \cdot \exp\left(-\frac{(2\pi f \sigma)^2}{2}\right) \quad (3-10)$$

An example of the Gaussian pulse is given in figure 3-2 for a σ value of 0.1 ns. The amplitude A of both the time domain and frequency domain representation has been scaled to have a maximum value of one. In real systems the amplitude would be scaled in order to comply with spectral masks as defined by the relevant authorities (see section 3-5).

Clearly the basic Gaussian pulse still has a relatively large portion of its radiated power in the lower frequencies, which is undesirable. For this reason higher time-derivatives of the

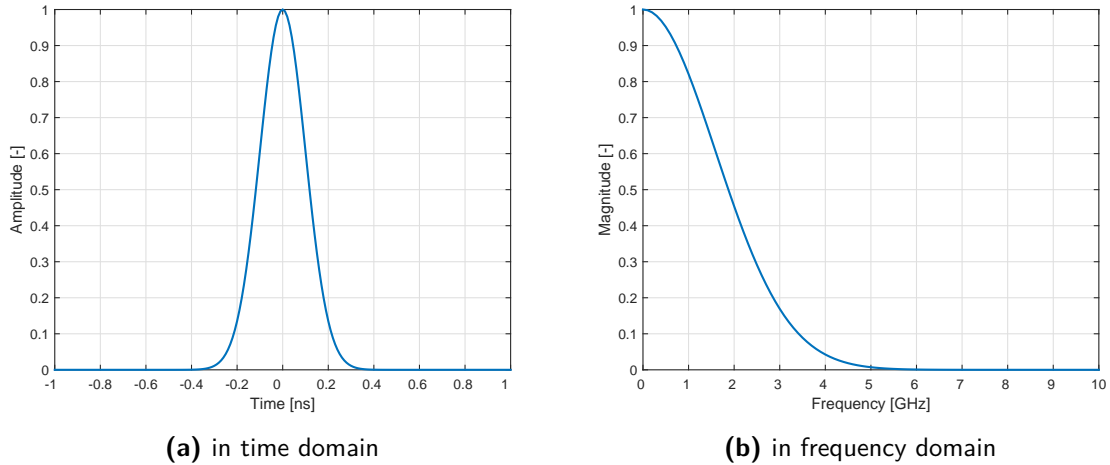


Figure 3-2: Example of a Gaussian pulse

Gaussian pulse can be used instead, since time derivatives of the Gaussian pulse cause the frequency spectrum to shift towards higher frequencies [83].

Because of the properties of the exponential present in the Gaussian pulse, the n th derivative of this pulse can easily be computed in a recursive manner according to the equation from [83]:

$$p^{(n)}(t) = -\frac{n-1}{\sigma^2} p^{(n-2)}(t) - \frac{t}{\sigma^2} p^{(n-1)}(t) \quad (3-11)$$

with the corresponding frequency spectra:

$$P_n(f) = \mathcal{F} [p^{(n)}(t)] = (j2\pi f)^n A \cdot \exp\left(-\frac{(2\pi f\sigma)^2}{2}\right) \quad (3-12)$$

Figure 3-3 shows that indeed time derivatives shift the frequency content of the Gaussian pulse towards higher frequencies by plotting the frequency response of the 1st to the 6th order time derivatives of the Gaussian pulse. Again a signal spread σ of 0.1 ns is used and the amplitude scaled to 1 in order to be able to compare the different frequency responses.

A number of popular UWB signal shapes are not directly derivatives of the Gaussian pulse, but are in some way similar to, or derived from derivatives of the Gaussian pulse. One of the most popular pulse shapes is for example the Gaussian monocycle [90], which is in fact derived from the first derivative of the basic Gaussian pulse [19]. Similarly, the Rayleigh monocycle is another example of a signal shape that is derived from the first derivative of the Gaussian pulse. Finally, the popular Gaussian doublet is in fact simply the addition of two Gaussian pulses (one positive one negative) that are time-shifted with respect to each other [114].

To conclude the section on UWB signal shapes, it is important to mention that the considerations regarding UWB signal shapes in this section, and also those in the literature, concern themselves with the properties of the signal from an analytical perspective. In reality with real physical hardware it will be impossible to generate exact realizations of the analytically

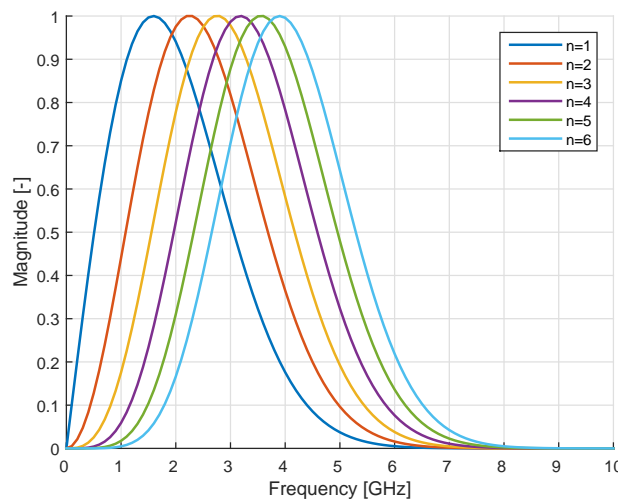


Figure 3-3: 1st to 6th order time derivatives of the Gaussian pulse in frequency domain

described waveforms due to antenna and RF matching problems [13]. The actual transmitted signals will therefore only be approximations of the theoretical signal shapes. In essence the UWB antennas act as filters on the signal that is to be transmitted. The effect of the antenna is often considered to be a differentiation of the pulse to be transmitted [83, 92, 110]. This assumption might however for certain applications be too simplified, as it is also reported in the literature that the UWB antennas shape the signal differently under different angles, as has been experimentally observed [87]. However, as technology evolves, the hardware used is increasingly capable of generating the desired signal shapes accurately.

3-3 UWB Modulation

The discussions so far show the foundations of UWB, but still have not shown how UWB can actually be used to transmit information. In order to do so, one must modulate the signal in order to encode information onto it. How that will be done will be discussed in this section.

One of the most important realizations regarding UWB modulation techniques is that, in the end, “*a radio is a radio*” [3, p.39], and therefore many of the modulation schemes that have previously been invented for any other type of radio, can apply to UWB radio as well. The most popular and common modulation methods for UWB will be discussed.

3-3-1 Pulse Position Modulation

The most popular UWB modulation technique is Pulse Position Modulation (PPM) [83]. PPM is a modulation technique that allows the encoding of information by displacing an UWB pulse in time. PPM essentially divides the time axis into an (infinite) series of “nominal” time positions. Sending an UWB pulse at exactly this nominal time position can for example represent the bit ‘0’. Sending an UWB pulse after the nominal time position can represent the bit ‘1’ [3]. Clearly, it is possible to also allow multiple delays of different lengths within a time slot to allow the coding of additional bits in one time slot.

Mathematically the PPM algorithm for a single user can be represented in time as:

$$x(t) = \sum_{j=-\infty}^{\infty} p(t - jT_f + \delta d_j) \quad (3-13)$$

where $p(t)$ is the signal being emitted in time by a certain UWB transmitter, j is the counter for the amount of time-frames that have past, T_f is the duration of a single time-frame, and δ is a small time-shift. Typically $\delta \ll T_f$ in order to prevent Inter Symbol Interference (ISI) [13]. Finally, the terms d_j encode the bit that is transmitted at time-frame j , where

$$d_j = \begin{cases} 0, & \text{bit } j = 0, \\ 1, & \text{bit } j = 1. \end{cases} \quad (3-14)$$

or similar (for example d_j could also be -1 for bit $j = 0$).

3-3-2 Pulse Amplitude Modulation

A different modulation technique in UWB is the Pulse Amplitude Modulation (PAM). Rather than encoding information by altering the times at which an UWB pulse is being transmitted, this modulation technique encodes information in the amplitude of the pulse that is being transmitted. In time the PAM modulation can be represented as:

$$x(t) = \sum_{j=-\infty}^{\infty} a_j \cdot p(t - jT_f) \quad (3-15)$$

where in this case the addition of a_j is used to encode information. The term a_j scales the amplitude of the pulse $p(t)$ being transmitted, and the amplitude of the transmitted signal can be related to the bit that is being transmitted.

Several possibilities exist with respect to the exact definitions of a_j , and sometimes the different possibilities are also mentioned as separate modulation techniques.

The most simple variant of PAM is called On-Off Keying (OOK) [83]. In OOK modulation the bit '1' is indicated by an amplitude a_j of '1'. Similarly, the modulation of the bit '0' corresponds to an amplitude a_j of '0'. Essentially the system only transmits a pulse when the bit '1' is being transmitted, and transmits nothing otherwise. Note that in this case it is necessary for the receiver of the signal to be aware of the time slots at which bits are transmitted.

Another variant that can be considered an implementation of PAM in specific cases goes by the name of Binary Phase Shift Keying (BPSK), Bi-Phase Modulation (BPM) [83], bipolar signaling [33], or similar. In this type of modulation the amplitude a_j is given the value '+1' in the case of the bit '1', and the value '-1' in the case of a bit '0'. Alternatively the amplitude a_j may also be assigned the complex values $\pm 1 \pm i$, in which case the method is called Quadrature Phase Shift Keying (QPSK), allowing the signal to carry 2 bits of information per pulse [83].

The final variant of PAM is often called M-ary PAM. This method is characterized by the fact that it can transmit more than one or two bits of information per frame of time. It does this by assigning multiple levels of amplitude to the term a_j which allows for additional information being transmitted per frame of time.

3-3-3 Pulse Shape Modulation

The final mentioned modulation technique is Pulse Shape Modulation (PSM). Rather than encoding information in the amplitude or time position of a certain pulse, PSM encodes information into the actual shape of the pulse that is being transmitted. It is again possible to encode multiple bits of information per frame of time, as long as a sufficient set of distinct pulse shapes are available to encode information. Clearly the different pulse shapes must all adhere to the definition of UWB as defined by the appropriate authorities (see section 3-5), and it is at the same time desirable for these pulse shapes to be mutually orthogonal such as to cause minimum interference [13].

3-4 UWB Multiple Access and Spectrum Randomisation

The considerations on UWB modulation in section 3-3 cover essentially how information can be encoded into an UWB data link in the perfect theoretical case of a single transmitter communicating with a single receiver without interference from other users. Naturally in reality a viable wireless technology needs to be able to cope with demand of different users operating in the same area. Essentially it is possible to distinguish between users both from a time domain perspective as well as from a frequency domain perspective. Both of these approaches have been studied specifically in the case of UWB, and these different approaches will be discussed here.

3-4-1 Time-Hopping UWB

One method of allowing for multiple access through time domain separation of users was already introduced by Scholtz in 1993 in [101], and is referred to as Time-Hopping UWB(TH-UWB).

TH-UWB can essentially be used with any of the modulation techniques mentioned in section 3-3, except for OOK. Depending on which of the modulation techniques is used the mathematical description of the complete signal changes slightly. However, when covering the TH-UWB scheme for just one of the modulation techniques, the method can quite easily be extrapolated to the other modulation techniques as well. Since the original work presented TH-UWB in combination with PPM, that is also the combination that will be presented here. The mathematical description of the TH-UWB format with PPM is given for the k th transmitter by [101]:

$$x^{(k)}(t^{(k)}) = \sum_{j=-\infty}^{\infty} p(t^{(k)} - jT_f - c_j^{(k)}T_c - \delta d_{[j/N_s]}^{(k)}) \quad (3-16)$$

Where $t^{(k)}$ is the local time of the k th transmitter, and $p(t)$ is the pulse shape that is being transmitted. The remainder of the equation consists of a number of time shifts, which each have a distinct function.

The first time shift is jT_f , where T_f is the Pulse Repetition Time (PRT) and j is the counter for the transmitted pulses. This time-shift is constant and would result in a uniformly spaced pulse train if it were the only time-shift occurring. It essentially divides the time axis in an infinite number of equal-width time-slots within which a pulse will occur. The time T_f is typically a hundred to a thousand times the width of the pulse being transmitted [101].

The second time shift corresponds with the term $c_j^{(k)}$, which is the pseudorandom time-hopping code, which is distinct for each user k . This term together with T_c provides an additional time-shift of $c_j^{(k)}T_c$ seconds to the j th transmitted pulse of the k th user. The main purpose of the pseudorandom time-hopping code is that it reduces the likeliness that different users consistently send pulses at the same time, because each user will be allocated a new pseudorandom time shift each frame duration.

Finally the actual data is encoded in the term $d_{[j/N_s]}^{(k)}$ which together with the time-shift δ provides the final time-shift of the signal of $\delta d_{[j/N_s]}^{(k)}$ seconds. The subscript $[j/N_s]$ is used to indicate that a single bit is not per definition transmitted only once, but is instead transmitted N_s times. This is done in order to allow the system to achieve higher processing gains (and thereby higher ranges).

What is noteworthy about this technique is its inherent smoothing of the frequency response of the transmitted signal [101, 110]. If an Impulse Radio (IR) based UWB signal transmits pulses with a relatively constant Pulse Repeat Frequency (PRF) this will result in spikes occurring at integer multiples of the PRF in the frequency domain. This will make it hard for an UWB system to remain within the legal spectral mask (see section 3-5 for an introduction into these spectral masks). By introducing randomness into the times at which the UWB pulses are transmitted (both through the pseudo-random time hopping, as well as through the PPM modulation technique in the example given in equation 3-16) these spikes in the frequency domain are smoothed out, which is a desirable property. This is also the reason why the authors originally proposed the TH-UWB method in combination with PPM modulation [101, 110].

3-4-2 Direct Sequence Spread Spectrum Ultra Wideband

The alternative multiple access scheme in time domain is called Direct Sequence Spread Spectrum UWB (DSSS-UWB), and was also one of the technologies that the IEEE considered as a potential candidate for the standard UWB PHY layer. In this technique each user k has assigned a spreading signal $c(t)$ which can be described mathematically as [83]:

$$c^{(k)}(t^{(k)}) = \sum_{j=-\infty}^{\infty} c_j^{(k)} p_{T_c}(t^{(k)} - jT_c) \quad (3-17)$$

Where $c_j^{(k)}$ is a periodic sequence of elements from $\{+1, -1\}$ and $p_{T_c}(t)$ is a pulse with time duration T_c . The signal that the k th user wishes to transmit is indicated as:

$$s^{(k)}(t^{(k)}) = \sum_{j=-\infty}^{\infty} d_j^{(k)} p_T(t^{(k)} - jT) \quad (3-18)$$

Where $d_j^{(k)}$ is again the j th transmitted bit of the k th user, $p_T(t)$ is a pulse with time T . The duration $T \gg T_c$.

Finally, the two time signals are multiplied to produce the final transmitted signal of user k . In other words:

$$x^{(k)}(t^{(k)}) = c^{(k)}(t^{(k)}) \cdot s^{(k)}(t^{(k)}) \quad (3-19)$$

Note that in this description two pulses are multiplied with each other in time domain. Other implementations of DSSS-UWB consider only the case where the original signal is multiplied with fixed values of $\{+1, -1\}$, rather than multiplying it with a second pulse of time T_c . The implementation presented here is more general and can be reduced to the fixed value implementation presented in [13, 114] by choosing as the pulse shape for the spreading signal (p_{T_c}) the unit step function.

A big difference between DS-UWB and TH-UWB is thus that in the case of DSSS-UWB each user k is continuously transmitting a signal. The multiple access is provided by the fact that each user modulates their signal with a spreading sequence, which can later be demodulated at the receiver again for every user k . For TH-UWB each user only sends a signal for a small portion of the time, and the receiver can therefore distinguish between different users by checking the time at which a specific user is supposed to send their signal.

3-4-3 Multi-band Ultra Wideband

Rather than directly modulating data and multiple access through manipulating data in time domain, another approach is to modulate data and multiple access in the frequency domain, which is what the multi-band UWB approach is aimed at.

One specific popular multi-band approach is the Multi-Band Orthogonal Frequency Division Multiplexing (MB-OFDM) UWB scheme, proposed by Batra et al. in 2003 in [11]. This is the alternative proposal to DSSS-UWB that was considered to become a standard UWB PHY layer for the IEEE task group 802.15.3a.

In Batra's proposal the available spectrum of UWB is divided into subbands with a bandwidth of 528 MHz each. The subbands are non-overlapping (hence "orthogonal") and therefore allow theoretically for information to be simultaneously transmitted on each of the subbands without mutual interference. In the proposal, within each subband information is encoded using QPSK modulation. Different users are assigned a subband on which they can transmit information.

3-5 Ultra-Wideband Regulations

Now that an understanding has been formed of how UWB works in theory, it is good to look at the more practical aspects of using UWB technology, and part of these practical considerations is looking at the regulations that hold for using UWB, since those must be adhered to in order to legally use the technology.

As mentioned in section 3-1, the U.S. based FCC was the first to take initiative into allocating legal RF bandwidth for commercial UWB use in April 2002 with the release of its First Report and Order (FRO) [30]. The report not only has significance in the U.S., but also globally, since its outcomes have influenced also the legislation in other areas of the world, and also because many of the research articles abide by the rules imposed by the FCC.

One of the important results of the report is that it finally formalized what type of EM waves are considered UWB, such that debates regarding this issue are henceforth easily solved by using the formal definition. Taking into account the comments of the industry, the FCC finally settled on the following definition for UWB. For a signal to be considered UWB, it must have either:

- A fractional bandwidth greater than 0.2.

- A total bandwidth larger than 500 MHz.

In this case the bandwidth of the signal should be measured at the -10 dB point [30]. The fractional bandwidth mentioned above is defined as $2(f_h - f_l)/(f_h + f_l)$, where f_h and f_l are respectively the upper and lower frequency emission point at the -10 dB point. Furthermore it also defines the center frequency as being $(f_h + f_l)/2$, or equivalently the average value between the upper and lower frequency points. The definition of UWB as mentioned above has as a result that "*UWB systems with a center frequency greater than 2.5 GHz need to have a -10 dB bandwidth of at least 500 megahertz while UWB systems operating with a center frequency below 2.5 GHz need to have a fractional bandwidth of at least 0.20*" [30, p.15].

Apart from formally defining UWB, the FCC also set out in its FRO to define the maximum allowable Effective Isotropic Radiated Power (EIRP) per unit of frequency that UWB devices will be allowed to emit, which is referred to as a spectral mask. The regulations are quite elaborate and also change depending on the type and purpose of an UWB device. For example, a ground penetrating radar system is expected to cause less interference with other devices because most of the radiated power should go into the ground, therefore these systems have slightly less stringent radiation limits than for example communication devices [30].

Most notable is the limit of -41.3 dBm/MHz EIRP for the frequency ranges from 3.1-10.6 GHz. This is also the limit that is most often noted in the literature on UWB (for example in [33, 86, 90]). The reason for this value often being named, despite the fact that the FRO names many more limits depending on the device and frequency range, is probably because this limit occurs for the largest range of frequencies, and because it is the same for most of the different devices and use cases mentioned in the FRO [30]. Interestingly enough, the -41.3 dBm/MHz limit is the same limit set by the FCC to unintentional EM radiators like hair dryers and laptops [36].

As an example, the full spectral mask as reported in the FRO for handheld UWB devices that are not restricted to a specific location is given in table 3-1. These are the most stringent requirements imposed by the FRO due to this category of devices causing the greatest concerns regarding their interference to other devices [30].

Table 3-1: Radiation spectral mask as specified by the FCC for handheld UWB devices [30]

Frequency range [GHz]	EIRP [dBm/MHz]
0.96 - 1.61	-75.3
1.61 - 1.9	-63.3
1.9 - 3.1	-61.3
3.1-10.6	-41.3
Above 10.6	-61.3

The spectral mask notably only allows a very low amount of radiated power for UWB uses, as is obvious from table 3-1. The limit of -41.3 dBm/MHz corresponds to a limit of 75 nW/MHz of EIRP. When integrating this amount over the entire bandwidth of 3.1 to 10.6 GHz this corresponds to a maximum integrated EIRP of 0.56 mW, which is very low. However, despite this low admissible power there is still potential for UWB, because it is the first time such a large amount of bandwidth was made freely available.

Other regions of the world caught on to the potential of UWB and also decided to investigate into UWB regulations. In Europe, the main bodies involved with the regulations are the European Commission (EC), the European Conference of Postal and Telecommunications Administrations (CEPT), the Electronic Communications Committee (ECC) and the European Telecommunications Standards Institute (ETSI).

The CEPT is today comprised of regulatory administrations of 48 countries that work in a cooperative way in the field of radio spectrum usage, telecommunications, *etc.* They often provide the technical knowledge required for the ECC and EC to establish regulations and legislation [29]. The ECC *"brings together 48 countries to develop common policies and non-binding regulations in electronic communications and related applications for Europe..."* [29]. The EC can perform similar tasks, but their decisions are legally binding under EU law [29]. Finally, ETSI is a European standards organization that describes standards regarding Information and Communications Technologies (ICT) related topics [29].

On 18 February 2004 the EC issued its first mandate to the CEPT, after which the CEPT was tasked to investigate the possibilities for harmonized introduction of UWB radio into the European Union. Following CEPT's results, the ECC made a decision on the 24th of March 2006 where they presented technical requirements for UWB devices operating in bands below 10.6 GHz. Following ECC's decision and CEPT's work, the EC published its first decision regarding UWB use on the 21st of February 2007 [26]. In this decision they specify an UWB spectral mask similar to the FCC's spectral mask. This decision was later amended by publications on the 21st of April 2009, and again on the 7th of October 2014 [27].

Noteworthy of the original decision by the EC is the definition of UWB according to EC, which is significantly different than the definition issued by the FCC. According to the EC, ultra-wideband technology is *"equipment incorporating, as an integral part or as an accessory, technology for short-range radiocommunication, involving the intentional generation and transmission of radio-frequency energy that spreads over a frequency range wider than 50 MHz..."* [26]. Whereas according to the FCC a signal must have a minimum bandwidth of 500 MHz or a fractional bandwidth higher than 0.2 in order to be considered an UWB signal, the EC already considers it an UWB signal if its bandwidth exceeds 50 MHz. This clearly allows many more radio signals to apply to the UWB regulation than is the case for the FCC legislation. Clearly this is for the industry advantageous because it gives more freedom in design compared to if the FCC definition were to apply.

However, whilst the definition of UWB allows for more freedom under EC legislation, the opposite is true for the allowable EIRP. Although similar regulations are published by the EC, the EIRP limits are more stringent than the FCC regulations.

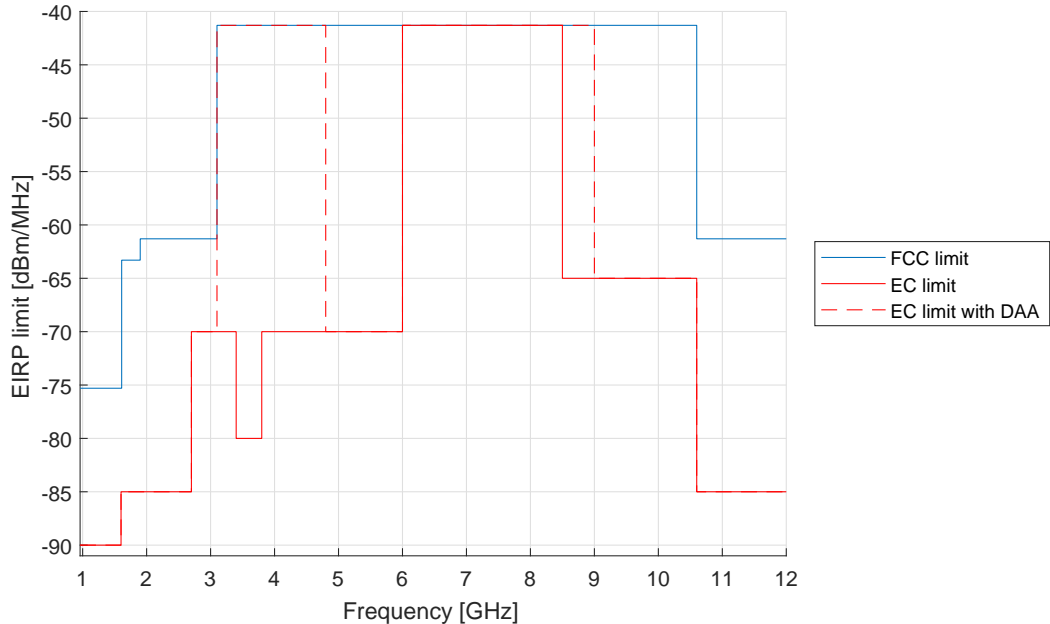
The EC allows somewhat less stringent spectral masks if the UWB products are using Detect and Avoid (DAA) an/or Low Duty Cycle (LDC) techniques. DAA is *"a active mitigation technique for the protection of sensitive potential victim systems in the vicinity of the UWB device based on a sensing approach including an active reduction of the interference potential if required"* [28, p.30]. LDC is *"a limitation to activity of a transmitter within certain time and power boundaries"* [28, p.30].

The most recent spectral mask, as published in [27], is given in table 3-2 for generic UWB usage. For an easy comparison between FCC and EC regulations, the two spectral masks are compared directly in figure 3-4.

It quickly becomes apparent from comparing the spectral masks of the EC in table 3-2 to the FCC spectral mask in table 3-1 that the EC spectral mask is a bit more complicated than the one proposed by the FCC. Another observation of note is that the spectral mask proposed

Table 3-2: Radiation spectral mask as specified by the EC for generic UWB devices [27]

Frequency range [GHz]	Maximum mean EIRP [dBm/MHz]	Maximum peak EIRP [dBm/50MHz]
<1.6	-90	-50
1.6 - 2.7	-85	-45
2.7 - 3.1	-70	-36
3.1 - 3.4	-70 or -41.3 using LDC or DAA	-36 or 0
3.4 - 3.8	-80 or -41.3 using LDC or DAA	-40 or 0
3.8 - 4.8	-70 or -41.3 using LDC or DAA	-30 or 0
4.8 - 6	-70	-30
6 - 8.5	-41.3	0
8.5 - 9	-65 or -41.3 using DAA	-25 or 0
9 - 10.6	-65	-25
>10.6	-85	-45

**Figure 3-4:** EIRP limits for UWB devices according to FCC and EC regulations

by the EC is at best equally lenient as the one proposed by the FCC, and in the other cases the EC spectral mask is more stringent.

Also in the EC spectral mask the limit EIRP of -41.3 dBm/MHz occurs. However, except for the band of 6-8.5 GHz, the EC imposes additional requirements on UWB systems in order to be allowed to radiate -41.3 dBm/MHz. These requirements are that the UWB systems must use DAA and/or LDC techniques. In comparison, the FCC legislation does not require either of these techniques for an UWB device to be allowed to radiate an EIRP of -41.3 dBm/MHz in the band from 3.1 - 10.6 GHz.

Chapter 4

Uses of Ultra-Wideband Technology in the Literature

We know that theoretically, UWB has numerous advantages associated with it. In order to see if these theoretical understandings are also translated into practice, a review of how UWB has been used in the past literature is given in this chapter. This can give us a benchmark for the results obtained in this thesis.

There are essentially three main areas of use for UWB. These areas are localization, radar, and communication. The areas that are most important within the scope of this thesis are localization and communication. This means that the radar capabilities of UWB are less interesting for this thesis. The reasons why that is are given in section 4-1. This leaves the areas of localization and communication, which are discussed in sections 4-2 and 4-3 respectively.

4-1 Localization Compared to Radar

In order to analyze the difference between the localization and radar applications of UWB, it is first important to gain an understanding of what the distinction between them actually is. The distinction made in this work is whether the specific method that is employed to localize a target requires cooperation from the target to be localized (in which case it is considered a localization technology) or not (in which case it is considered a radar technology). In this case cooperation means that the target to be localized is essentially aware that it is being localized, and therefore can participate in the protocol used to determine its location. Contrarily in radar applications the target is often passive and does not participate in the protocol. It simply reflects EM waves which can then be used to determine its location.

The area of radar technology is actually one of the first areas where UWB found a practical use [85]. The first uses of the technology were mostly military due to the Low Probability and Detect (LPD) characteristics of UWB technology. [35] However, since some years UWB radar has also proven to be useful for non-military purposes.

Many of the same advantages that UWB has in the context of localization hold also in the context of radar. An example of especially the UWB frequency content up to 4 GHz is its

ability to penetrate through most non-metallic materials, including many materials used in construction, such as wood, concrete, plastic, rock, *etc.* [58, 97]. This gives it the ability to detect the presence of objects or people even inside of buildings. Other advantages include UWB radar's fine range resolution, its fine angular resolution, its ability to detect stationary targets and previously considered stealth targets, its ability to operate under all weather conditions, and its power efficiency [34, 35, 45]. These advantages can be attributed to the high bandwidth of UWB signals, and their narrow spacing in time.

The favorable material penetration properties of UWB are often exploited in radar applications. For example researchers Sachs et al. report having designed an UWB radar capable of detecting people trapped in rubble [97]. This could be important in search and rescue scenarios where people may be trapped in rubble after for example the event of an earthquake. Researchers Kocur et al. report having designed a handheld UWB radar capable of detecting moving targets through 30 cm thick walls with errors less than a meter [58]. Finally, an entirely different application is reported by Klemm et al. where they use UWB radar for breast cancer detection [56, 57].

It is clear that UWB radar is an interesting topic of research and also shows promising results for different uses. It is still however decided to not pursue this particular use of UWB for the application in this thesis for several reasons.

In the case of localization, the methods required to interpret the signals being propagated back from a target are often much less computationally intensive than those required in the case of radar. The response signal can often be identified using relatively simple procedures, such as threshold and energy detectors, or signal correlation techniques [35]. This is because the signal shape is known *a priori* due to the fact that this is carefully controlled by the transmitters. In the case of radar, where the response signal is a reflected version of the transmitted signal, the shape of the signal is often unknown, because it is altered as it reflects off of the target [46]. For this reason, often many more steps are required to interpret the signals in radar applications. For example, in [58] an UWB radar algorithm takes four different steps (background subtraction, target detection, TOA estimation, wall effect compensation) before it can finally get to the localization part of the algorithm.

Many of the UWB radar applications seek to exploit the material penetrating properties of UWB [58, 68, 79, 97]. This can be a desirable property of radar, as it means that it is even possible to detect targets inside buildings. When considering material penetration, however, it becomes very important that the antennas have a low cut-off frequency [97]. This in turn imposes restrictions on the minimum size of the antenna, often resulting in antenna arrays that will be too large for applications on pocket drones. The localization focused papers instead seek to exploit the fine temporal resolution of the UWB signal, which is best utilized at the higher frequencies. Consequently, these solutions impose less severe restrictions on the minimum antenna size, resulting in smaller antennas that are even applicable on pocket drones.

Another difference between radar and localization is that in radar applications the radar will only be aware of the fact that there is a target, and potentially be aware of some geometrical properties of the target. In the case of localization UWB transceivers can not only determine range between one another, but can simultaneously exchange data as well [35, 47]. Within the requirements imposed by the performance of the system (such as required update rate) the UWB localization systems are free to exchange other data than the data required for localization [47]. This is essential for what this thesis aims to achieve, since range information

alone is not enough to determine relative locations of other agents in the swarm.

It is for these reasons that this thesis will explore the area of localization rather than the area of radar, despite their apparent similarities.

4-2 Ultra-Wideband for Localization

One of the main problems of ranging and localization using any type of EM waves is that the technique generally suffers from multipath errors. These errors occur due to the fact that the EM waves bounce off of walls, furniture, *etc.*, causing the receiving end to receive the same signal multiple times at different time delays. Traditionally these multipaths are difficult to separate from the direct path, causing erroneous estimation of the range between transmitter and receiver. Fortunately, as demonstrated in chapter 3, UWB's high temporal resolution (caused by the narrow width of an UWB signal in time) naturally provides robustness against the multipath problem.

The advantages of UWB spurred the scientific community to research its potential for localization applications. A lot of research regarding this subject involves the usage of UWB beacons with known positions to aid in the localization of an agent in the environment through a process called triangulation. These types of systems along with how they work are assumed background knowledge throughout this chapter. If terms such as Time of Arrival (TOA), Time Difference of Arrival (TDOA), or Two Way Ranging (TWR) sound unfamiliar, the interested reader is referred to chapter 5 and 6 for an introduction into these concepts and triangulation in general.

4-2-1 Early Research on UWB localization

Some early research done on UWB localization is done by Lee and Scholtz in 2002 [65]. They examine specifically the ranging capabilities of UWB signals in a dense multipath environment. The researchers perform ranging measurements for a variety of scenarios using a Generalized-Maximum Likelihood (GML) estimation algorithm in a TWR scheme to reduce clock offset errors. The easiest scenario that was examined by Lee and Scholtz is one with a clear unobstructed Line-Of-Sight (LOS) between transmitter and receiver, and with a relatively short distance between the two. The researchers report a ranging error of less than 15 cm in this scenario. As the scenarios increase in difficulty the error in TOA estimation goes up, up to about 1.2 meters maximally. One of the interesting aspects that the researchers report is that the error in TOA estimation appears to increase as distance between transmitter and receiver increase. Lee and Scholtz suggest that this could be due to the fact that the LOS blockage becomes more complex as the distance increases.

Correal et al. did early research on UWB localization in an article published in 2003 [22]. Rather than only utilising the information that fixed UWB beacons offer for the purpose of localizing agents in an environment, the researchers suggest also utilizing the measured range between the agents (with unknown positions) themselves. The researchers again use a TWR ranging scheme to obtain range estimates. It is mentioned in the paper that their relative localization scheme achieves Root Mean Square Error (RMSE) of about 3 and 3.6 cm in x and y directions. According to the researchers, the same data using classical multilateration would have resulted in location RMSE of 14 and 9.8 cm in respectively the x and y direction. This suggest a significant improvement in performance when utilizing the data available from relative agent to agent ranging as well. The results are quite accurate, but it should be

noted that the results are obtained using clear LOS measurements.

4-2-2 Research on Highly Accurate UWB Localization

As hardware and software improved, so did the accuracy of the UWB localization systems presented in the literature. Gradually the UWB localization systems became capable of producing millimeter accurate localization results. For example, researchers Zhang et al. reported in 2006 [112] and later in 2008 [69] to have acquired mean localization errors of 1.49, 2.61 in 1D and 2D respectively. In 3D the authors reported an accuracy of 3.32 mm in their article from 2006, and an accuracy of 2.45 mm in their article from 2008.

The researchers combine Received Signal Strength (RSS) methods with first peak detection algorithms. They further use a TDOA method to transform the range measurements into a location of the tracked tag. In their article the agent is transmitting information that is received by receivers at specific reference locations. In order to get the highly accurate results, the receivers are time synchronized amongst themselves. Furthermore, the tag and the receivers have synchronized PRF and local oscillators. The accurate 3D result is obtained by using 6 receiving stations to do the TDOA computation. The researchers show that by having an over determined system (6 receivers instead of 4) the accuracy of the system increases. Particularly for the case of 4 receiving stations with a high Position Dilution of Precision (PDOP) value, the accuracy of the system deteriorates rapidly (a mean error of 43.3 mm is reported in the worst case scenario). This also hints towards the dependency of the accuracy of these localization systems on position, since the PDOP value changes depending on the base station layout and the tag position.

4-2-3 UWB Localization Applied to Indoor Navigation

Whilst some articles focus on the development of accurate UWB localization systems, other articles focus on applying UWB localization systems in real applications. An example of where this can be used is for indoor navigation.

Researchers Krishnan et al. look at this application of UWB systems [60]. The researchers suggest alternatives to an UWB localization system (odometry, IR, or ultrasound based) but note that each of these technologies have problems that make them ill suited for proper indoor robot navigation [60]. Instead they propose an UWB system using receivers in known locations, in combination with centrally processed TDOA computations. The receivers are wired to a central computer in order to virtually mitigate all clock synchronization errors. They keep the cost of the receivers low, and consequently claim that by doing so they can easily use a lot of receivers with minimal costs. They use this to prevent problems associated with Non Line of Sight (NLOS) conditions. By simply making sure there are enough receivers spatially distributed the robot will at all times have LOS with enough receivers to compute its position. Interestingly enough, the central computer communicates with the robot through Zigbee, rather than UWB. The researchers report that this is mainly due to the unavailability of low rate UWB Integrated Circuits (ICs) at the time of writing, but mention that they would consider UWB also for communication when such ICs become available in the future. All together the localization system keeps track of the robot with a Root Mean Squared Error (RMSE) of less than 15 cm, and a maximum error of 25 cm across its trajectory.

4-2-4 UWB Localization for Aerial Vehicle Applications

Most recently a lot of articles have also started to focus on applying UWB localization systems for the use of localizing Aerial Vehicles, which is the most interesting for the research in this thesis work. Localizing aerial vehicles introduces the difficulty of another dimension, namely height. This is often considered a non trivial extension to just 2D position estimation because now beacon based systems must make a trade-off between accuracy in horizontal and vertical localization. The different research found is described below.

Benini et al. investigate combining UWB localization data with other sources of localization data in order to get accurate indoor localization of an Unmanned Aerial Vehicle (UAV). [14] Specifically, it attempts to fuse Inertial Measurement Unit (IMU) data with vision based sensor data and UWB localization data in an EKF. The researchers use a commercially available UWB localization system developed by UbiSense. Benini et al. mention that the UbiSense system has an accuracy of 15 cm with a 95% confidence, which it obtains by using two different localization methods, namely TDOA and Angle of Arrival (AOA) methods. The localization computations are performed off-board. The researchers report that after fusing this data with IMU and vision odometry, the accuracy is increased to 10 cm. This is not a very large improvement yet considering the substantial additional computational complexity of the system.

Researchers Mueller et al. attempt to accomplish a similar task in [77] when they describe and implement an algorithm that fuses UWB localization data with rate gyroscopic and accelerometer data. Mueller et al. do not use the popular TDOA method, but instead use a TWR method to eliminate the clock synchronization errors. This therefore requires both the agent and the reference beacons to be able to receive and transmit messages. Through a variety of experiments (hovering, waypoint following at slow and fast speeds) the researchers examine the localization error of the proposed methods. In horizontal direction the researchers realize reasonable accuracy, namely approximately 5 cm mean error for the hovering experiment. In vertical direction, however, the mean error is much worse, namely approximately 24.4 cm. The researchers attribute this anomaly to the orientation dependent group-delay of an antenna [77].

In the same spirit, Tiemann et al. attempt to design and implement an indoor localization system for UAV navigation using commercially available UWB technology [105]. They use an interesting method of emulating GNSS signals over UWB in order to maximize compatibility of the localization system with many commercially available UAVs that use GNSS. The researchers focus on achieving a high horizontal accuracy (as opposed to vertical accuracy), and therefore also again achieve higher accuracy in the horizontal plane than in the vertical plane. The researchers report a RMSE of less than 10 cm in the horizontal plane with a 95% probability. In the vertical plane, the accuracy is less than 20 cm in the vertical plane with a 95% probability.

Finally, Nguyen et al. also describe an indoor UWB UAV localization system [82]. Apart from the often used EKF, they propose an alternative method for computing localization data, namely using Non-Linear Regression (NLR). The advantage of the NLR is that it does not require data from the previous localization step, like the EKF does, making the NLR more robust in the case of loss of connection for some time. The disadvantage of the filter, however, is that because it computes an entirely new estimate of position every time step, and it converges only to a local optimum, it can happen that from one time

step to the next the computed position are significantly different. This could potentially prove dangerous for the stability of the system. The researchers observe this effect in the estimate of the altitude, which according to them causes the computed altitude to sometimes "flip" at some points. The researchers report a maximum RMSE in horizontal direction of 0.162 m , and a maximum RMSE in vertical direction of 0.353 m with the EKF. For the NLR, the maximum RMS in horizontal direction is 0.144 m , and in vertical direction 0.356 m , which is thus slightly more accurate than the EKF results in the horizontal direction.

The researchers mentioned so far in this section all use a beacon based system to perform localization through lateration. In those systems, there are several UWB beacons present with known coordinates. Whilst this is interesting research, it is different from using UWB as an on-board sensor for localization. One other group of researchers is performing research that is closer in spirit to the intended use of UWB within this thesis. Guo et al. demonstrate in [39] a method of combining self displacement information with UWB ranging to perform relative localization. They do, however, have an initialization phase that requires a static drone that essentially performs the function of a beacon. They derive the methodology required to be able to fly with all the drones simultaneously after the initialization phase, but they do not show this experimentally. In their experiments in [39] they keep the static beacon stationary throughout the experiment. A relative localization error within 1 meter is achieved in their experiment with inter-UAV distances of up to 30 meters.

4-3 Ultra-Wideband as a Communication Technology

UWB is also a capable communication technology. However, as mentioned in chapter 3, UWB did not take off as a communication technology as rapidly as was initially expected. This is also reflected in the literature when looking for practical uses of UWB as a communication technology. It should be noted that technically any UWB system used for localization is also an UWB system capable of communicating, since all of the EM based localization principles rest on the fact that information is communicated between devices. The difference in this consideration is that for the purpose of localization the focus is on getting low localization errors (which means accurate timestamps on the signals). For the purpose of communication the focus is on getting high data rates, with accurate timestamps of messages being of minimal importance.

One of the few mentions of developed UWB communication systems was done in [35] by Fontana, where the existence of three UWB communication devices is mentioned, named DRACO, ORION, and AWICS. According to Fontana, DRACO uses Frequency-Division Multiplex (FDM) in combination with Time-Division Multiple Access (TDMA) to allow communication with multiple users simultaneously over several kilometers of range. ORION is a system that uses a fixed TDMA architecture that allows long communication ranges of up to 60 km [35]. Finally, Fontana mentions AWICS, a system that again uses the TDMA architecture and which is designed for use in high multipath environments. However, according to Fontana the ORION system was designed for the military (infantry and platoon operations) and the AWICS system for the navy, thus neither of those systems are for commercial or research purposes.

One good example of research performed on creating a UWB communication system is presented by Kikkawa et al. in [54]. The researchers designed an UWB transmitter with

integrated antennas for the purpose of high speed communication over UWB. The researchers present a chip that is only a few millimeters in width and height. This is partially possible because of the fact that the high frequency that was aimed for in the design (3.5 GHz center frequency) allows for relatively small antenna lengths [54]. Using a Gaußion Monocycle Pulse as the UWB signal of the choice, the researchers report being able to attain transmission speeds of 1.16 Gb/s with the small UWB transmitter. The article is however dedicated to the design of an UWB pulse transmitter, rather than showing its use in a practical application.

Most research that is in one way or another related to UWB communication is dedicated to only parts of an UWB communication system, such as considerations regarding the signal design for UWB communications in [92] or the design of a suitable antenna in [66]. Perhaps in the further future UWB will take off as a communication technology as demand for high speed wireless data exchange increases, but to date only few examples exist.

Chapter 5

Beacon Based Localization and Ranging

This chapter gives an introduction into beacon based Electromagnetic (EM) wave based localization methods. These methods are essentially the alternative, more widely used way to use wireless signals for localization purposes, compared to how this thesis uses wireless signals for the purpose of localization. They rely on static beacons in the environment with respect to which an agent (referred to as a “tag”) can localize itself. These methods of localization often go hand in hand with the process of ranging as well, which is why these topics are treated simultaneously in this chapter. However, the specific ranging method called two-way ranging is discussed separately in chapter 6 due to its relevance to this thesis.

Beacon based navigation uses the concept of triangulation, which means that the geometric properties of triangles are used in the determination of position [67]. Beacon based localization can be further divided into lateration and angulation methods. Lateration methods determine an agent’s position by measuring the relative distance between an agent and several reference points. Angulation methods uses the angles between an agent and several reference points to deduce a location. The lateration techniques are discussed in section 5-1, and angulation is described in section 5-2. Finally, the direction in which information is shared between beacons and tags is further explored in section 5-3.

5-1 Lateration Techniques for Localization

The first discussed lateration method uses information of the Time of Arrival (TOA) of an EM wave at a tag. TOA methods are based on the fact that knowing the departure and arrival time of an EM wave allows one to deduce the distance it traveled. A tag can determine its range to a beacon using the equation $R = c(t_R - t_S)$. In this equation R is the computed range, c is the speed at which an EM wave propagates, and t_R and t_S are respectively the time at which a tag receives a message from a beacon, and the time at which the beacon sent that message.

Knowing the range to multiple beacons in space allows a tag to solve a set of equations to deduce its own location. In two dimensions (2D) a tag needs a minimum of three range

measurements to beacons to unambiguously solve for its location, and in three dimensions (3D) a tag needs a minimum of four range measurements to beacons. Some methods however can reduce the number of required beacons by one beacon for part of the operation, such as done by Radovnikovich et al. in [89], by cleverly using information from previous range measurements (in this case by deducing a tag's velocity) in order to resolve the location ambiguity. However, to get an initial fix on a tag, still three range measurements are necessary in 2D and four in 3D.

Intuitively this can be understood by geometrically visualizing the situation. For reference the situation is schematically depicted in figure 5-1 for the 2D case. In 2D, knowing your range towards a beacon (denoted by R_1) means that you can be located anywhere on a circle of radius R_1 around the beacon. By measuring at the same time your range towards a second beacon (R_2), you know now that you are also located somewhere on the circle of radius R_2 from the second beacon. The intersection of these two circles in space gives you the possible locations where you could be located in space. If the two beacons are not spatially identical, this gives you 2 (or in a rare case 1) possible locations where you could be located. By measuring the range to a third spatially different beacon, one can unambiguously determine their location at the intersection of the three circles. This is why a minimum of three intersections are needed to unambiguously solve for a position in 2D space. A similar reasoning can be extrapolated to determining one's position in 3D and why it requires a minimum of 4 range measurements.

In 3D, the equation for the range towards a beacon can be expressed as follows:

$$R = \sqrt{(x - x_R)^2 + (y - y_R)^2 + (z - z_R)^2} \quad (5-1)$$

Where R is the (measured) range to a certain beacon, (x_R, y_R, z_R) are the known Euclidean coordinates of the beacon in 3D space, and (x, y, z) are the unknown Euclidean coordinates of the tag in 3D space. In order to unambiguously solve for the tag's coordinates in 3D space, equation 5-1 must be simultaneously solved for 4 (independent) range measurements to 4 different beacons.

The considerations presented above work perfectly under the assumption that the location of the beacons in space are perfectly known, and that the range to these beacons is measured without error. In reality such conditions are never true. This means that in 2D, rather than being located precisely on a circle around a beacon, a tag will be located anywhere on an annulus around the beacon (with a width proportionate to the uncertainty in the range measurement). The intersections of multiple of these annuli will geometrically not result in a single point, but rather an area where the tag can be located on. This means that it won't be possible to exactly solve equation 5-1. Furthermore, this means that the estimation of a tag's position is going to be less accurate.

In order to combat some of these problems, other methods of solving equation 5-1 exist. A number of these methods involve the construction of a cost function. This cost function allows adding more than the minimum amount of range measurements to beacons in order to improve the localization accuracy. Such a cost function will look similar to:

$$\mathbf{F}(\mathbf{x}) = \sum_{i=1}^N \alpha_i (R_i - \sqrt{(x - x_i)^2 + (y - y_i)^2 + (z - z_i)^2}) \quad (5-2)$$

where α_i is a weighing factor that can be chosen to for example represent the strength of a

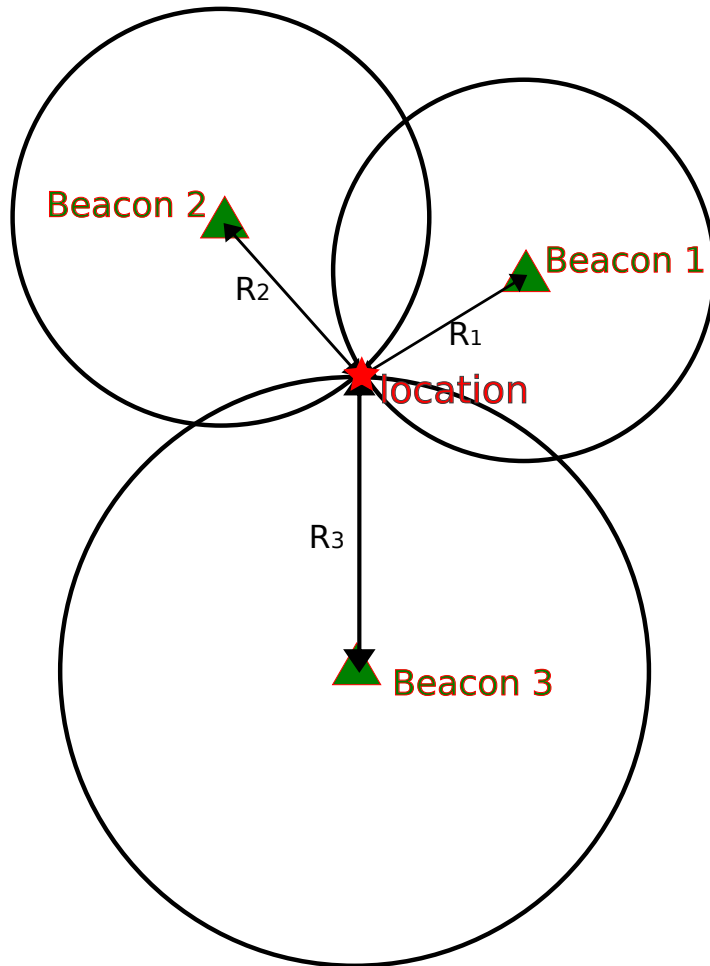


Figure 5-1: Schematic depiction of 2D trilateration process

measurement's signal, N is the number of beacons used in the computation, i is the counter for the beacons, R_i is the measured range (through TOA determination) to each beacon i , (x_i, y_i, z_i) are the Euclidean coordinates of each beacon i and $\mathbf{x} = (x, y, z)$ are the Euclidean coordinates of a tag that are to be estimated.

A variety of methods can be used to minimize the cost function as defined by equation 5-2, which will result in an estimate of the tag's coordinates. Note that the cost function is non-linear, such that a non-linear optimizer should be used to minimize the cost function. These optimizers typically run the risk of converging to local optima, so they often require a decent initial guess of the tag's coordinates to converge to the global optimal solution of the tag's coordinates.

One of the main problems in using TOA techniques is that the clock time of the receiver and the clock time of the transmitter must be precisely synchronized. Due to the high speed at which EM waves propagate, an error in clock synchronization of only 1 nanosecond results in almost 30 centimeters error in range. Especially when the tracked tag is equipped with an inexpensive and inaccurate clock, time synchronization can be a troublesome procedure and result in inaccuracies rapidly.

An alternative to the TOA method is the Time Difference of Arrival (TDOA) method. Similarly to TOA techniques, TDOA also uses EM wave propagation times to deduce locations. However, unlike TOA, TDOA uses differences of propagation times between signals received from distinct beacons, rather than raw the propagation times.

Much like the TOA method, the TDOA method also has a geometric interpretation. Measuring the range difference between two beacons gives the receiver enough information to determine that it must lie on a hyperboloid of constant range difference between the two beacons. This is schematically depicted in figure 5-2.

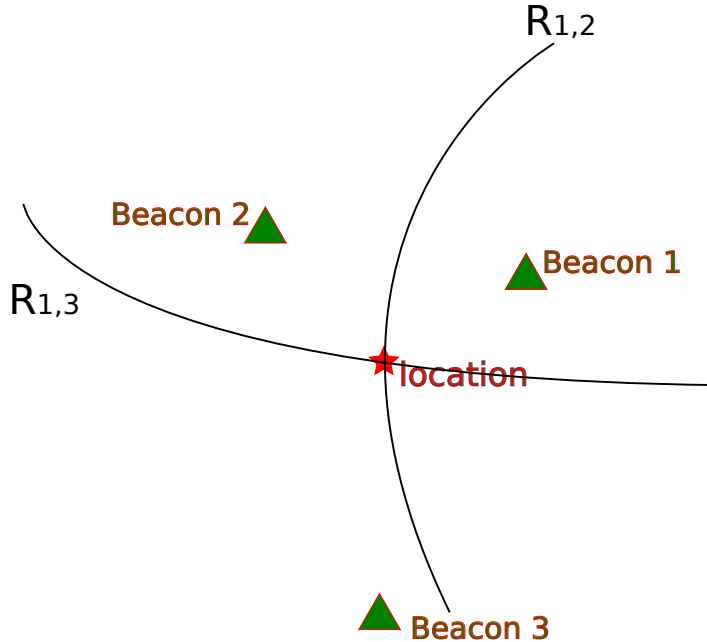


Figure 5-2: Schematic depiction of 2D TDOA process

Just like the equation of a circle was used in the TOA case, the equation of a hyperboloid is used in the TDOA case:

$$R_{i,j} = \sqrt{(x - x_i)^2 + (y - y_i)^2 + (z - z_i)^2} - \sqrt{(x - x_j)^2 + (y - y_j)^2 + (z - z_j)^2} \quad (5-3)$$

In this equation (x_i, y_i, z_i) and (x_j, y_j, z_j) represent the known coordinates of transmitter i and j , (x, y, z) are again the unknown coordinates of the receiver, and $R_{i,j}$ is now the difference between the range from the receiver to transmitter i , and the range from the receiver to transmitter j .

Somewhat simplistically put, the range $R_{i,j}$ can be calculated as

$$R_{i,j} = c((t_{R,i} - t_{S,i}) - (t_{R,j} - t_{S,j})) \quad (5-4)$$

where $t_{R,i}$ and $t_{R,j}$ are respectively the times at which the tag received a signal from beacons i and j , and $t_{S,i}$ and $t_{S,j}$ are respectively the times at which the beacons i and j transmitted that signal.

If it is assumed that the beacons have synchronized time clocks, and send their signal at the same time, then $t_{S,i}$ and $t_{S,j}$ are equal, and will cancel out in equation 5-4. This will

consequently mean that equation 5-4 depends only on the received signal times, which are measured both by the same receiver clock. This essentially eliminates the need for time synchronization between the beacons and the tag. This is advantageous when the beacons are for example fixed, and perhaps even wired together. In this case it is much easier and more accurate to synchronize the beacons, than it would be to synchronize tag and beacon.

In order to estimate a 2D location, a minimum of two TDOA measurements are needed to find a location, instead of the minimum three TOA measurements. This is because the intersection of two hyperboloids already gives an unambiguous intersection point. However, since two beacons are needed for every TDOA measurement, still a minimum of three beacons are needed to find a solution (provided one of the transmitters is used in two different TDOA measurements). Just like for the TOA case, it is again possible to add more measurements in combination with some optimization method to increase the localization accuracy.

A third lateration method is called Roundtrip Time-Of-Flight in [67] or Two-Way Ranging (TWR) in some other articles [55, 62, 63]. TWR is very similar to the TOA method, with the exception of how the EM wave propagation time is determined. In pure TOA methods the tag and beacon must have synchronized clocks. The transmitter then sends a signal containing a time stamp of when the signal was sent, such that the receiver can deduce from the time stamp and the received time what the propagation time (and thus distance to target) was. TWR, however, has two way communication between transmitter and receiver. If this technique is used in the proper way, then there is no need for synchronization between transmitter and receiver to deduce range. For this reason, TWR has the potential to be simpler and more precise than simple TOA ranging, but comes at the expense of a higher channel usage per ranging request [105]. Once the range between the tag and some beacons is determined, the same lateration principles as used for the TOA case can be used.

TWR knows quite a few different implementations, each with their own considerations and advantages. Because of the particular relevance of TWR to this thesis, it is treated separately in chapter 6.

The fourth lateration method discussed here is the method of Received Signal Strength (RSS) or Received Signal Strength Indicator (RSSI). This method directly uses the strength of a received signal to estimate a range between tag and beacon, instead of using the information the signal contains. If $r(t)$ is the signal received by a receiver antenna, the RSS is given by [41]:

$$RSS = \int_{-\infty}^{+\infty} |r(t)|^2 dt \quad (5-5)$$

The measured strength of the received signal needs to be mapped into a distance, so distance d is a function of the RSS, expressed as $d = f(RSS)$. The difficulty in RSS based localization is finding out the mapping $f : RSS \mapsto d$. There are a variety of approaches to do this, both theoretical as well as experimental [67].

The theoretical models typically try to model the strength of a signal in relation to the distance between tag and beacon, in order to be able to directly map the RSS value to a distance value. The downside of this is that especially in indoor environments these models are almost never accurate enough because the constants used in the theoretical models often change depending on the indoor environment, and because shadow fading is too unpredictable

in the indoor environment [41].

For indoor localization using RSS methods that leaves mostly the empirical methods. These methods require a priori information on the RSS values that will be measured in different parts of an indoor environment. A database of this information must be collected, which is called location fingerprinting. With the known database in place, the actual RSS values that a tag measures with respect to multiple beacons must be compared to the values present in the database in order to extract position information. Many algorithms of vastly ranging complexities exist for specifically this task, such as nearest neighbour algorithms or bayesian statistics based methods. An indepth approach to RSS based localization using statistical location fingerprinting is given in [51]. These methods require a lot of location-specific knowledge, and therefore cannot quickly be employed in a new location without performing all the measurements for the database again.

The RSS method is very different from the other lateration methods discussed so far, and therefore has its own unique advantages compared to the other methods discussed so far. The main advantage of the RSS method is that it does not need any time clock synchronization at all, neither between tag and beacon (as with TOA), nor between the beacons themselves (as with TDOA). In fact, because it does not use any time clock in the ranging scheme directly, it does not contain any clock drift errors whatsoever (which TWR does still suffer from). Another advantage of RSS methods is that the performance of RSS methods is not significantly affected by the bandwidth of the used signal [5], or the occurance of possible undetected direct paths in the signal [41]. This is a big advantage from a practical point of view, because it means that that many existing wireless networks, such as the existing wifi networks present in many buildings, can be used for RSS ranging, without imposing additional bandwidth or network architecture requirements on these networks.

The final lateration method that can be employed is the Received Signal Phase (RSP) method. In RSP, the tag measures the received phase of a signal arriving from a beacon, and uses that information to determine distance towards that beacon. This method is again very similar to the TOA method, except that it does not map a signal delay into a distance metric, but instead maps a signal phase shift into a distance metric. Because of the similarities, the same algorithms can be used as those explained in the paragraphs on TOA methods to translate the distances to several beacons into a location in space.

5-2 Angulation Technique for Localization

Apart from lateration method, there is also a group of localization methods that are referred to as angulation techniques in [67], or Angle Of Arrival (AOA) techniques. These methods do not make use of distance information, but instead use the angle at which a tag receives an EM wave from a beacon to perform localization. In 2D, a single AOA measurement from a beacon geometrically means that the tag is anywhere on a line going from the beacon to the tag. This is schematically depicted in figure 5-3, where the angles to the reference beacons are α_1 and α_2 . The intersection of two of these lines already give the tag's position.

Of course the situation is somewhat simplified here by assuming the AOA can simply be determined. In reality retrieving the angle of an arriving EM wave is more complex than retrieving the distance to the transmitter of the EM wave. There are however methods that

can accomplish this, and these systems are also being used in practice. An example system used by aircraft is the Very high frequency Omnidirectional Radio (VOR) range beacon. In this system the transmitter is responsible for encoding the angle information into its signal. By having a circular array of transmitting antennas, a VOR beacon uses the Doppler effect to encode the angle into the signal. Depending on the bearing that an observer has with respect to the VOR beacon, a different phase of the transmitted signal will be received. By comparing the phase with a certain baseline signal that the VOR beacon also transmits, the observer can extract a bearing. For example, a zero phase shift indicates being North of the VOR beacon, a 90° phase shift indicates East, etc.

A method that might be more applicable to smaller drones is using two spatially dislocated receivers that receive the same signal. One can compare the phase between the two signals to extract a bearing (up to a flip ambiguity).

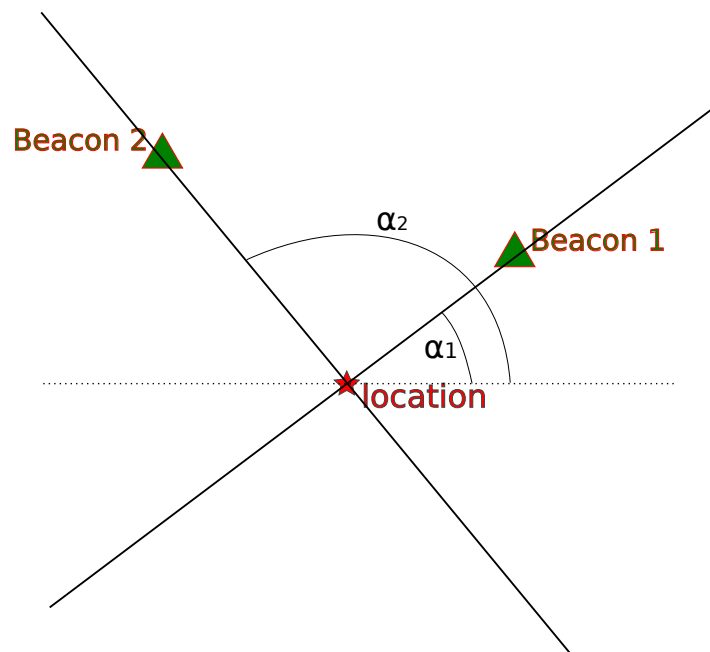


Figure 5-3: Schematic depiction of 2D angulation process

An obvious advantage of angulation techniques over lateration techniques is that it requires one less beacon to determine a tag's position (two are needed in 2D and three in 3D) [5]. The disadvantage of the method is that the error in localization increases proportionally to the distance from the beacons [93], making this method most suitable for short ranges. In comparison, the lateration methods are theoretically independent of distance (although also the lateration methods typically have some error dependency on the range [50, 65], because the propagation channel of the EM waves become more complex for larger distances [65]). Another disadvantage of angulation is that, as mentioned, measuring the AOA is more difficult than measuring just the distance, which makes the dependency of the method on antenna geometry bigger, potentially leading to more complex and heavy antennas [67] [4].

5-3 Uplink, Downlink, and Hybrid Localization

All of the ranging and/or localization methods described in sections 5-1 and 5-2 require communication between tag and beacon. So far it has mostly been assumed for the sake of clarity that it is the beacon that is sending information, and the tag that is receiving information. It is however also possible that the direction of information is reversed, such that the tag is the one transmitting a signal, and the beacon is receiving this signal. The direction in which information flows determines whether an architecture is a downlink, uplink, or hybrid localization system.

An example of a strict downlink localization system is the well known GPS [47]. In the case of downlink systems, the beacons (or satellites in the case of GPS) with known coordinates are strictly transmitters. the tag that wishes to deduce its location is in this case the receiver. The transmitters provide information to the tag in a downlink fashion, and they do not receive any information back. The transmitters thereby only provide information, but no service [47]. It is the task of the tag to perform computations in order to deduce its own location (through lateration or angulation methods). The advantage of such a system is that it is theoretically scalable to serve an infinite amount of users [47], because any number of a tags can receive the signals from the transmitters and deduce their location as long as the signal is strong enough to be received. The disadvantage of such an architecture is that it imposes additional requirements on the receiving a tags, because they must be capable of doing the computations required to solve for their position.

The alternative is a strict uplink localization system. In this case the beacons are the receivers, and the tag is the transmitter. Depending on the method, the tag will transmit a certain message. Multiple beacons in this case will receive the signal from the tag, and by combining the received signals in a central computer, the central computer can deduce the tag's position. In this case, of course, it is the central system that is aware of the tag's location, but the tag is still unaware of its own location. In some cases this is exactly as desired, since some applications require only the system to be aware of a tag's position, without requiring the tag to be aware of its own position. However, when the tag must also know its own position, its location should separately be communicated to the tag [91]. The advantage of this is that the tag no longer has to perform lateration computations anymore, this is instead done by the central computer. The disadvantage is that the capacity of the system is limited, because it requires communication from every tag, and because the central system must perform the computations for all the tags.

Finally it is recognized that some systems are best classified as hybrid uplink/downlink systems. An example of these systems is those that use the TWR scheme to perform ranging. In this case both the tag and the beacons must be capable of sending and receiving information to accomplish the TWR scheme. Depending on the situation, both the tag and a central system could perform the lateration computations to determine the location of the tag. As mentioned, the advantage of this type of setup is that it eliminates the need for time synchronization between a tag and beacons. The disadvantage is again the limited capacity of such a system to serve many users.

Chapter 6

Two-Way Ranging Implementations and Considerations

Two-way ranging (TWR) methods are very suitable for use in combination with UWB to establish range information between drones. This is due to the fact that some TWR algorithms focus on the suppression of ranging errors due to clock crystal drift [63], an important property when considering that most drones won't be equipped with heavy and/or expensive clocks with low clock drift. As the name suggests, TWR indeed requires both devices participating in the ranging procedure to participate in sending and receiving information. This means that both devices (device A and device B) must be equipped with transceivers to provide this functionality.

The communication required between two devices (device A and B) for the basic TWR algorithm is schematically depicted in figure 6-1.

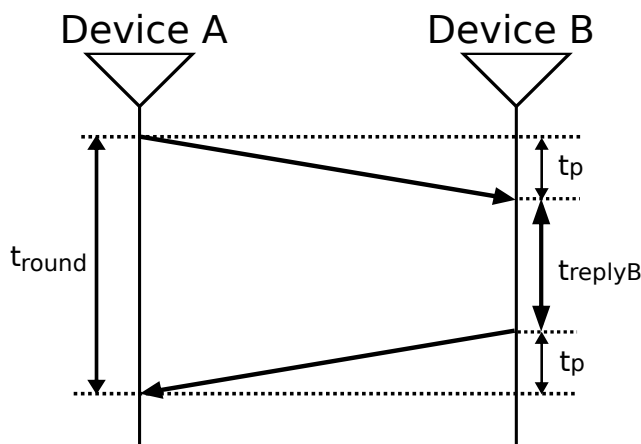


Figure 6-1: Schematic depiction of the basic TWR algorithm

In figure 6-1, t_{round} is the complete round trip time, t_{replyB} is the time that device B waits after receiving a message from device A before sending a reply message, and t_p is the actual

propagation time of the signal, which is the variable of interest. Under the assumption of a perfect clock, equation 6-1 holds.

$$t_{round} = 2 \cdot t_p + t_{replyB} \quad (6-1)$$

This equation can be rewritten to extract the parameter of interest, namely the propagation time t_p , which is expressed by equation 6-2.

$$t_p = \frac{1}{2} (t_{round} - t_{replyB}) \quad (6-2)$$

In reality, however, both device A and device B will have an imperfect clock that drifts over time. Consequently, t_{round} , which is measured by device A will be slightly inaccurate, and t_{replyB} , which is measured by device B, will also be slightly inaccurate. This can be expressed by introducing the clock errors e_A and e_B of device A and device B respectively. Introducing these factors into equation 6-2 results in equation 6-3, where \hat{t}_p is the estimate of the propagation time, which is affected by the clock errors.

$$\hat{t}_p = \frac{1}{2} (t_{round}(1 + e_A) - t_{replyB}(1 + e_B)) \quad (6-3)$$

By subtracting equation 6-2 from equation 6-3, and by substituting equation 6-1 for t_{round} , the following expression is found for the difference between the estimated and the real propagation time:

$$\hat{t}_p - t_p = t_p \cdot e_A + \frac{1}{2} t_{replyB} (e_A - e_B) \quad (6-4)$$

It is typically assumed that $t_{replyB} \gg t_p$, such that the main contribution in the ranging error comes from the reply time at device B.

The dependency of the ranging error in the basic TWR method on the reply time caused interest in the development of algorithms that are more robust against clock drift. Most of the improved algorithms take the form of Double Sided Two Way Ranging (DS-TWR) algorithms. This family of methods started when Rainer Hach proposed a Symmetric Double Sided Two Way Ranging (SDS-TWR) algorithm to the IEEE ranging subcommittee in 2005 [40]. The SDS-TWR algorithm is schematically depicted in figure 6-2.

It is shown in [62] that with this TWR scheme the time of flight can be calculated according to:

$$t_p = \frac{1}{4} ((t_{roundA} - t_{replyA}) + (t_{roundB} - t_{replyB})) \quad (6-5)$$

Using this calculation method, the corresponding error equation becomes:

$$\hat{t}_p - t_p = \frac{1}{2} t_p (e_A + e_B) + \frac{1}{4} ((t_{replyB} - t_{replyA})(e_A - e_B)) \quad (6-6)$$

At this point the constraint of the SDS-TWR scheme on the reply times tells us that t_{replyA} is equal to t_{replyB} , in which case the second term in equation 6-6 would drop out. In that case, it is clear when comparing equation 6-6 to equation 6-4 that the error in the propagation time is no longer dependent on the reply times. It is now only dependent on the propagation time of the signal, which is typically much smaller than the reply time of the devices.

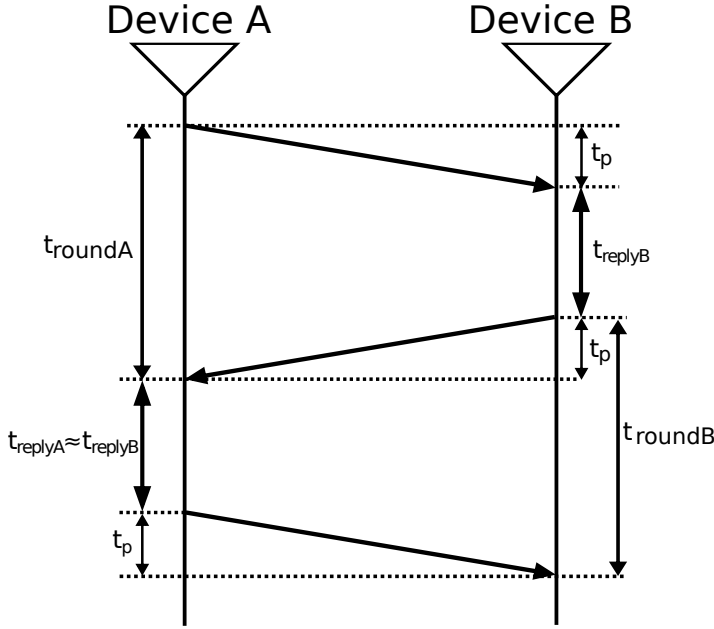


Figure 6-2: Schematic depiction of the SDS-TWR algorithm, adapted from [81]

Unfortunately, the assumption of equal reply times between devices A and B does not always hold, or is otherwise impractical from an operational point of view. It would be much more convenient if both sides were free to choose a reply time. It is shown by Neirynck et al. in [81] that this can actually be accomplished with exactly the same messages as for the SDS-TWR scheme shown in figure 6-2, only now without imposing any requirements on the reply times of the two devices. This method is therefore simply called Double Sided TWR (DS-TWR) since no symmetry properties are used.

The only change that needs to be made for DS-TWR to work is that rather than using equation 6-5 to compute the time of flight, one of the following expressions should be used:

$$\begin{aligned}
 t_p &= \frac{t_{roundA}t_{roundB} - t_{replyA}t_{replyB}}{2(t_{roundA} + t_{replyA})} \\
 &= \frac{t_{roundA}t_{roundB} - t_{replyA}t_{replyB}}{2(t_{roundB} + t_{replyB})} \\
 &= \frac{t_{roundA}t_{roundB} - t_{replyA}t_{replyB}}{t_{roundA} + t_{replyA} + t_{roundB} + t_{replyB}}
 \end{aligned} \tag{6-7}$$

It is shown in [81] that when using either the first or the second expression to calculate the TOF, the error equation reduces to:

$$\hat{t}_p - t_p = e_a t_p \tag{6-8}$$

For the first equation, and to:

$$\hat{t}_p - t_p = e_b t_p \tag{6-9}$$

For the second equation.

These error equations are independent of the reply times of either device A or device B, regardless of whether these reply times are equal or not, which is a big advantage. The disadvantage of this method is that it relies on several multiplications and divisions to compute the TOF. These might be expensive operations on some microprocessors, increasing the computation time required to run this algorithm. This is however considered a small cost to pay for favorable algorithm properties, which is why this specific TWR algorithm is used within this thesis.

There are however yet other implementations of TWR with each their own unique properties. Kwak and Chong suggest in [62] a potentially even better TWR algorithm, which they call Double Two-way Ranging (D-TWR). Their proposed algorithm is schematically depicted in figure 6-3.

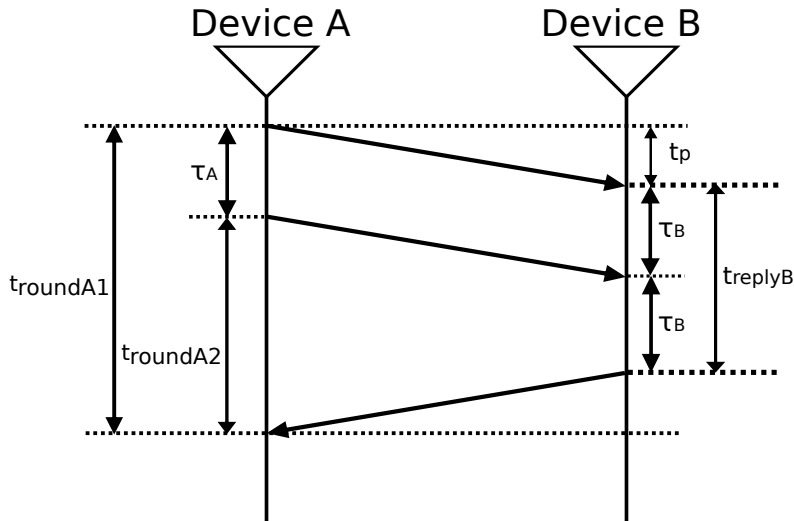


Figure 6-3: Schematic depiction of the D-TWR algorithm, adapted from [62]

Using this communication scheme, it is shown in [62] that the TOF can be computed using:

$$t_p = t_{roundA2} - \frac{1}{2}t_{roundA1} \quad (6-10)$$

With this method the error equation becomes [62]:

$$\hat{t}_p - t_p = t_p \cdot e_A \quad (6-11)$$

Which is the same as the error obtained by using the method presented by Neirynck et al. [81].

Baba and Matia further expand on the concept of sending multiple request messages at once in [7], where they introduce a method that they call Burst Mode Symmetric Double Sided Two Way Ranging (BM-SDS-TWR). This method uses even more than two consecutive request packages at once, in fact it leaves the amount of consecutive request packages variable, so n request messages at once. The schematic depiction of the BM-SDS-TWR algorithm is given in figure 6-4.

For this algorithm, they derive the following range error equation:

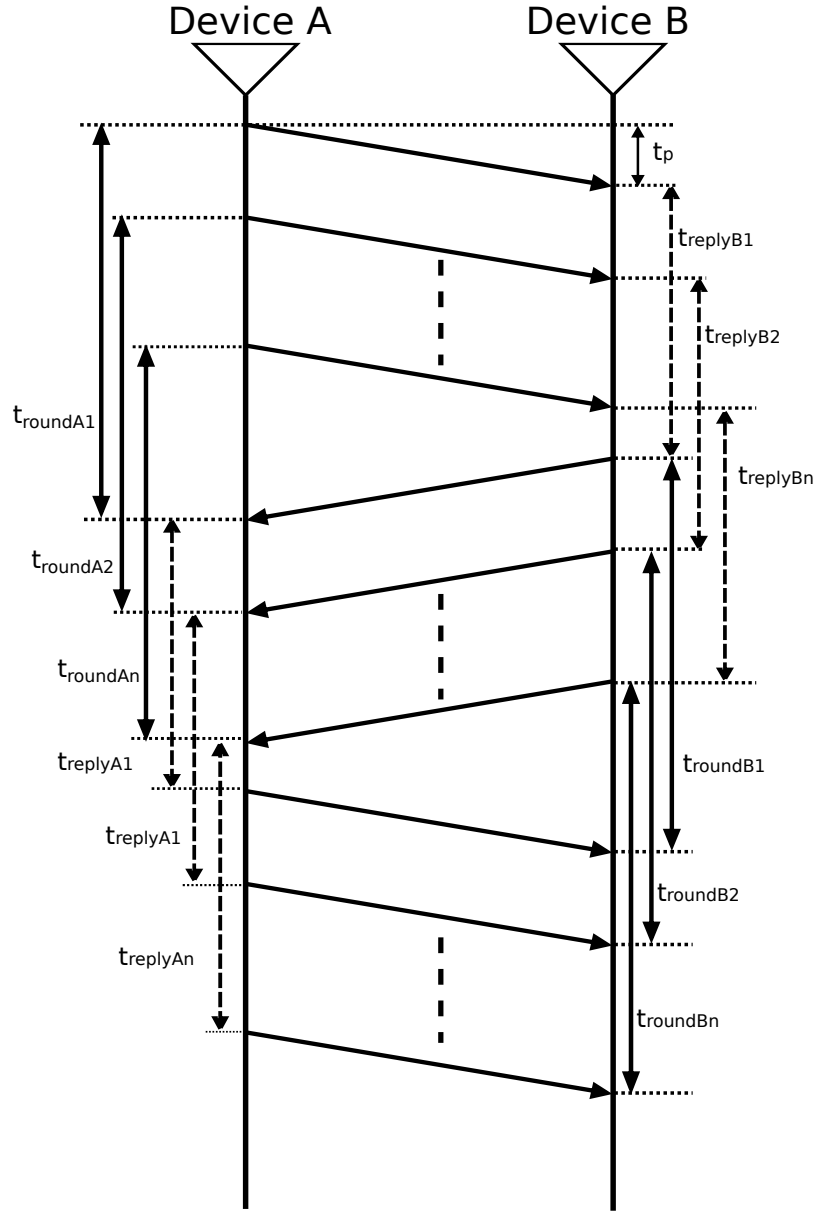


Figure 6-4: Schematic depiction of the BM-SDS-TWR algorithm, adapted from [7]

$$\hat{t}_p - t_p = \frac{1}{4n} \sum_{i=1}^n \{2(e_A + e_B) \cdot t_p + (e_A - e_B)(T_{replyB_i} - T_{replyA_i})\} + \Delta R \quad (6-12)$$

where in this case ΔR indicates the clock resolution error, which was not considered in the previous discussions, and i is the counter for the messages being sent.

Notice how for a single request message being sent at a time, thus for n equal to 1, and without considering the clock resolution error, equation 6-12 reduces to equation 6-6, which is exactly as expected, given that the BM-SDS-TWR algorithm is just an extension to the SDS-TWR algorithm where multiple messages are sent consecutively. Just like for the SDS-TWR

algorithm, if the reply times of device A and B are the same for every request message i , the range error becomes only dependent on the propagation time of the signal, which is typically very small. The authors show in [7] that in fact this formulation of the algorithm causes the error to decrease as n increases.

At first sight it seems that increasing the number of messages n will also have an adverse effect, namely that it will take longer to get a single ranging measurement. However, Kim illustrates in [55] that this is not necessarily the case. This becomes apparent when considering the implementation of these algorithms in a real ranging system. Sometimes it might be necessary in reality to iterate the ranging algorithms multiple times in order to get a stable ranging result. [55] Whilst it is necessary in the case of SDS-TWR to repeat the entire ranging procedure when an iteration of the ranging algorithm is performed, the BM-SDS-TWR algorithm can achieve such an iteration by simply adding another message to the sequence. This means that especially in the case where many iterations of the algorithm are necessary to get a stable ranging result (such as in the case of severe signal interference) the BM-SDS-TWR actually uses less messages to get the stable ranging result, thus has the potential to reduce ranging time.

In this thesis, it has been decided to use DS-TWR, represented by equation 6-7 as the TWR method of choice. This choice has been made due to the favorable properties of an asymmetrical TWR algorithm. Especially when more than two devices are involved in the ranging algorithm, the asymmetrical properties can be exploited to efficiently range with multiple modules, without having to worry about keeping equal reply times.

Part III

Additional Experiments

Chapter 7

Ranging Experiments with Ultra Wideband

It is important to verify the ranging performance of the UWB modules used in this thesis. For this purpose an experiment was conducted, which will be described in this chapter.

7-1 Hardware Used in Ranging Experiment

The first thing that was needed for this experiment were a pair of UWB transceivers. For this thesis it was decided to use the DWM1000 UWB module by Decawave.¹ These modules were chosen for a number of reasons. First and foremost is the fact that these modules are relatively easy to use. The DWM1000 module is a package that already has an integrated circuit, UWB antenna, power management, and clock control in a single product. This therefore allows transferring some of the low level details of managing complex UWB interactions to the module, but it still allows for a good amount of customization options. A second reason is the fact that the DWM1000 is designed for real time localization applications in mind, which corresponds with the primary use case that this thesis explores.

Decawave themselves report that the DWM1000 is capable of locating objects to a precision of 10 centimeters indoors [25]. They are not very precise however as to how this value is obtained and what kind of error representation is used. For this reason it was necessary to also perform tests on the chips to find out what the real precision is, starting with the pure ranging performance of the modules.

The decawave module still needs to be controlled by an external controller that programs its registers, sends it commands, and interprets its data outputs. This function was performed by an Arduino Pro Mini 3.3V with an ATmega328 microcontroller running at 8 MHz. In order to connect the Arduino's with the DWM1000 modules, specialized breakout boards were purchased that are specifically designed to connect an Arduino Pro Mini with a DWM1000.^{2,3}

The code used to control the Decawave is adapted from an open source arduino library that

¹<https://www.decawave.com/products/dwm1000-module>

²<https://www.localino.net/>

³<https://sites.google.com/site/wayneholder/uwb-ranging-with-the-decawave-dwm1000---part-ii>

is written to control the DWM1000 with an arduino.⁴ It already contains build in functions that configure the DWM1000 by programming its registers, and contains examples on how to perform ranging measurements with the library.

7-2 Antenna Delay Calibration

One important parameter that the DWM1000 internally takes into account is the antenna delay. In order to precisely determine the time of flight, it is necessary that only the time that the Electromagnetic (EM) wave travels through the air is recorded. Unfortunately there is a delay between when the DWM1000 commands a signal to be sent, and when the signal finally leaves the antenna and propagates through the air. This delay is called the antenna delay. Since the antenna delay would cause erroneous calculations of the time of flight, the DWM1000 internally takes it into account. When the DWM1000 sends a message, the antenna delay is added to the recorded timestamp to represent the actual time at which the EM wave left the antenna. When the DWM1000 receives a message, the antenna delay is subtracted from the timestamp to represent the actual time at which the EM wave arrived at the antenna.

Unfortunately these antenna delays are not the same for different antennas. The effect of this different antenna delay is non-negligible, because an error in the antenna delay as small as 1 nanosecond corresponds with a ranging error of approximately 30 cm due to the fact that it scales with the speed of EM waves. For this reason this antenna delay value must be calibrated.

In the experiments the antenna delay value was calibrated at a distance of 1 meter. A pair of DWM1000 modules were placed carefully at 1 meter distance, and ranging measurements were collected over a period of time. The mean range that the TWR protocol determined was compared to the true value of 1 meter. The error was calculated, and the correct antenna delay was computed by calculating how much the antenna delay must be changed to correct for the determined error. Figure 7-1 shows the calibration procedure being executed.

It should be noted that Decawave recommends a calibration distance of 5 meters for the DWM1000 modules with the settings that were used during the experiment. This distance is likely chosen as it represents an intermediate position between short range and long range measurements, and calibration at such a distance would intuitively result on average in better performance over a larger set of distances. A calibration distance of 1 meter was instead chosen for practical reasons, due to the fact that calibration was easier with both DWM1000 modules hooked up to a laptop. The experimental results presented in section 7-4-2 later on show that the effect of this decision is rather small. The reason for this is that the error changes depending on distance and orientation of the antenna. It will therefore be difficult to get a consistent value for the antenna delay regardless of the distance at which the calibration has taken place. Perhaps a better future alternative would be to collect range data over a variety of distances, and optimizing the antenna delay to get a minimum error over all those distances.

⁴<https://github.com/thotro/arduino-dw1000>



Figure 7-1: Calibrating antenna delays for two UWB modules at 1 meter distance

7-3 Experiment Execution

The idea behind the experiment is to put the UWB modules at a known distance from each other, and to subsequently instruct the UWB modules to perform range measurements between themselves over a 30 second time frame. By choosing a sufficiently long time interval, a large number of ranging samples can be collected. This will allow statistical analyses to be performed on the ranging measurements. Because the true distance between the UWB modules is known, the range determined by the UWB modules can be compared to the true range between them.

The UWB modules were mounted onto a tripod as is depicted in figure 7-2a. There are several reasons for using a tripod. First of all the tripod made sure that the UWB modules were lifted off the ground. This is beneficial because the antennas might behave differently close to the ground due to reflections that can occur from the ground. The lifted position more closely represents the eventual scenario where the UWB modules are attached to drones.

Another reason for attaching the UWB modules to a tripod is that this allowed the UWB modules to be fixed in a certain position during the test. This will make sure that the range measurements are only minimally influenced by the UWB antenna being perturbed and allowed for a constant orientation of the two antennas with respect to each other.

The ranging experiment was conducted in a MCS environment. Within this MCS environment it is possible to determine the location and orientation of objects with millimeter and sub-degree accuracy. This is made possible by an overhead system of IR cameras. By attaching reflective markers onto objects of interest, these IR cameras are able to keep track of specific objects. The different measurements of the same object by multiple cameras allow accurate determination of the location and orientation of the object.

The actual range experiment was conducted for measurement ranges of 50, 100, 150, 250, 500, and 750 centimeters. These measurement distances were marked on the ground with tape

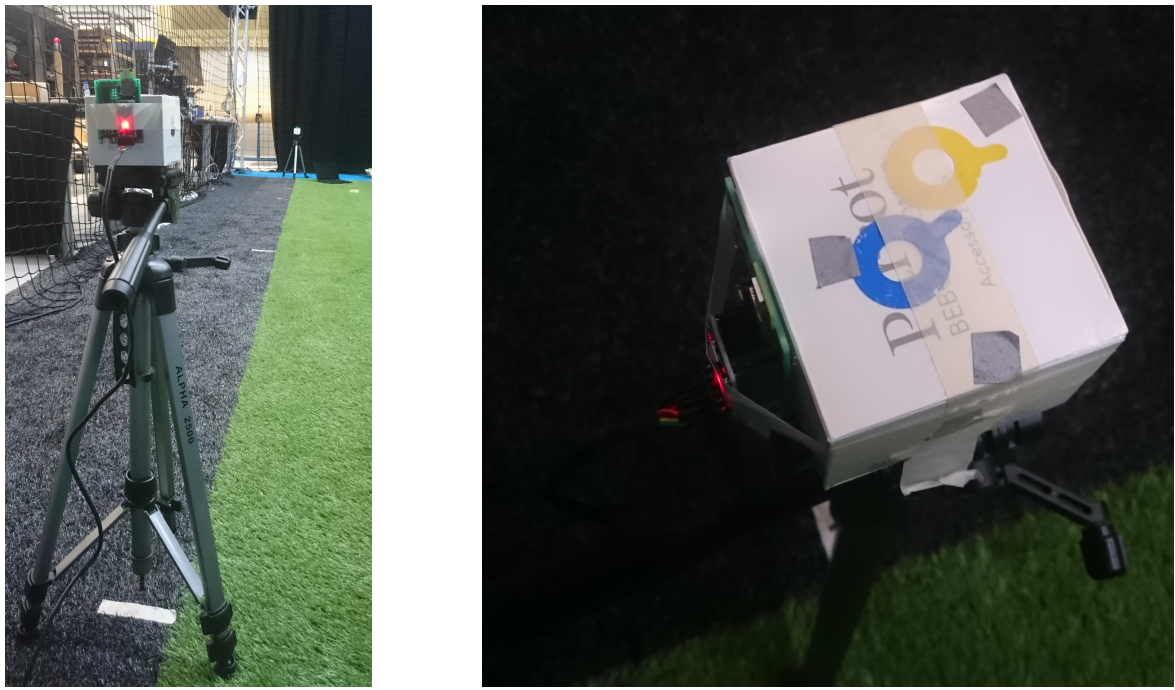


Figure 7-2: Tripod setup used in the experiment

to aid in the initial positioning of the tripods. The actual distances that the tripods are apart will however be read using the MCS with accuracy less than a centimeter. The experiment was repeated with two different pairs of DWM1000 modules to also test differences between modules. Both pairs were calibrated at a 1 meter distance according to the method described in section 7-2.

Finally, in order to capture the effects of antenna orientation, for one of the DWM1000 pairs, the experiment was conducted at 0, 45, and 90 degree antenna orientations (where one of the antennas was rotated about the yawing axis by that amount). This will give insight into the ranging performance when the two antennas are not perfectly facing one another.

7-4 Ranging Experiment Results

With the ranging set-up complete, the results of the experiment were collected. The results have been processed and will be presented in this section.

7-4-1 Raw ranging data

As mentioned, the experiment consisted of collecting range measurements over a time frame of 30 seconds. To give an idea of how the raw range measurements look, a plot of all the collected range samples in one of the experimental conditions is presented in figure 7-3.

It is quite clear just by looking at figure 7-3 by eye that the mean value of the data is above the true value. It is however also true that the range measurements lie within a relatively small interval, which is favorable. The minimum and maximum measured ranges over the

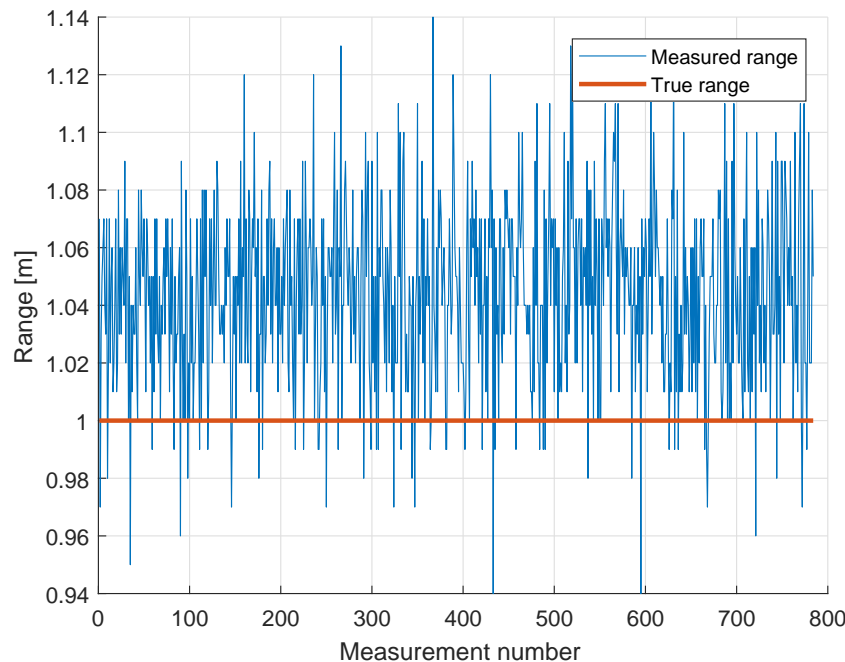


Figure 7-3: Raw range measurement data for measurement distance of 1 meters

whole thirty second interval are 0.94 and 1.14 meters respectively, a difference of only 20 cm.

7-4-2 Processed Range Error Results and Discussion

Raw range measurement data is available for all these experimental conditions similar to that presented in figure 7-3. For all these conditions the raw range measurements are processed and presented in a more suitable format. First the range measurements for two different DWM1000 modules will be compared, and afterwards the range measurements for varying antenna orientations will be compared.

An interesting parameter to first of all look at is the mean range that the UWB modules measure over the 30 second time window, and comparing that to the ground truth value of the range. Ideally the mean measured range and the ground truth should correspond exactly, but in reality there will be a difference between the two. In order to compare these values for all the experimental conditions, a bar chart of the error between the mean measured range and ground truth range for the two different DWM1000's is given in figure 7-4.

Figure 7-4 shows that the mean errors between different pairs of modules have low correlation with each other. The overall performance of the two is however quite similar. The maximum absolute mean error for the first module pair is 10.1 cm, the maximum absolute mean error for the second module is 8.1 cm. The minimum absolute mean error for the first module pair is 0.4 cm, and for the second pair it is 0.6 cm. On average the first module pair has a mean absolute error of 4.3 cm, and the second module pair has a mean absolute error of 4.4 cm over the six measured ranges. The overall performance of the two module pairs is therefore very comparable.

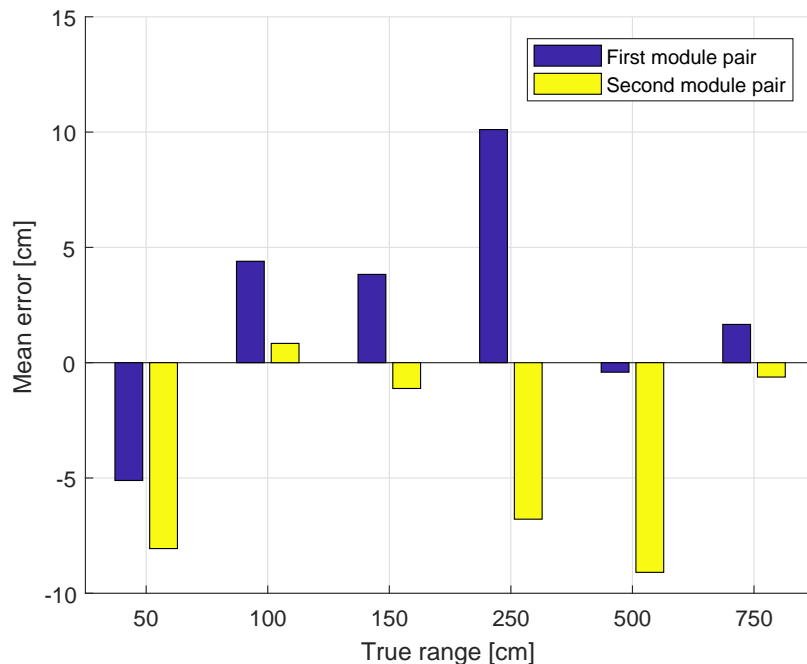


Figure 7-4: Bar chart comparing mean measured ranges to ground truth ranges

Another important parameter to look at is the standard deviation of the collected range data. A similar bar chart, but this time of the standard deviation is given in figure 7-5.

The standard deviations between the two pairs of modules are much more similar than the mean errors presented earlier. The clear exception is the standard deviation of the second module pair measured at 750 cm range. For this particular measurement the standard deviation is much greater than the standard deviations in any of the other conditions. This is quite an unexpected result, especially because the standard deviations in all the other conditions are all very similar (ranging from about 1.5-3 cm).

One possible explanation is that for that particular experimental condition there was a specific multipath profile that was difficult for the algorithm within the DWM1000 modules to identify. This could consequently result in the DWM1000 incorrectly identifying the first arriving path of the received signal, which is necessary to perform Time of Flight (TOF) measurements. Instead it might have identified one of the multipath reflections as the first arriving path, which would cause the determined range to increase (since multipaths take longer to arrive than the direct paths). This is supported by inspecting the raw data of that specific experimental condition, which shows that there are a large number of spikes in the data going towards higher determined ranges.

Other variables that could have influenced the result is the fact that it was the last experiment, and that the tripod had been moved about several times before. Some of the equipment may have come loose, resulting in less stable ranging performance. Furthermore, the experiment was conducted in an area with lots of electromechanical equipment. Other equipment may have radiated EM energy in the UWB frequency range during the final test, which could have resulted in poorer performance.

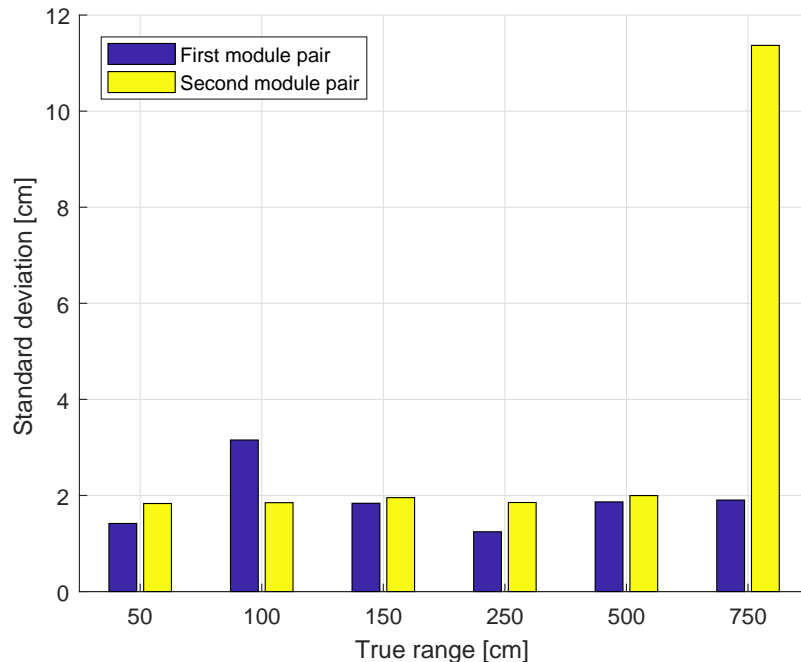


Figure 7-5: Bar chart comparing standard deviations of two DWM1000 pairs

Apart from this one experimental condition the standard deviations of the range measurements are mostly around 2 cm. This is a good result, especially considering that the standard deviation does not necessarily increase as measurement distance increases. The same can be said for the mean errors in figure 7-4, which also do not necessarily increase with increasing range. This means that the modules can provide good performance at lower and higher ranges, making it a versatile piece of hardware.

Now that the ranging data of the two DWM1000 module pairs has been presented, the effect of changing antenna orientation (about the yaw axis) will be analyzed. Just like before, the mean ranging error and its standard deviation are presented in figures 7-6 and 7-7.

It can clearly be seen that the antenna orientation has an effect on the ranging performance at different individual measurement distances, but overall the performance between the different orientations is very similar. All orientations have maximum absolute errors of around 10 cm, and minimum absolute errors of less than 3 cm. On average, the 0, 45, and 90 degree orientations have absolute errors of 4.3, 5.7, and 6.3 cm. The trends in the error appear to be relatively similar between the different antenna orientations as well. The maximum negative error is obtained at a distance of 50 cm, the error then increases as the measurement distance increases to 250 cm, then decreases again for 500 cm, and increases a little bit again towards 750 cm.

The standard deviations across all the different antenna orientations and measurement distances is very similar. All standard deviations lie between 1.2 and 3.7 cm, with average standard deviations around 2 cm. This time there is no observation of a single experimental condition showing much higher standard deviations like the one observed in figure 7-5.

Regardless of the antenna orientation the mean absolute error stays below 12 cm. When

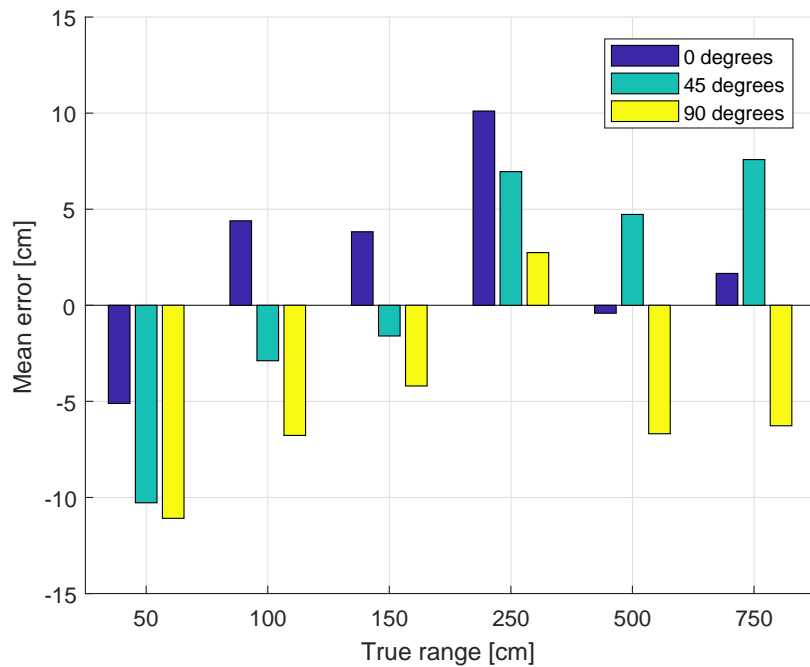


Figure 7-6: Bar chart comparing mean measured ranges to ground truth ranges at different antenna orientations

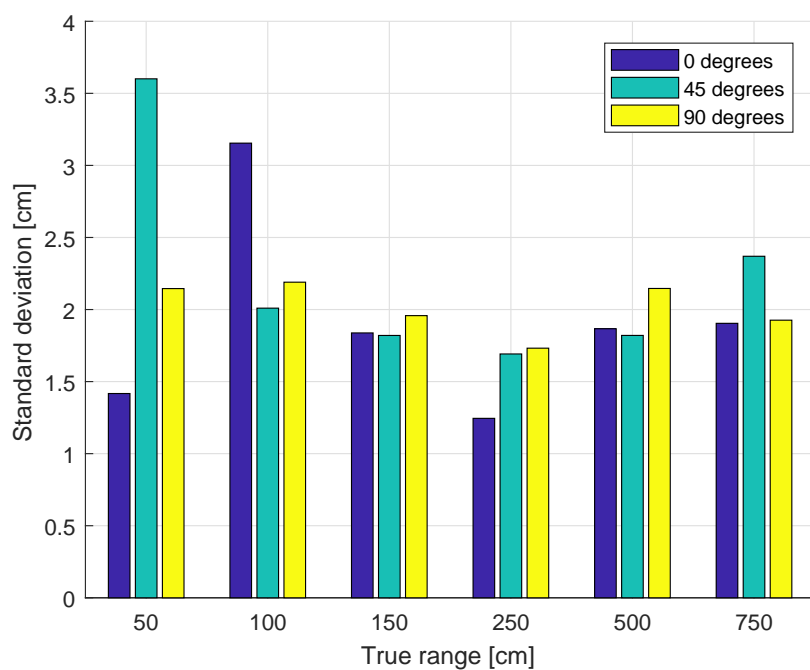


Figure 7-7: Bar chart comparing standard deviations when ranging at different antenna orientations

the modules are equipped to drones, it is important that the errors stay reasonably low even with changing orientations. We do however see that in the leader follower flight experiments presented in part I of the thesis that in this case we do observe larger errors. Of course in the actual leader-follower flight the UWB modules are constantly moving and changing orientation, making the ranging more difficult.

7-4-3 Normality of Ranging Data and Error Bounds

It is ultimately desirable for the errors between measured range and true range to be normally distributed. This can be useful for example when using these measured ranges in filters like the Kalman filter that make use of the assumption of normally distributed errors.

In order to test for normality, two well known tests will be applied to the data, namely the Kolmogorov Smirnov (K-S) test, and the Shapiro Wilk (S-W) test. Both these tests allow the comparison of sample data with the (nul-)hypothesis that the sample is drawn from a normal distribution. Unfortunately both tests show that none of the samples from the different experimental conditions are normally distributed.

Finally, the 95% worst case error is determined for the experimental conditions that compared the two different DWM1000 module pairs. The resulting error bounds are displayed in figure 7-8.

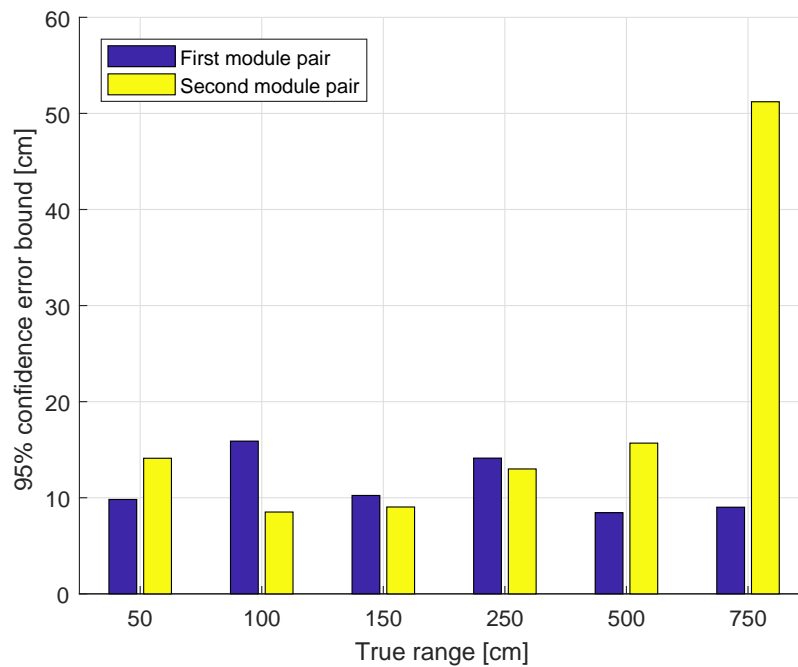


Figure 7-8: 95% confidence worst case error for each measurement distance

It is shown that the 95% confidence worst case error stays below 16 cm for both module pairs except for the second module pair at 750 cm range. Again this is caused by the fact that this particular experimental condition had much higher standard deviation than the other conditions did.

Chapter 8

Parrot Bebop 2 characteristics

In this chapter we briefly look at the characteristics of the Bebop 2 drone by parrot¹, which is the drone used for the experiments presented in the scientific paper in part I of this thesis. First the step response to a velocity command is examined in section 8-1. Afterwards, some data regarding the on-board measurements of height and velocity by the Bebop 2 is given in section 8-2.

8-1 Parrot Bebop 2 step response

In the scientific paper in part I of this thesis, the step response of the Bebop 2 with respect to a velocity input is approximated as a first order delay. In this section a brief analysis is given of the actual step response of the Bebop 2 to a velocity command.

In figure 8-1 we see the step response of a Bebop 2 in forward and backward direction to a velocity command of 0.5 m/s. In the same figure, there are two approximations to the step response of the Bebop 2, one is a first order approximation, whose transfer function is:

$$H_1(s) = \frac{1}{\tau s + 1} \quad (8-1)$$

with s being the Laplace variable and τ the characteristic time delay of the system.

The other approximation is a second order approximation, with transfer function:

$$H_2(s) = \frac{\omega_n^2}{s^2 + 2\zeta\omega_n + \omega_n^2} \quad (8-2)$$

where ζ is the damping of the system, and ω_n the natural frequency.

To generate the approximations in figure 8-1, the value chosen for τ is 1. The value chosen for ζ is 0.32 and the value for ω_n is 0.95. These values were tuned by hand to match the data of the Bebop 2 as well as possible.

It is very obvious from figure 8-1 that the step response of the Bebop 2 to a velocity command is much better approximated by a second order system than by a first order system. In the scientific paper in part I, however, the control method still assumes the Bebop 2 step response to a velocity command to be approximated as a first order delay.

¹<https://www.parrot.com/us/drones/parrot-bebop-2>

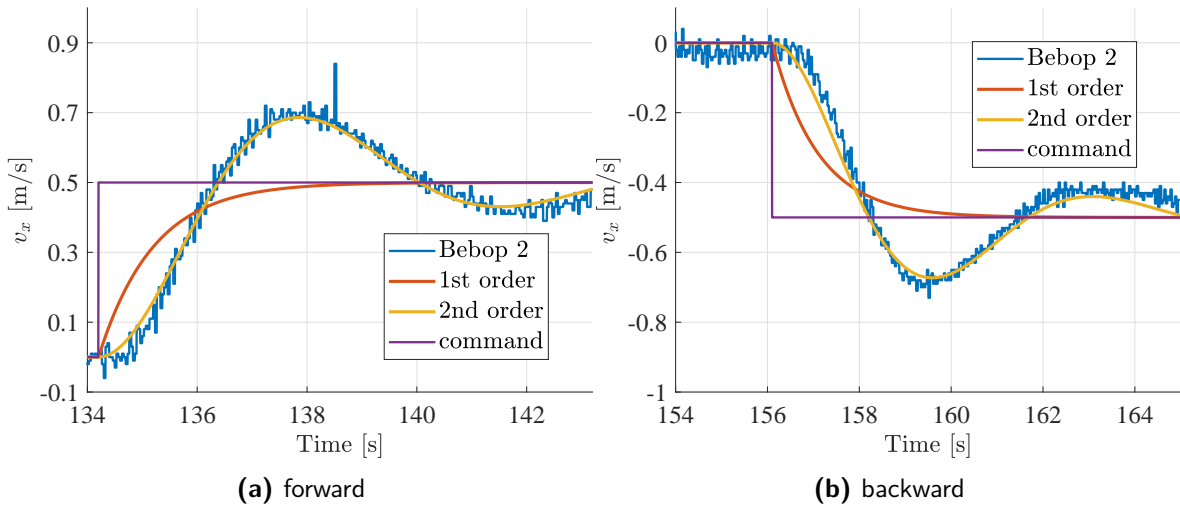


Figure 8-1: Step response of Bebop 2 to a velocity command of 0.5 m/s, along with first and second order approximations.

Despite the discrepancy in the assumed model, and the real step response of the Bebop 2, the derived control law still accomplishes the desired leader-follower behavior. This is primarily the result of the fact that the control law simply responds to the mismatch in models by issuing more aggressive commands as soon as the Bebop 2 does not respond as expected according to a first order delay.

It can further be shown that deriving a control law with a second order approximation for the step response results in a very similar control law. The control law with a second order approximation was also implemented on a Bebop 2, but was not seen to make the follower behave any better than the control law with a first order approximation did. This might change if the command saturation is increased to higher values, but this would have to be investigated in future research. Due to the sufficiency of the results obtained with just a first order delay, the control law with a second order approximation was not further investigated.

8-2 Parrot Bebop 2 on-board measurements

In the scientific paper in part I, the leader-follower flight is first performed with height and velocity data provided by an overhead Motion Capture System (MCS). Afterwards, in a second iteration, the height and velocity data is obtained from on-board sensor information. The height is obtained from an on-board ultrasonic sensor, and the velocity is obtained using Lucas-Kanade based optical flow measurements from the drone's bottom-facing camera.

Despite the switch to on-board sensory information, the followers were still able to successfully follow the leader. This can largely be attributed to the fact that the on-board sensors are actually quite accurate. To demonstrate this, the on-board sensory information will be compared to that provided by the MCS.

Consider first of all the height information provided by the on-board ultrasonic sensor in figure 8-2. Whilst the noise is slightly increased compared to MCS height information, the mean is actually very close to the MCS data. This is especially important when using it in the Extended Kalman Filter (EKF), since the noise can easily be filtered out. The main

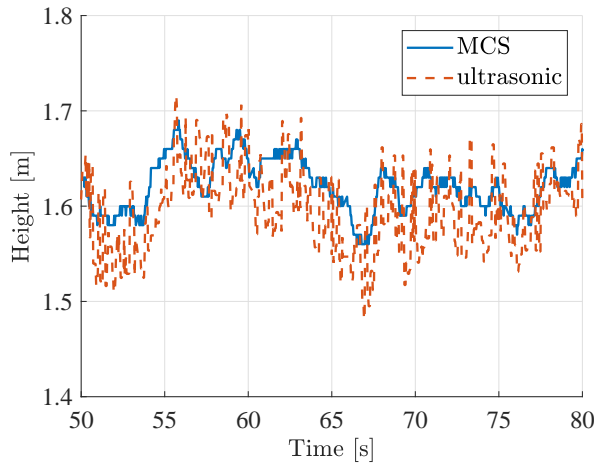


Figure 8-2: Height of Bebop 2 as measured by a MCS and through on-board ultrasonic sensor measurements

difference, as also discussed in the paper, is that the update rate is quite a lot lower for the ultrasonic sensor than for MCS measurements. This does not affect the performance of the relative localization filter so much, since that filter also does not run at a very high frequency, but it does affect the drone's flight performance when using only on-board sensing. It was seen that the drone struggled to maintain altitude, which was likely caused by the lower update rate of the ultrasonic height measurements. In turn, this affected the ability of the drone to move also in the horizontal plane, since it sometimes had to use a lot of thrust to compensate its height.

The second measurement that is replaced with on-board information in the paper is the velocity measurement of the drone. This is replaced by optical flow measurements from the drone's bottom-facing camera. Consider in figure 8-3 a comparison between MCS velocity data, and velocity data from optical flow measurements.

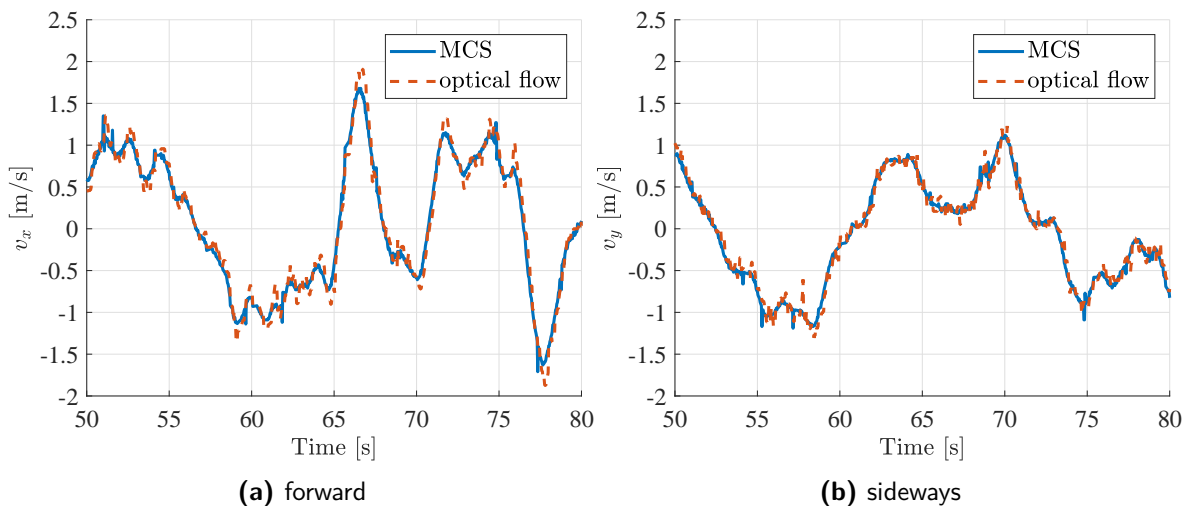


Figure 8-3: Velocity of Bebop 2 as measured by a MCS and through on-board optical flow measurements

Again it is clear that the difference between on-board measurements and MCS measurements is not that high. A slight increase in noise is observed, but nothing that an EKF cannot easily filter out. Much like for the ultrasonic sensor, the update rate of the optical flow measurements will also be lower than the update rate for the MCS measurements, however.

The main issue with optical flow measurement data is that occasionally it does produce much larger errors than visible in figure 8-3. Optical flow measurements rely on the ability of the algorithm to identify features in the camera image from the bottom-facing camera. Occasionally it fails to identify any such features, during which the optical flow measurements will estimate a much lower velocity than the drone is really flying at. This is however not observed very frequently. Most of the time the velocity data from optical flow measurements is very reliable.

Bibliography

- [1] M. Achtelik, Y. Brunet, M. Chli, S. Chatzichristofis, J. D. Decotignie, K. M. Doth, F. Fraundorfer, L. Kneip, D. Gurdan, L. Heng, E. Kosmatopoulos, L. Doitsidis, G. H. Lee, S. Lynen, A. Martinelli, L. Meier, M. Pollefeys, D. Piguet, A. Renzaglia, D. Scaramuzza, R. Siegwart, J. Stumpf, P. Tanskanen, C. Troiani, and S. Weiss. Sfly: Swarm of micro flying robots. In *2012 IEEE/RSJ International Conference on Intelligent Robots and Systems*, pages 2649–2650, Oct 2012.
- [2] Muhammad Haris Afzal, Valérie Renaudin, and Gérard Lachapelle. Assessment of Indoor Magnetic Field Anomalies using Multiple Magnetometers. *23rd International Technical Meeting of the Satellite Division of the Institute of Navigation*, pages 525–533, 2010.
- [3] G. R. Aiello and G. D. Rogerson. Ultra-wideband wireless systems. *IEEE Microwave Magazine*, 4(2):36–47, June 2003.
- [4] Saleh O Al-jazzar, Artem Muchkaev, Ahmad Al-Nimrat, and Mahmoud Smadi. Low complexity and high accuracy angle of arrival estimation using eigenvalue decomposition with extension to 2D AOA and power estimation. *EURASIP Journal on Wireless Communications and Networking*, 2011:123, 2011.
- [5] Abdulrahman Alarifi, AbdulMalik S. Al-Salman, Mansour Alsaleh, Ahmad Alnafessah, Suheer Al-Hadhrami, Mai A. Al-Ammar, and Hend S. Al-Khalifa. Ultra Wideband Indoor Positioning Technologies: Analysis and Recent Advances. *Sensors*, 16(5):707, 2016.
- [6] Sjriek Alers, Daniel Claes, Karl Tuyls, and Gerhard Weiss. Biologically Inspired Multi-Robot Foraging (Demonstration). In *Proceedings of the 13th International Conference on Autonomous Agents and Multiagent Systems (AAMAS 2014)*, pages 1683–1684, May 2014.
- [7] A. I. Baba and M. M. Atia. Burst mode symmetric double sided two way ranging. In *2011 IFIP Wireless Days (WD)*, pages 1–3, Oct 2011.

- [8] Terence Barrett. History of UltraWideBand (UWB) Radar & Communications: Pioneers and Innovators. In *Progress In Electromagnetics Symposium 2000 (PIERS2000)*, 2000.
- [9] M. Basiri, F. Schill, D. Floreano, and P. U. Lima. Audio-based localization for swarms of micro air vehicles. In *2014 IEEE International Conference on Robotics and Automation (ICRA)*, pages 4729–4734, May 2014.
- [10] M. Basiri, F. Schill, P. Lima, and D. Floreano. On-board relative bearing estimation for teams of drones using sound. *IEEE Robotics and Automation Letters*, 1(2):820–827, July 2016.
- [11] Anuj Batra et al. Multi-band OFDM Physical Layer Proposal for IEEE 802.15 Task Group 3a. Technical report document IEEE P802.15-03/268r2, 2003.
- [12] R. W. Beard and T. W. McLain. Multiple uav cooperative search under collision avoidance and limited range communication constraints. In *42nd IEEE International Conference on Decision and Control*, volume 1, pages 25–30, Dec 2003.
- [13] Maria-Gabriella Di Benedetto, Thomas Kaiser, Andreas F. Molisch, Ian Oppermann, Christian Politano, and Domenico Porcino. *UWB communication systems: a comprehensive guide*. Hindawi Publishing Corporation, 2006.
- [14] Alessandro Benini, Adriano Mancini, and Sauro Longhi. An IMU/UWB/vision-based extended kalman filter for mini-UAV localization in indoor environment using 802.15.4a wireless sensor network. *Journal of Intelligent and Robotic Systems*, 70:461–476, 2013.
- [15] M. Brambilla, E. Ferrante, M. Birattari, and Marco. Dorigo. Swarm robotics: a review from the swarm engineering perspective. *Swarm Intelligence*, 7(1):1–41, 2013.
- [16] Alexandre Campo, Shervin Nouyan, Mauro Birattari, Roderich Groß, and Marco Dorigo. Negotiation of goal direction for cooperative transport. In Marco Dorigo, Luca Maria Gambardella, Mauro Birattari, Alcherio Martinoli, Riccardo Poli, and Thomas Stützle, editors, *Ant Colony Optimization and Swarm Intelligence. Ants 2006*, volume 4150, pages 191–202, Berlin, Heidelberg, 2006. Springer Berlin Heidelberg.
- [17] P. A. Catherwood and W. G. Scanlon. Ultrawideband communications - an idea whose time has still yet to come? [wireless corner]. *IEEE Antennas and Propagation Magazine*, 57(2):38–43, April 2015.
- [18] Hande Çelikkanat and Erol Şahin. Steering self-organized robot flocks through externally guided individuals. *Neural Computing and Applications*, 19(6):849–865, 2010.
- [19] Xiaomin Chen and Sayfe Kiaei. Monocycle Pulse Shapes for Ultra Wideband System. In *2002 IEEE International Symposium on Circuits and Systems*, 2002.
- [20] Soon Hooi Chiew, Weihua Zhao, and Tiauw Hieng Go. Swarming Coordination with Robust Control Lyapunov Function Approach. *Journal of Intelligent and Robotic Systems*, 78(3):499–515, 2015.

- [21] M. Coppola, K. McGuire, K. Y. W. Scheper, and G. C. H. E. de Croon. *On-board Communication-based Relative Localization for Collision Avoidance in Micro Air Vehicle teams.* arxiv:1609.08811, submitted on 28 sep 2016.
- [22] Neiyer S Correal, Spyros Kyperountas, Qicai Shi, and Matt Welborn. An UWB Relative Location System. In *2003 IEEE Conference on Ultra Wideband Systems and Technologies*, pages 394–397, 2003.
- [23] Nikolaus Correll, Samuel Rutishauser, and Alcherio Martinoli. Comparing coordination schemes for miniature robotic swarms: A case study in boundary coverage of regular structures. *Springer Tracts in Advanced Robotics*, 39:471–480, 2008.
- [24] A. K. Das, R. Fierro, V. Kumar, J. P. Ostrowski, J. Spletzer, and C. J. Taylor. A vision-based formation control framework. *IEEE Transactions on Robotics and Automation*, 18(5):813–825, Oct 2002.
- [25] DecaWave. ScenSor DWM1000 Module. <https://www.decawave.com/products/dwm1000-module>. [Online] Accessed: 12 February 2018.
- [26] European Commission (EC). Commission Decision of 21 February 2007 on allowing the use of the radio spectrum for equipment using ultra-wideband technology in a harmonised manner in the Community. *Official Journal of the European Union*, L55:33–36, 2007. Decision 2007/131/EC Accessed: 20 April 2017.
- [27] European Commission (EC). Commission Implementing Decision of 7 October 2014 amending Decision 2007/131/EC on allowing the use of the radio spectrum for equipment using ultra-wideband technology in a harmonised manner in the Community. *Official Journal of the European Union*, L293:48–56, 2014. Decision 2014/702/EU Accessed: 20 April 2017.
- [28] European Telecommunications Standards Institute (ETSI). Short Range Devices (SRD) using Ultra Wide Band (UWB); Measurement Techniques. 2016. Draft ETSI EN 303 883 v1.1.0 Accessed: 20 April 2017.
- [29] European Telecommunications Standards Institute (ETSI). The European regulatory environment for radio equipment and spectrum: an introduction. 2016. Version 2.1, July 2016, Accessed: 20 April 2017.
- [30] Federal Communications Commission (FCC). Revision of Part 15 of the Commission’s Rules Regarding Ultra-Wideband Transmission Systems. *First Report and Order*. ET Docket 98-153, FCC 02-48, Released: April 22, 2002.
- [31] Xavier N. Fernando, Srithar Krishnan, Hongbo Sun, and Kamyar Kazemi-Moud. Adaptive denoising at infrared wireless receivers. *Infrared Technology and Applications XXIX*, 5074, 2003.
- [32] Jeff Foerster. Channel Modeling Sub-committee Report Final. Technical report document IEEE P802.15-02/490r1-SG3a, IEEE 802.15 Working Group for Wireless Personal Area Networks, 2003.

- [33] Jeff Foerster, Evan Green, Srinivasa Somayazulu, and David Leeper. Ultra-Wideband Technology for Short- or Medium-Range Wireless Communications. *Intel Technology Journal*, 2, 2001.
- [34] R. J. Fontana, E. A. Richley, A. J. Marzullo, L. C. Beard, R. W. T. Mulloy, and E. J. Knight. An ultra wideband radar for micro air vehicle applications. *IEEE Conference on Ultra Wideband Systems and Technologies*, pages 187–191, 2002.
- [35] Robert J. Fontana. Recent system applications of short-pulse ultra-wideband (UWB) technology. *IEEE Transactions on Microwave Theory and Techniques*, 52(9):2087–2104, 2004.
- [36] Ranjit Gharpurey and Peter Kinget, editors. *Ultra Wideband Circuits, Transceivers and Systems*. Springer US, 1 edition, 2008.
- [37] Y. Gu, B. Seanor, G. Campa, M. R. Napolitano, L. Rowe, S. Gururajan, and S. Wan. Design and Flight Testing Evaluation of Formation Control Laws. *IEEE Transactions on Control Systems Technology*, 14(6):1105–1112, 2006.
- [38] Yanying Gu, Anthony Lo, and Ignas Niemegeers. A survey of indoor positioning systems for wireless personal networks. *IEEE Communications Surveys and Tutorials*, 11(1):13–32, 2009.
- [39] Kexin Guo, Zhirong Qiu, Wei Meng, Lihua Xie, and Rodney Teo. Ultra-wideband based cooperative relative localization algorithm and experiments for multiple unmanned aerial vehicles in GPS denied environments. *International Journal of Micro Air Vehicles*, 9(3):169–186, 2017.
- [40] Rainer Hach. Symmetric Double Sided Two-Way ranging. In *Contribution 802.15-05-0334-00-004a to the IEEE 802.15.4a Ranging Subcommittee*, 2005.
- [41] Ahmad Hatami and Kaveh Pahlavan. Performance comparison of RSS and TOA indoor geolocation based on UWB measurement of channel characteristics. In *IEEE 17th International Symposium on Personal, Indoor and Mobile Radio Communications*, 2006.
- [42] S. Hauert, S. Leven, M. Varga, F. Ruini, A. Cangelosi, J. C. Zufferey, and D. Floreano. Reynolds flocking in reality with fixed-wing robots: Communication range vs. maximum turning rate. In *2011 IEEE/RSJ International Conference on Intelligent Robots and Systems*, pages 5015–5020, Sept 2011.
- [43] A. T. Hayes and P. Dormiani-Tabatabaei. Self-organized flocking with agent failure: Off-line optimization and demonstration with real robots. In *2002 IEEE International Conference on Robotics and Automation*, pages 3900–3905, 2002.
- [44] Adam T. Hayes, Alcherio Martinoli, and Rodney M. Goodman. Swarm robotic odor localization: Off-line optimization and validation with real robots. *Robotica*, 21(4):427–441, 2003.
- [45] Malek G. M. Hussain. Ultra-wideband impulse radar - An overview of the principles. *IEEE Aerospace and Electronic Systems Magazine*, 13(9):9–14, 1998.

- [46] I. I. Immoreev and P. G. S. D. V. Fedotov. Detection of UWB signals reflected from complex targets. *IEEE Conference on Ultra Wideband Systems and Technologies*, pages 193–196, 2002.
- [47] S. J. Ingram, D. Harmer, and M. Quinlan. Ultrawideband indoor positioning systems and their use in emergencies. In *PLANS 2004. Position Location and Navigation Symposium*, pages 706–715, April 2004.
- [48] Arjun Iyer, Luis Rayas, and Andrew Bennett. Formation Control for Cooperative Localization of MAV Swarms (Demonstration). In *Proceedings of the 2013 International Conference on Autonomous Agents and Multi-agent Systems*, pages 1371–1372, 2013.
- [49] Matarić M. J. Reinforcement Learning in the Multi-Robot Domain. *Autonomous Robots*, 4(1):73–83, 1997.
- [50] Damien B. Jourdan, Davide Dardari, and Moe Z. Win. Position error bound for UWB localization in dense cluttered environments. In *2006 IEEE International Conference on Communications*, 2006.
- [51] Kamol Kaemarungsi and Prashant Krishnamurthy. Modeling of Indoor Positioning Systems Based on Location Fingerprinting. *INFOCOM 2004. Twenty-third Annual Joint Conference of the IEEE Computer and Communications Societies*, 2:1012 – 1022, 2004.
- [52] I. D. Kelly and D. A. Keating. Flocking by the fusion of sonar and active infrared sensors on physical autonomous mobile robots. In *Third International Conference on Mechatronics and Machine Vision in Practice*, volume 1, pages 1–4, 1996.
- [53] Serge Kernbach and Olga Kernbach. Collective energy homeostasis in a large-scale microrobotic swarm. *Robotics and Autonomous Systems*, 59(12):1090–1101, 2011.
- [54] T. Kikkawa, P. K. Saha, N. Sasaki, and K. Kimoto. Gaussian monocycle pulse transmitter using 0.18 *mu*hbox{m} cmos technology with on-chip integrated antennas for inter-chip uwb communication. *IEEE Journal of Solid-State Circuits*, 43(5):1303–1312, May 2008.
- [55] Hakyong Kim. Double-sided two-way ranging algorithm to reduce ranging time. *IEEE Communications Letters*, 13(7):486–488, 2009.
- [56] M. Klemm, I. Craddock, J. Leendertz, A. Preece, and R. Benjamin. Experimental and clinical results of breast cancer detection using UWB microwave radar. *2008 IEEE Antennas and Propagation Society International Symposium*, 2008.
- [57] M. Klemm, I. J. Craddock, J. A. Leendertz, A. Preece, and R. Benjamin. Radar-based breast cancer detection using a hemispherical antenna array—experimental results. *IEEE Transactions on Antennas and Propagation*, 57(6):1692–1704, 2009.
- [58] Dušan Kocur, Mária Svecová, and Jana Rovnáková. Through-the-wall localization of a moving target by two independent ultra wideband (UWB) radar systems. *Sensors*, 13(9):11969–11997, 2013.

- [59] M. Kriegleder, S. T. Digumarti, R. Oung, and R. D’Andrea. Rendezvous with bearing-only information and limited sensing range. In *2015 IEEE International Conference on Robotics and Automation*, pages 5941–5947, 2015.
- [60] Sivanand Krishnan, Pankaj Sharma, Zhang Guoping, and Ong Hwee Woon. A UWB based localization system for indoor robot navigation. In *2007 IEEE International Conference on Ultra-Wideband*, pages 77–82, 2007.
- [61] Alex Kushleyev, Daniel Mellinger, Caitlin Powers, and Vijay Kumar. Towards a swarm of agile micro quadrotors. *Autonomous Robots*, 35(4):287–300, 2013.
- [62] Myungkyun Kwak and Jongwha Chong. A new double two-way ranging algorithm for ranging system. In *Proceedings - 2010 2nd IEEE International Conference on Network Infrastructure and Digital Content*, pages 470–473, 2010.
- [63] J. X. Lee, Z. Lin, and C. P. S. Francois. Symmetric double side two way ranging with unequal reply time. In *2007 IEEE 66th Vehicular Technology Conference*, pages 1980–1983, 2007.
- [64] Jin Shyan Lee, Yu Wei Su, and Chung Chou Shen. A comparative study of wireless protocols: Bluetooth, UWB, ZigBee, and Wi-Fi. In *IECON 2007 - 33rd Annual Conference of the IEEE Industrial Electronics Society*, pages 46–51, 2007.
- [65] Joon-Yong Lee and Robert A. Scholtz. Ranging in a dense multipath environment using an UWB radio link. *IEEE Journal on Selected Areas in Communications*, 20(9):1677–1683, 2002.
- [66] Yingsong Li, Wenxing Li, and Qiubo Ye. A reconfigurable wide slot antenna integrated with sirs for UWB/multiband communication applications. *Microwave and Optical Technology Letters*, 55(1):52–55, 2013.
- [67] H. Liu, H. Darabi, P. Banerjee, and J. Liu. Survey of Wireless Indoor Positioning Techniques and Systems. *IEEE Transactions on Systems, Man, and Cybernetics, Part C (Applications and Reviews)*, 37(6):1067–1080, 2007.
- [68] H. Lv, G. H. Lu, X. J. Jing, and J. Q. Wang. A new ultra-wideband radar for detecting survivors buried under earthquake rubbles. *Microwave and Optical Technology Letters*, 52(11):2621–2624, 2010.
- [69] Mohamed R. Mahfouz, Cemin Zhang, Brandon C. Merkl, Michael J. Kuhn, and Aly E. Fathy. Investigation of high-accuracy indoor 3-D positioning using UWB technology. *IEEE Transactions on Microwave Theory and Techniques*, 56(6):1316–1330, 2008.
- [70] A. Martinelli and R. Siegwart. Observability analysis for mobile robot localization. In *2005 IEEE/RSJ International Conference on Intelligent Robots and Systems*, pages 1471–1476, Aug 2005.
- [71] J. McLurkin and Jennifer Smith. Distributed algorithms for dispersion in indoor environments using a swarm of autonomous mobile robots. In R. Alami, R. Chatila, and H. Asama, editors, *Distributed Autonomous Robotic Systems 6*, pages 399–408. Springer, Tokyo, 2007.

- [72] Chris Melhuish and Jason Welsby. Gradient ascent with a group of minimalist real robots: implementing secondary swarming. In *2002 IEEE International Conference on Systems, Man and Cybernetics*, pages 509–514, 2002.
- [73] L. Merino, F. Caballero, J. R. Martinez-de Dios, J. Ferruz, and A. Ollero. A cooperative perception system for multiple UAVs: Application to automatic detection of forest fires. *Journal of Field Robotics*, 23(3-4):165–184, 2006.
- [74] N. Michael, D. Mellinger, Q. Lindsey, and V. Kumar. The GRASP Multiple Micro-UAV Test Bed: Experimental evaluation of multirobot aerial control algorithms. *IEEE Robotics & Automation Magazine*, 17(3):56–65, 2010.
- [75] Andreas F. Molisch, Kannan Balakrishnan, Dajana Cassioli, Chia-chin Chong, Shahriar Emami, Andrew Fort, Johan Karedal, Juergen Kunisch, Hans Schantz, Ulrich Schuster, and Kai Siwiak. IEEE 802.15.4a channel model - final report. Technical report document IEEE 802.15-04-0662-02-004a, 2005.
- [76] Andreas F. Molisch, Dajana Cassioli, Chia-Chin Chong, Shahriar Emami, Andrew Fort, Balakrishnan Kannan, Johan Karedal, Juergen Kunisch, Hans Gregory Schantz, Kazimierz Siwiak, and Moe Z. Win. A comprehensive standardized model for ultrawideband propagation channels. *IEEE Transactions on Antennas and Propagation*, 54(11):3151–3166, 2006.
- [77] M. W. Mueller, M. Hamer, and R. D’Andrea. Fusing ultra-wideband range measurements with accelerometers and rate gyroscopes for quadrocopter state estimation. In *2015 IEEE International Conference on Robotics and Automation (ICRA)*, pages 1730–1736, 2015.
- [78] Yash Mulgaonkar, Gareth Cross, and Vijay Kumar. Design of small, safe and robust quadrotor swarms. In *2015 IEEE International Conference on Robotics and Automation (ICRA)*, pages 2208–2215, 2015.
- [79] S. Nag, H. Fluhler, and M. Barnes. Preliminary Interferometric Images of Moving Targets obtained using a Time- Modulated Ultra-Wide Band Through-Wall Penetration Radar. In *Proceedings of the 2001 IEEE Radar Conference*, pages 64–69, 2001.
- [80] Tobias Nägeli, Christian Conte, Alexander Domahidi, Manfred Morari, and Otmar Hilliges. Environment-independent Formation Flight for Micro Aerial Vehicles. In *2014 IEEE/RSJ International Conference on Intelligent Robots and Systems*, pages 1141–1146, 2014.
- [81] Dries Neirynck, Eric Luk, and Michael McLaughlin. An alternative double-sided two-way ranging method. In *13th Workshop on Positioning, Navigation and Communications (WPNC)*, 2016.
- [82] T. M. Nguyen, A. H. Zaini, K. Guo, and L. Xie. An Ultra-Wideband-based Multi-UAV Localization System in GPS-denied environments. In *International micro air vehicle competition and conference 2016*, pages 56–61, 2016.
- [83] Homayoun Nikookar and Ramjee Prasad. *Introduction to Ultra Wideband for Wireless Communications*. Springer Netherlands, 1 edition, 2009.

- [84] Jesús Pestana, Jose Luis Sanchez-Lopez, Paloma de la Puente, Adrian Carrio, and Pascual Campoy. A Vision-based Quadrotor Multi-robot Solution for the Indoor Autonomy Challenge of the 2013 International Micro Air Vehicle Competition. *Journal of Intelligent and Robotic Systems*, 84(1-4):601–620, 2015.
- [85] Sylvain Pittet, Valérie Renaudin, Bertrand Merminod, and Michel Kasser. UWB and MEMS Based Indoor Navigation. *The Journal of Navigation*, 61(3):369–384, 2008.
- [86] Domenico Porcino and Walter Hirt. Ultra-wideband radio technology: Potential and challenges ahead. *IEEE Communications Magazine*, 41(7):66–74, 2003.
- [87] R. C. Qiu, H. Liu, and X. Shen. Ultra-wideband for multiple access communications. *IEEE Communications Magazine*, 43(2):80–87, 2005.
- [88] S. A. P. Quintero, G. E. Collins, and J. P. Hespanha. Flocking with fixed-wing UAVs for distributed sensing: A stochastic optimal control approach. In *Proceedings of the American Control Conference*, pages 2025–2031, 2013.
- [89] M. Radovnikovich, P. Fleck, and K. Hallenbeck. Ultra wide-band trajectory following for an omnidirectional factory automation vehicle. In *2014 IEEE International Conference on Technologies for Practical Robot Applications (TePRA)*, pages 1–6, 2014.
- [90] Y. Rahayu, T. A. Rahman, R. Ngah, and P. S. Hall. Ultra wideband technology and its applications. In *5th IFIP International Conference on Wireless and Optical Communications Networks*, pages 1–5, 2008.
- [91] A. K. Raja and Z. Pang. High accuracy indoor localization for robot-based fine-grain inspection of smart buildings. In *2016 IEEE International Conference on Industrial Technology (ICIT)*, pages 2010–2015, March 2016.
- [92] Fernando Ramírez-Mireles. Signal design for ultra-wide-band communications in dense multipath. *IEEE Transactions on Vehicular Technology*, 51(6):1517–1521, 2002.
- [93] C. H. Nagarjuna Reddy and B. R. Sujatha. TDOA Computation Using Multicarrier Modulation for Sensor Networks. *International Journal of Computer Science & Communication Networks*, 1(1):85–90, 2011.
- [94] James F. Roberts, Timothy Stirling, Jean-Christophe Zufferey, and Dario Floreano. 3-D relative positioning sensor for indoor flying robots. *Autonomous Robots*, 33(1-2):5–20, 2012.
- [95] Steven Roelofsen, Denis Gillet, and Alcherio Martinoli. Reciprocal collision avoidance for quadrotors using on-board visual detection. *2015 IEEE/RSJ International Conference on Intelligent Robots and Systems (IROS)*, pages 4810–4817, 2015.
- [96] J. A. Rothermich, M. Í. Ecemîş, and P. Gaudiano. Distributed Localization and Mapping with a Robotic Swarm. In E. Sahin and W. M. Spears, editors, *Swarm Robotics. SR 2004. Lecture Notes in Computer Science*, pages 58–69. Springer, Berlin, 3342 edition, 2005.

- [97] J. Sachs, M. Aftanas, S. Crabbe, M. Drutarovsky, R. Klukas, D. Kocur, T. T. Nguyen, P. Peyerl, J. Rovnakova, and E. Zaikov. Detection and tracking of moving or trapped people hidden by obstacles using ultra-wideband pseudo-noise radar. In *2008 European Radar Conference*, pages 408–411, 2008.
- [98] Erol Şahin. Swarm Robotics: From Sources of Inspiration to domains of Application. In E. Şahin and W.M. Spears, editors, *Swarm Robotics. SR 2004. Lecture Notes in Computer Science*, volume 3342, pages 10–20. Springer, 2005.
- [99] A. A. M. Saleh and R. A. Valenzuela. A Statistical Model for Indoor Multipath Propagation. *IEEE Journal on Selected Areas in Communications*, 5(2):128–137, 1987.
- [100] Martin Saska, Vojtěch Vonásek, Jan Chudoba, Justin Thomas, Giuseppe Loianno, and Vijay Kumar. Swarm Distribution and Deployment for Cooperative Surveillance by Micro-Aerial Vehicles. *Journal of Intelligent & Robotic Systems*, 84(1–4):469–492, 2016.
- [101] R. Scholtz. Multiple access with time-hopping impulse modulation. In *IEEE Military Communications Conference*, pages 447–450, 1993.
- [102] Mac Schwager, Brian J. Julian, and Daniela Rus. Optimal coverage for multiple hovering robots with downward facing cameras. *2009 IEEE International Conference on Robotics and Automation*, pages 3515–3522, 2009.
- [103] Mac Schwager, James McLurkin, Jean-Jacques E. Slotine, and Daniela Rus. From Theory to Practice: Distributed Coverage Control Experiments with Groups of Robots. In O. Khatib, V. Kumar, and G. J. Pappas, editors, *Springer Tracts in Advanced Robotics*, volume 54, pages 127–136. Springer, Berlin, 2009.
- [104] Timothy Stirling, James Roberts, Jean-Christophe Zufferey, and Dario Floreano. Indoor navigation with a swarm of flying robots. In *2012 IEEE International Conference on Robotics and Automation*, pages 4641–4647, 2012.
- [105] Janis Tiemann, Florian Schweikowski, and Christian Wietfeld. Design of an UWB indoor-positioning system for UAV navigation in GNSS-denied environments. In *2015 International Conference on Indoor Positioning and Indoor Navigation (IPIN)*, 2015.
- [106] T. K. K. Tsang and M. N. El-Gamal. Ultra-wideband (UWB) communications systems: An overview. In *The 3rd International IEEE Northeast Workshop on Circuits and Systems Conference*, pages 381–386, 2005.
- [107] Matthew Turpin, Nathan Michael, and Vijay Kumar. Decentralized formation control with variable shapes for aerial robots. *2012 IEEE International Conference on Robotics and Automation*, pages 23–30, 2012.
- [108] G. Vásárhelyi, Cs. Virág, G. Somorjai, N. Tarcai, T. Szörényi, T. Nepusz, and T. Vicsek. Outdoor flocking and formation flight with autonomous aerial robots. In *2014 IEEE/RSJ International Conference on Intelligent Robots and Systems*, pages 3866–3873, 2014.

- [109] S. Weiss, M. W. Achtelik, S. Lynen, M. Chli, and R. Siegwart. Real-time Onboard Visual-Inertial State Estimation and Self-Calibration of MAVs in Unknown Environments. In *2012 IEEE International Conference on Robotics and Automation (ICRA)*, pages 957–964, 2012.
- [110] M. Z. Win and R. A. Scholtz. Impulse radio: how it works. *IEEE Communications Letters*, 2(2):36–38, 1998.
- [111] Liuqing Yang and G. B. Giannakis. Ultra-Wideband Communications: an idea whose time has come. *IEEE Signal Processing Magazine*, 21(6):26–54, 2004.
- [112] C. Zhang, M. Kuhn, B. Merkl, M. Mahfouz, and A. E. Fathy. Development of an uwb indoor 3d positioning radar with millimeter accuracy. In *2006 IEEE MTT-S International Microwave Symposium Digest*, pages 106–109, 2006.
- [113] Xun S. Zhou and Stergios I. Roumeliotis. Robot-to-robot relative pose estimation from range measurements. *IEEE Transactions on Robotics*, 24(6):1379–1393, 2008.
- [114] Weihua Zhuang, Xuemin Shen, and Qi Bi. Ultra-wideband wireless communications. *Wireless Communications and Mobile Computing*, 3(6):663–685, 2003.